UNIVERSITÀ DEGLI STUDI DI CATANIA

Ph.D. in Materials Science XXVI Cycle

Ph.D. Thesis

Metal organic chemical vapor deposition of multifuctionalperovskitic oxides: from giant K to colossal magnetoresistance materials, from ionic conductors to multiferroics.

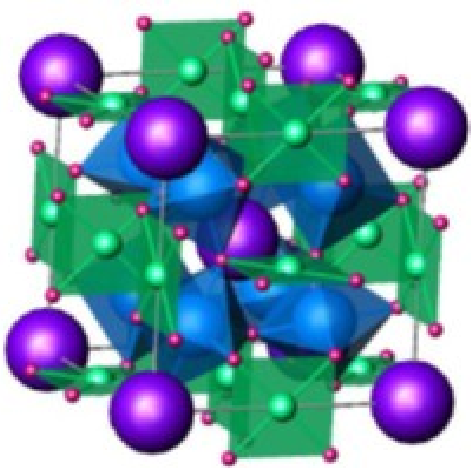

Ph.D. Student: ***MARIA RITA CATALANO***

Advisor:
Prof. Graziella Malandrino

Coordinator:
Prof. Maria Grazia Grimaldi

2011-2013

Contents

Chapter 5: Multiferroic perovskite $BiFeO_3$ film *60*

Introduction

Oxide materials have several applicative properties such as ionic and electronic conductors for solid oxide fuel cells, high temperature superconductivity, giant dielectric constant, colossal magneto-resistance, ferroelectricity, multiferroicity, and so on.

Among the oxide material, the perovskite structure class is one of the most commonly occurring and important in all fields of materials science. The interest in these compounds is due to its structure that offers an high degree of chemical flexibility which determines its electronic and magnetic properties. In fact, perovskite compounds exhibit a large and surprising variety of properties, including superconductivity, colossal magnetoresistance, ionic conductivity, piezoelectricity and ferroelectricity, and find several applications for electronic and photonic devices. The ideal perovskite ABX_3have a cubic crystal structure which consists of corner sharing $[BX_6]$ octahedral with the A cation occupying the 12-fold coordination site formed in the middle of the cube formed by the eight such octahedra. The ideal cubic perovskite structure is not very common but, there are many different types of distortions which can occur from the ideal structure. These include tilting of the octahedra, displacements of the cations out of the centers of their coordination polyhedra, and distortions of the octahedra driven by electronic factors (i.e. Jahn-Teller distortions). Many of the physical properties of perovskites depend crucially on the details of these distortions, particularly the electronic, magnetic and dielectric properties which are so important for many of the applications of perovskite materials.

In this context, the following work discuss about some different perovskite materials such as calcium copper titanate $CaCu_3Ti_4O_{12}$, bismuth ferrite $BiFeO_3$, lanthanum cobaltite ($LaCoO_3$), barium ceriate ($BaCeO_3$) and Ca-doped praseodymium manganites ($Pr_{1-x}Ca_xMnO_3$), which possess interesting physical properties of scientific and technological interest.

$CaCu_3Ti_4O_{12}$ has an impressive dielectric constant value of 10^5working at 1 MHz which remains constant in the 100–600 K temperature range and slightly depends upon work frequency in the 10^2–10^5Hz range. In addition, CCTO does not show ferroelectric transition or relaxor behavior. The giant-k dielectric materials as CCTO can be used in high capacity density planar condensers used in integrated circuits for wireless communication.

The bismuth ferrite ($BiFeO_3$) is a multiferroic material; it is probably the only material that is both magnetic and ferroelectric at room temperature. It has many application from sensor electronics, spintronics, next-generation non-volatile memories and photovoltaic.

Lanthanum cobaltites ($LaCoO_3$) have a large variety of magnetic, ferroelastic and electrical properties, and are promising candidates as ionic conductors and surface catalysts.

Barium cerate $BaCeO_3$ exhibits high proton conductivities and are attractive candidates for application in electro catalysis and fuel cells. Nevertheless, $BaCeO_3$ shows poor chemical stability and tends to react with water vapor or CO_2, generating insulating $BaCO_3$ and hence inducing breakage of devices and performance degradation. Chemical stability of $BaCeO_3$ can be improved by partial substitution of Ce with Yttrium, Samarium, Niobium and so on .

Calcium-doped praseodymium manganites ($Pr_{1-x}Ca_xMnO_3$)have attracted great attention due to their technologically important electrical, magnetic, and magnetoresistance properties. In particular, very attractive for future developments are the colossal magnetoresistance phenomenon around the ferromagnetic transition temperature (Tc), and the electric pulsed induced resistance (EPIR) effect. For this reason the manganite films have been proposed as active components in non-volatile magnetic random access memory, magnetoresistive read-head, semiconductor field effect transistors.

It is well known, that for many application, it is desirable to synthesize the above mentioned functional materials in the form of nanostructure thick and thin film. Furthermore, the magnetic and electronic properties of perovskite thin films closely depend upon the fabrication method, the growth conditions, and substrate lattice parameters. At the same time developing a “user friendly” and low cost route to this material in form of thin films represents a challenging goal. In fact, perovskite thin films deposited through an industrially transferable and scalable methodology, are necessary for introducing functional materials into electronic and magnetic devices.

In this work, suitable Metal Organic Chemical Vapor Deposition (MOCVD) approaches have been used to fabricate the above mentioned complex oxide thin films. Thin film deposition by MOCVD is of great and increasing interest of a wide number of materials ranging from metals to insulators, because of advantages such as composition control, high film densities, film uniformity, and potential matching to large wafer sizes. In all cases the appropriate conditions for the epitaxial growth have been found in order to improve the quality of the interface and special emphasis has been placed upon the importance of suitable precursors, deposition parameters and interfacial characterization. It is important to underline thatthe success of a process based on a chemical reaction depends critically on the availability of volatile, thermally stable precursors that exhibit high and constant vapour pressures, since poor performances affect the film properties. Therefore, an accurate knowledge of the physical properties and thermal behaviour of precursors is of fundamental relevance for the optimization of processes in the perspective of achieving uniform and reproducible film growth. In regard to the thermal analysis of the compounds the characterization has been carried out through thermogravimetric experiments both under atmospheric and low pressures and differential scanning calorimetry (DSC). The physical-chemical behaviour of the films depends on the film structural characteristics, such as crystalline structure of the deposited phases, chemical composition, uniformity and eventual interactions among substrate and overlayer. Deposited films have been studied by X-ray diffraction (XRD) to determine the structural nature. Additional information regarding the epitaxial growth of thin film has been obtained using TEM (Transmission Electron Microscopy) and pole figure analysis. The film composition and purity have been assessed by energy dispersive x-ray analyses EDX and X ray photoelectron spectroscopy (XPS). XPS depth profiling has been used to determine the vertical homogeneity of the sample. Morphological properties of thin films have been investigated through field emission scanning electron microscopy (FESEM).In all cases the MOCVD routes have shown great flexibility and proven to be a really intriguing challenge for implementation on large scale processes that could be superior or, at least, complementary to other methodologies. The functional properties have been assessed using consolidated national and international.

In conclusion , the research activity has been carried out as follow:

- Synthesis of chemical precursors suitable for the MOCVD growth of the films;
- Optimization of the MOCVD processes in order to determine the most critical factors for a reproducible deposition of the functional perovskite of interest:$CaCu_3Ti_4O_{12}$, $BiFeO_3$, $LaCoO_3$, $BaCeO_3$, $Pr_{1-x}Ca_xMnO_3$;
- Accurate control of the composition and structural/morphological properties of deposited films;
- Rationalization of the relationship processing parameters/film properties;
- Study of the functional properties of materials

Chapter 1 : Perovskites

The term perovskite indicates the class of compounds which have the same type of crystal structure as $CaTiO_3$.It was used for the first time for $CaTiO_3$in honour of its discoverer Perovskii.

The perovskite crystal structure was first described by V.M. Goldschmidt in 1926,[1] in his work on tolerance factors that represents a milestone on the exploration of the perovskite family of materials.[2]

Despite the simplicity of perovskite crystal structure, this family of materials shows an enormous variety of structural modifications and variants, that in turn infer several and important technological properties. Thus, they can be employed in several micro-electronics applications[3,4]such as memory elements or in microwave devices, in solid oxide fuel cells, such as electrolytes[5] or cathodes[6], in resistive and magnetic data storage[7], in sensor electronics and spintronic devices.[8,9]These characteristicsmake the perovskite oxide probably the most studied family of oxides in the materials science.

1.1:The crystal structure of perovskite

The ideal perovskite-type structure ABO_3(Fig.1.1.1),where A is the larger cation and B is the smaller cation, is cubic with space groupP_{m3m}. This structure consists of a three-dimensional framework of corner-sharing BO_6octahedra in which the A cations reside in the dodecahedral sites surrounded by twelve oxygen anions. Only very few perovskites have this ideal symmetric cubic structure at room temperature, but many of them acquire this ideal structure at higher temperatures.

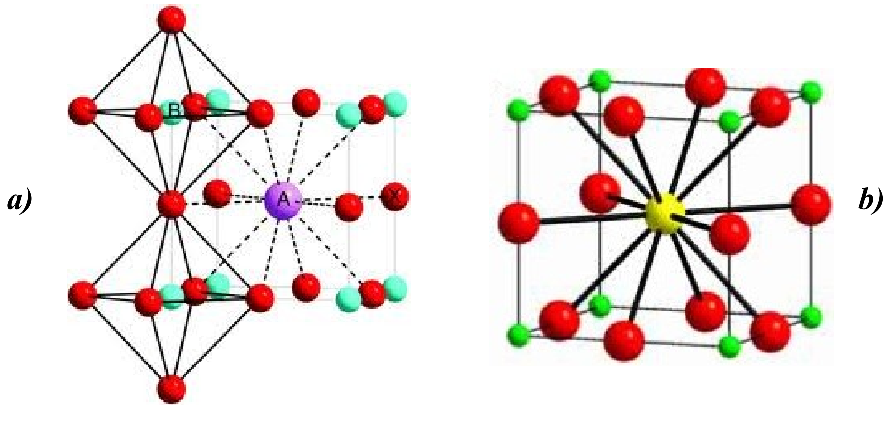

FIG.1.1.1 Ideal cubic perovskite structure ABO_3: (a) three dimensional net of corner sharing $[BO_6]$ octahedra (b) B ions in the twelve fold cavities in between the polyhedra.

Most perovskites are distorted and do not have the ideal cubic structure. Goldschimdt introduced the so-called “tolerance factor” (t)to indicate the “stability” of perovskite structures. The tolerance factor has been calculated [eq. (1)] taking into account the crystal ionic radii from Shannon[10] with a six coordination

$$t = (R_A + R_O)/\sqrt{2}(R_B + RO) \text{ eq. (1)}$$

where R_A, R_B, and R_O are the ionic radii of A ion , Bion and O^{2-} ion in the crystal. Note that to fit the structure correctly in the Goldschimdt perovskite classification, ionic radii values of ions six-coordinated have to be considered, even though this may not represent the correct coordination number in perovskite. In the ideal cubic crystal structure t = 1.If the A ion is smaller than the ideal value then t becomes smaller than 1. As a result the[BO_6] octahedra will tilt in order to fill the space. However, the cubic structure occurs if$0.89 < t < 1$.[11,12]Lower values of t will lower the symmetry of the system and hexagonal variants of the structure are stable. On the other hand, if t is larger than 1 due to a large A or a small B ion, a different structure is observed.

Goldschmidt underlined that the perovskite structure is stable only if the t parameter lies between 0.8 and 1. A deviation of t value from 1 indicates the likely formation of a distorted perovskite structure. The distortion is due to a rotation (tilt) of the oxygen octahedral (Fig.1.2). The various structures that are formed depend on both the magnitude and the relative rotation of the octahedra around the crystallographic axes.

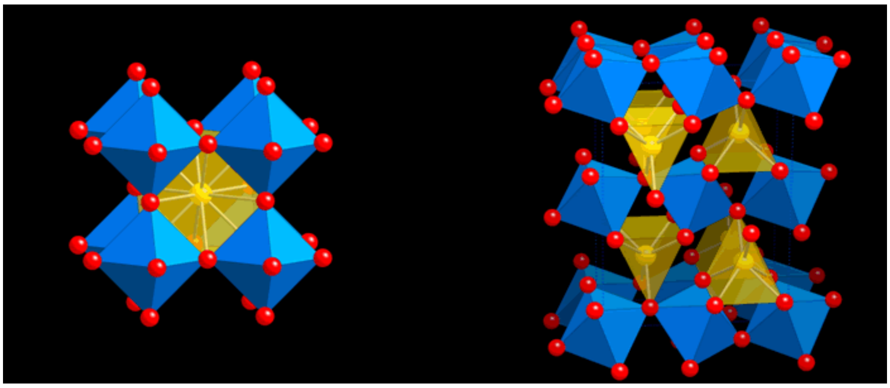

FIG.1.1.2 Rotation (tilt) of the oxygen octahedral [BO_6]

Further importantfactors, that are responsible for the distortion, is the changing in the composition from the ideal ABO_3. The perovskite structure is known to be very flexible because of the wide range of ions and valences that can be varied or partially replaced in both

A and B positions, leading to the large number of known compounds with perovskite or related structures.

These complex perovskites have $A_{1-}A'_xBO_3$, $AB_{1-y}B'_yO_3$or $A_{1-}A'_xB_{1-y}B'_yO_3$formulas. The A′ and B′ are termed dopant species. The insertion of a dopant specie may modify some properties depending on the doping fraction x or y.

In some perovskites, the distortion of the structure can be assigned to Jahn–Teller effect active ions at the B position. For example in the perovskite manganites, with the general formula $AMnO_3$, where the nominal electronic configurations of Mn^{3+} ion is $3d^4$ and it contains four d electrons, the $3d^4$ electrons divide up into 3 t_{2g} and 1 e_g electron. The odd number of electrons in the e_g orbital causes an elongation of the $[MnO_6]$ octahedron. Therefore, according to the Jahn-Teller theorem the $Mn^{3+}O_6$ groups are energetically unstable towards distortions aiming to reduce the total energy of the system, as a consequence of a lifting of degeneracy of the e_g levels.

1.2 Properties of perovskites

The functional properties of perovskites, discovered over 50 years ago, have been widely discussed in several review.[13-15]As already mentioned, the structural properties of perovskite materials lead to a huge range of innovative properties, such as ferromagnetism, colossal magnetoresistance, piezoelectricity, ferroelectricity, multiferroicity, metal-insulator transitions, superconductivity, ionic and electronic conductivity. One reason for this is that nearly all cubic perovskites are unstable to energy-lowering structural distortions[16] and hence typically have rich structural phase diagrams.

This variety of electronic and magnetic properties is not only due to their chemical flexibility, but also to the complex character that transition metal ions play in certain oxygen coordination architectures.[17]The magnetic and electronic correlations are usually due to unfilled 3d electron shells of the transition metal, while dielectric properties are connected with filled 3d electron shells.

Exchange interactions are the main phenomenon at the base of magnetic properties. In the ideal cubic perovskite structure, each oxygen is shared by two B^{3+}ions,forming a B-O-B angle of 180°. Such a configuration is favorable for superexchange interactions between magnetic B^{3+}cations. This exchange usually results in antiparallel coupling of nearest-neighbor magnetic moments. When the B^{3+} ions are in two sublattices ($A_2BB'O_6$) other spin arrangements are possible.

If B' is a diamagnetic ion, the B^{3+} ions are aligned antiferromagnetically, and the most important exchange mechanism is believed to be a longer range superexchange interaction through two oxygens of the type B-O-B'-O-B.

In regards to the electrical properties, the perovskites can act as metals, semiconductor, superconductors, and dielectrics. The electrical behavior in perovskites depends on the outer most electrons, which may be localized at specific atomic sites or may be collective. For example in $LnMnO_3$perovskitethe charge carriers, would be holes, hopping among localized levels, and lead to an abrupt change in conductivity and in magnetic susceptibility as a function of temperature.

Another important aspect that influences the physical properties is the non-stoichiometry.[18,19] In order to maintain the electroneutrality (the sum of charges of A and B equals the total charge of oxygen anions)an appropriate charge distribution of the form $A^{1+}B^{5+}O_3$,$A^{2+}B^{4+}O_3$, or $A^{3+}B^{3+}O_3$ occurs in perovskite. However, deficiencies of cations at the A- or B-sites or of oxygen anions are frequent, which results in defective perovskites. Oxygen deficiency is more common than those involving cationic vacancies.

The former composition can be considered as an anion-deficient perovskite with one-sixth of the oxygen ions being vacant. Oxygen vacancies are ordered in alternate (001) BO_2planes of the cubic structure such that alternate [110] rows of oxide anions are missing.

Thereby, the properties and phase diagrams of a perovskite strongly depend on non-stoichiometries and even more on tilting or distortions of the $[BO_6]$ octahedra.

References

1V. M. Goldschimdt, Akad. Oslo. J. Mat. Natur. 2 (1926) 7.

2 A.S. Bhalla, R. Guo, R. Roy ,Mat. Res. Innovat. 4 (2000)3-26

3 R. Ramesh, D.G. Scholm, J. Solid State Chem. 33 (2008) 1006.

4C .K. Campell, J.D. Van Wyk, P. Wolmarans, IEEE Trans. Compon. Packag. Technol.27 (2004) 311

5E. Fabbri, D. Pergolesi, E.TraversaChem. Soc. Rev.,2010,39, 4355–4369

6 A. Yu Zuev, V. V. Sereda, D. S. Tsvetkov, J. Electrochem. Soc. 159 (2012) F594

7Murakami Y, Kasai H, Kim J J, Mamishin S, ShindoD,Mori S, Tonomura A , Nature Nanotechnol. 5(2010) 37Y

8 N. A. Spaldin, S.-W. Cheong, R. Ramesh, Physics Today 63 (2010) 38

9T. Choi, S. Lee, Y. J. Choi, V. Kiryukhin, S. W. Cheong, Science324 (2009)63-66

10R. D. Shannon, *ActaCrystallogr. Sect. A* 32 (1976) 751.

11 A.F. Wells, Structural Inorganic Chemsitry, Oxford Science publications.(1995)

12U. Müller, Inorganic Structural Chemistry, Wiley &SonsLtd.(1993).

13 M. A. Pena˜, J. L. G. Fierro Chem. Rev. 101 (2001) 1981−201

14 N.,Nurxat; S. KaiNanoscale5(19)(2013) 8752-8780.

15Benedek N. A.; Fennie C. J, Condensed Matter (2013) 1-12

16Rabe, K. M.; Ph: Ghosez, Physics of Ferroelectrics: A Modern Perspective; Springer-Verlag, (2007).

17P. Lemmens and P. Millet, Spin – Orbit – Topology, a triptych, in “Quantum Magnetism”, Springer, Heidelberg, (2004).

18Rao, C. N. R.; Gopalakrishnan, J.; Vidyasagar, K. Indian J.Chem. Sect. A 1984, 23A, 265.

19Smyth, D. M. Annu. Rev. Mater. Sci. 15(1985) 329.

Chapter 2: Giant dielectric constant $CaCu_3Ti_4O_{12}$perovskite films

In the last years, the technological development and the increasing request for new miniaturized electronic devices has focused the attention on the search of new innovative and more performant materials. In fact, the performance of these electronic devices should progress very rapidly and their technological improvement requires higher speed and lower power consuming. In order to have better performances, one of the most popular method is the downsizing of components. In this respect, the development of new techniques for the synthesis of thin films has allowed the application and integration of new multifunctional oxides in complex multilayer devices[1].

Dielectric thin films are among the most required materials for this kind of devices and in particular for fabricating capacitors.

Dielectric materials are electrical insulator and their main characteristics are: i) high dielectric strength (must support high voltages without degrading or become electrical conductors) and ii) low dielectric loss (under alternating electric field there should be no loss of electrical energy).

Dielectric material can be polarized by an applied electric field. When a dielectric is placed in an electric field, electric charges do not flow through the material as they do in a conductor, but only slightly shift from their average equilibrium positions causing dielectric polarization. Because of dielectric polarization, positive charges are displaced toward the field and negative charges shift in the opposite direction. This creates an internal electric field that reduces the overall field within the dielectric itself. The dielectric constant is closely related to the polarization: electronic polarization, dipolar polarization, ionic polarization and space charge polarization. In the last years, materials with high dielectric constants (ε) have received ever-increasing attention for their wide use in technological applications, such as capacitors and memory devices. In particular, capacitor applications require highly insulating materials and the increasing of smaller and faster microelectronics devices is associated with similarly higher values. In an attempt to miniaturize device size, much attention has been devoted to discover materials with high relative permittivity, low dielectric loss and low-temperature coefficient of the permittivity. In particular, capacitor applications need high permittivity materials having also great structural stability. A large ε is based on collective polar displacements of the metal ions with respect to the oxygen sublattice and is a highly nonlinear and anisotropic phenomena.

Several studies on the perovskite related calcium copper titanate, $CaCu_3Ti_4O_{12}$ (CCTO), have demonstrated that this material presents the so-called giant dielectric permittivity, having an impressive dielectric constant value of 10^5 working at 1 MHz, which remains constant in the 100-600 K temperature range and depends slightly on work frequency in the 10^2-10^5Hz range.[2-4]In addition, CCTO does not show ferroelectric transition or relaxor behavior. These intriguing properties render the CCTO material a real attractive alternative to the currently used ferroelectrics which in turn possess lower dielectric constant values having a stronger temperature dependence. A number of theoretical studies and experimental observations have attempted to elucidate this remarkable dielectric property.[5-7]The most widely accepted mechanism for the giant dielectric constant in CCTO ceramics is the internal barrier layer capacitor (IBLC) model invoking semiconducting grains and insulating grain boundaries.[8-12] These studies indicated that the huge dielectric constant is probably not an intrinsic property, but could be due to some extrinsic phenomenon. Some theories, on the other hand, correlate the CCTO high ε value to its peculiar crystal structure,[13] in particular high permittivity may arise from the local dipole moments associated with off-center displacement of Ti ions**.** Until now, however, most of the experiments carried out have been on ceramic bulk materials, and only rarely have been reported data on the properties of CCTO thin films[14]. A decrease of the dielectric constant value is expected when moving from bulk to films, and some differences could be observed between epitaxial and polycrystalline thin films, which are characterized by the presence of many grain boundaries.

In order to choose substrates best suited for an epitaxial growth of the CCTO phase, the structural characteristics of this perovskite phase is reported in the following.

The CCTO compound belongs to the family of mixed oxides ACu_3TiO_{12} synthesized for the first time in the 1967.[15] The crystal structure (Fig 2.1) of CCTO is a body-centered cubic system with four $ATiO_3$ perovskite-type formula per primitive cell (where A is either Ca or Cu).[16]The unit cell of CCTO has a lattice parameter of 7.405 Å at room temperature. The Ti atoms are octahedrally coordinated with the octahedra rotated the same amount around the [100], [010], and [001] axes. The tilt is fairly large causing 3/4 of the A atoms, i.e., the Cu atoms, to be four-coordinated with the four oxygen atoms forming a square with a Cu atom at its center. The distance from the Cu atom to each of the four surrounding oxygen atoms is 1.98 Å. The remaining A atoms, i.e., the Ca atoms have a bcc arrangement, and each is surrounded by 12 oxygen atoms at a distance of 2.61 Å.

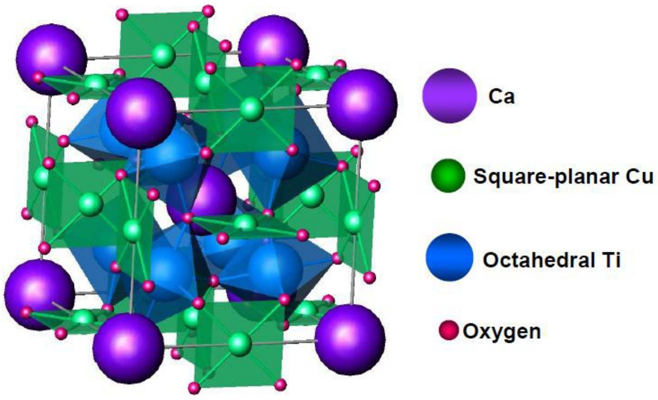

FIG.2.1 Crystal structure of CCTO

CCTO thin films have been epitaxially grown on various substrates by Pulsed Laser Deposition (PLD)[17-19] and by Metal-Organic Chemical Vapor Deposition (MOCVD).[20-22] MOCVD growth takes advantage of simpler, less costly equipment, ready scalability, and higher throughput as compared to conventional physical vapor deposition techniques.

Previously, CCTO thin films have been deposited by MOCVD approach, using an innovative, single, molten multimetal source on conventional $LaAlO_3$ (001) substrate[23] and on and $IrO_2/Ir/TiO_2/SiO_2/S$ [24] technological substrates; the structural, the compositional and optical investigations of these epitaxial film pointed out to the formation of high quality CCTO materials.

In the present work, CCTO thin films were obtained by MOCVD technique, on oriented $SrTiO_3$ (STO) (001) substrates, in order to grow CCTO material in the form of epitaxial films,[25] and on conductive oxide electrodes, the $La_{0.9}Sr_{1.1}NiO_4/LaAlO_3$ (LSNO/LAO) stack.[26]

2.1 Growth of CCTO thin films on STO (100) substrates

2.1.1Thermal characterization of precursors and MOCVD growth process

The growth of epitaxial oxides is always a challenging aim, depending on the lattice mismatch and chemical complexity of the perovskites. The present MOCVD process for the fabrication of CCTO thin films relies upon a “unique” approach based on the use of a molten multi-component precursor source consisting of a 1:1:3 mixture of $Ti(tmhd)_2(O\text{-}iPr)_2$, $Ca(hfa)_2\cdot$tetraglyme[27] and $Cu(tmhd)_2$precursors. The MOCVD apparatus is a horizontal hot-wall reactor (Fig. 2.1.1). The volatile source mixture was loaded in a resistively heated alumina boat at 115°C and was transported through the reactor with an argon flow rate of 150 sccm in the presence of a 200 sccm oxygen reaction.

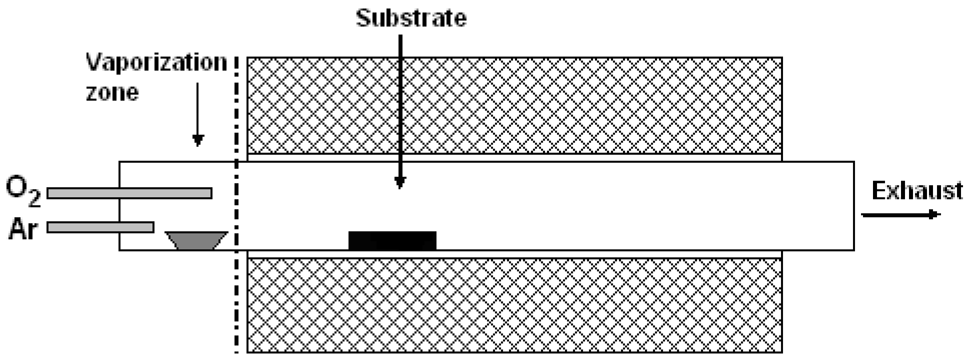

Fig. 2.1.1.1 MOCVD horizontal hot-wall reactor

The comparative study of the multi-component Ca:Cu:Ti mixture has been performed by TG and DSC measurements. The dynamic TG (Fig.2.1.1.2a), under reduced pressure (20 Torr) and atmospheric pressure, curves indicated that the sublimation/evaporation for the mixture occurs in a single step with low residues (≤1%) at 450 °C. Moreover, isothermal TG analyses in the 90–140 °C (Fig.2.1.1.2b) under reduced pressure (20 Torr), showed a linear behavior for each single precursor in the entire investigated temperature range, while the precursor mixture shows a non linear behavior at temperatures higher than 120 °C, thus suggesting that contributions of individual precursors may prevail giving rise to differential vaporization rates. However, at temperatures higher than 100 °C the precursor mixture possesses a high volatility and, therefore, it can be safely used up to 120 °C.

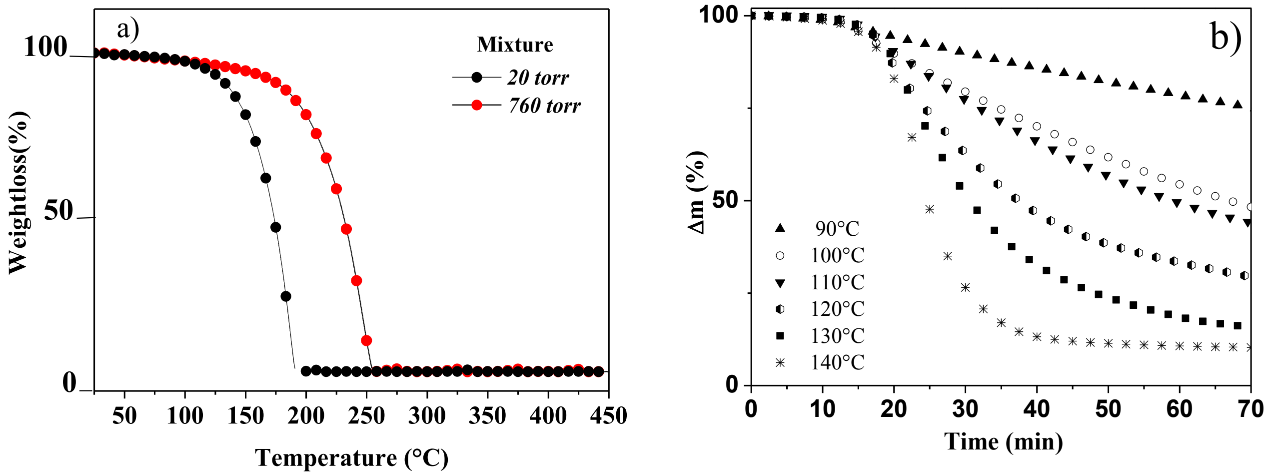

Fig.2.1.1.2 TG curves (a) and isothermal curves (b) of the multicomponent Ti(tmhd)$_2$(O-iPr)$_2$, Ca(hfa)$_2$•tetraglyme Cu(tmhd)$_2$

Other useful information has been obtained from calorimetric data (Fig. 2.1.1.3). Calcium and copper precursors show two endothermic DSC peaks due to melting (94.0 °C and 198.6 °C, respectively) and two endothermic peaks due to evaporation from melts (200–280 °C and 220–250 °C). The DSC curve (Fig.2.1.1.3) for the Ti precursor shows two peaks associated with two crystal change structure at 60 °C and at 164 °C, while the higher temperature peaks at 205 °C and 244 °C are related to melting and evaporation, respectively.[28] The molten Ca:Cu:Ti mixture shows a small temperature peak (60°C) associated with the first structure change of the $Ti(tmhd)_2(O\text{-}iPr)_2$ component and an higher temperature peak at 88.7°C associated with the $Ca(hfa)_2$ tetraglyme melting. Some small features in the 120–175 °C range may be related to dissolution of Ti and Cu components. Finally a broad endothermic peak in the 180–240 °C temperature range is associated with the mixture vaporization from melt. Note that, the endothermic peaks expected for the $Cu(tmhd)_2$ and $Ti(tmhd)_2(O\text{-}iPr)_2$ melting are not observed. Therefore, the $Ca(hfa)_2\cdot$tetraglyme precursor acts, on melting, as a solvent for the Ti and Cu sources and forms a homogenous mixture of the three precursors. These results show that the Ca:Cu:Ti mixture can be used as a single multi component precursor since it allows a stable evaporation from the melt with a vaporization rate that remains constant during the vaporization time up to 120 °C.

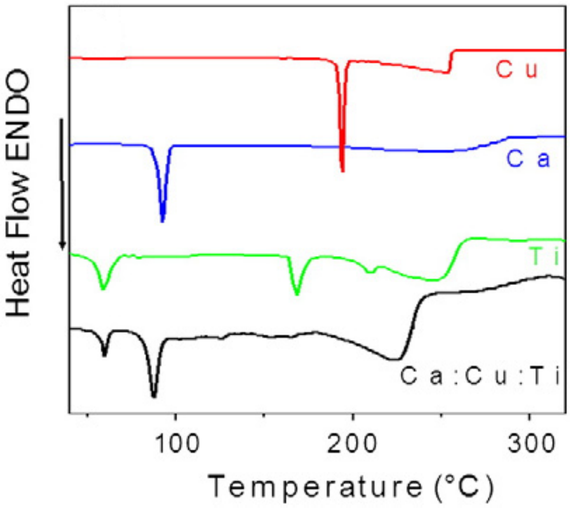

Fig.2.1.1.3 DSC curve (a) of the multi component $Ti(tmhd)_2(O\text{-}iPr)_2$, $Ca(hfa)_2$•tetraglyme $Cu(tmhd)_2$

CCTO films have been deposited using the present mixture by two different MOCVD processes; a two-step, in situ process (Fig.2.1.4a), and a single-step process (Fig2.1.4b).[24, 29, 30] The two-step in-situ process consists of the deposition of an almost amorphous matrix and the subsequent in-situ annealing. In particular, the first deposition step was carried out at 600° C, while the second, in-situ annealing step was performed at 900° C The single-step approach was based on the direct deposition of the CCTO film at 750 ° C.

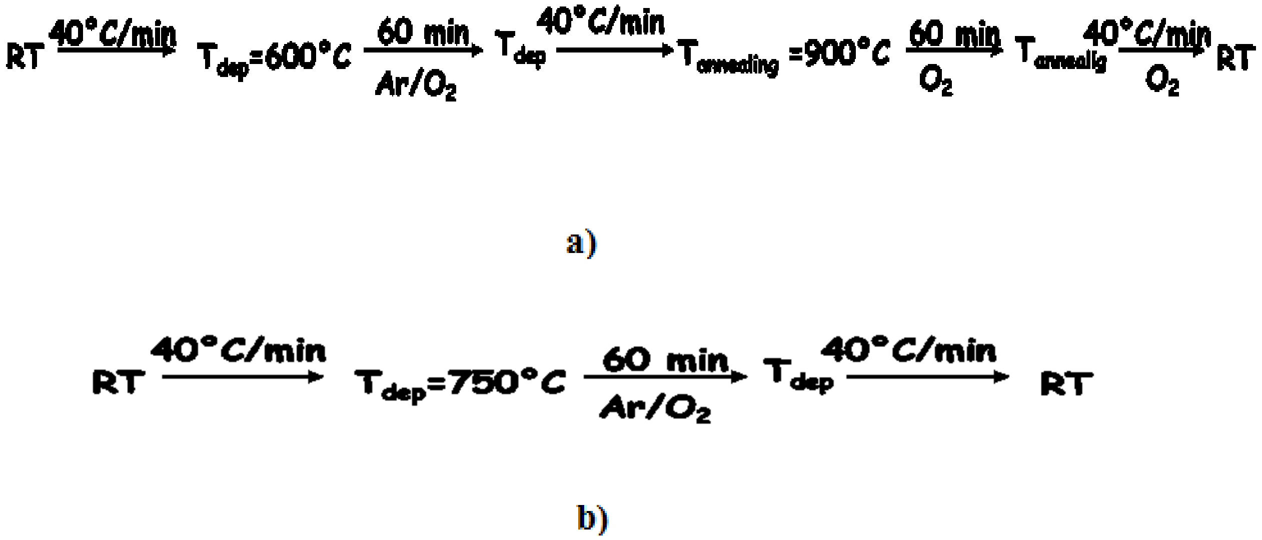

Fig.2.1.1.4 MOCVD a two-step in situ process (a), and a single-step process(b)

2.1.2 Structural and morphological characterization of CCTO thin Films on $SrTiO_3$ substrate.

First attempts on STO substrates were carried out using the two-step, in-situ process. The XRD pattern (Fig.2.1.2.1a) of the deposited films shows the formation of two different compounds, namely CCTO and $CaTiO_3$ (CTO). In fact, the peaks at 23.30° and 47.62° can be related to the 001 and 002 reflections of the CTO phase, while the peak visible at 49.52° corresponds to the 004 CCTO reflection. Thus, the principal peaks can be related to the formation of oriented (001) CTO films and only one peak of lower intensity corresponds to the CCTO phase. While the peaks at 22.78° and 46.48 ° are due to the STO substrate contribution with 001 and 002 reflections respectively.

The preferential formation of the $CaTiO_3$ phase can be explained on the basis of the larger lattice mismatch (≈6%) between CCTO and $SrTiO_3$ than that between $CaTiO_3$ and the $SrTiO_3$ substrate (0.4%). The film is characterized by quite rounded grains, about 150 nm wide (Fig.2.1.2.1b), homogeneously distributed.

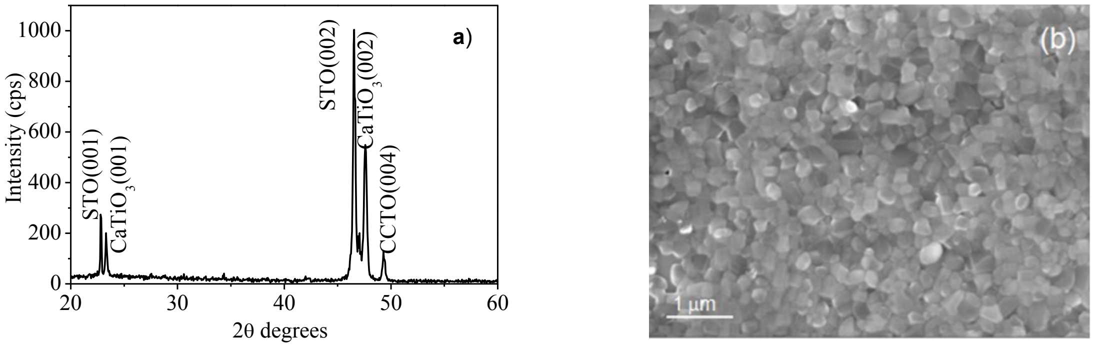

Fig .2.1.2.1a) XRD pattern and b) FE-SEM image of a film deposited on $SrTiO_3$ substrate by the two-step in-situ MOCVD process.

To understand what happens during the two step MOCVD process, the structure and the morphology of film, after the first deposition step at 600°C, was studied. The XRD characterization of CCTO films deposited at 600°C consist of a quite amorphous matrix; in fact the XRD pattern recorded using the Bragg-Brentano Θ-2Θ configuration shows only those peaks due to the substrate, while the XRD analysis in grazing incidence mode (Fig. 2.1.2.2) shows broad low-intensity peaks due to the formation of the CuO phase. Thus films deposited at 600 °C can be considered a roughly amorphous matrix of Ca-Cu-Ti oxide. The FE-SEM investigation (Fig. 2.2.2b) shows nanocrystalline and not well-defined aggregations of grains. Finally, to evaluate the composition of both the deposited (600°C) and annealed (900°C) films energy dispersive X-ray (EDX) analyses have been carried out on films deposited on Pt substrate simultaneously to those obtained on perovskite substrates. The use of platinum is required because of the overlap between Ti signals from the film and the substrates. EDX spectra indicated that the 1:1:3 Ca:Cu:Ti ratio in the precursor mixture results in a 1.1:2.7:3.9 Ca:Cu:Ti ratio in both the amorphous matrix and in the CCTO/CTO mixture thin films. Best results were obtained using one step process at 750°C .

The single step depositions have not been carried out at 900°C, because at this temperature CCTO films poor in copper are obtained, whatever the stoichiometric ratio of the precursor mixture. This is likely due to the decomposition at high deposition temperatures of the $Cu(tmhd)_2$ precursor on the reactor walls before reaching the substrate surface. In the case of single step deposition at 750°C to obtain the correct stoichiometry in the film it has been necessary to change the initial 1:1:3 Ca/Cu/Ti precursor mixture.

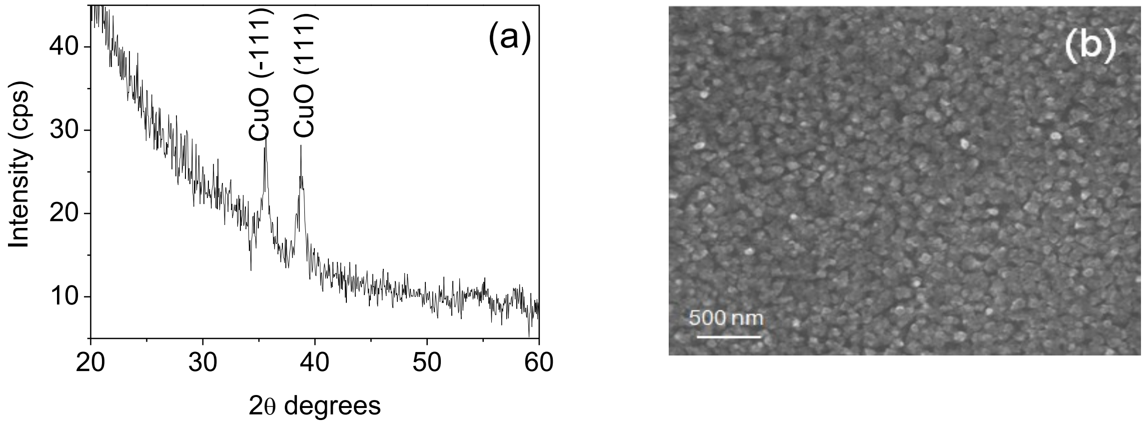

Fig.2.1.2.2 a) XRD pattern and b) FE-SEM image of the film deposited on SrTiO$_3$ substrates at 600°C.

In fact, EDX analysis, carried out on films deposited at 750°C simultaneously on a Pt substrate, showed that Ca/Cu/Ti precursor mixture ratio of 1:1.3:3.2 provides a nearly correct stoichiometry (1.0:3.2:4.2 Ca/Cu/Ti) in the film. The new operative parameters, deposition temperature and stoichiometry of the precursors in the mixture, lead to pure epitaxial CCTO film. In fact, the XRD (fig. 2.1.2.3a) pattern of thin films shows the presence of the unique peak at $2\Theta=49.54°$, that indicates that only CCTO <001> oriented film has been formed. To study the epitaxial grow of the CCTO film on the STO substrate, ϕ-scans on a four-circle X-ray diffractometer have been carried out. The measurements on the (001)-oriented CCTO film and the STO substrate have been carried out consecutively in order to establish the in-plane relationship of the CCTO film with respect to the underlying STO substrate. In the ϕ-scans (from 0 to 180°) the CCTO (220) reflection ($2\Theta=16.90°$) and STO (110) reflection ($2\Theta=32.38°$), both at tilt angles of 45°, have been used as poles. The expected two peaks due to CCTO{110} planes are perfectly coincident with STO {110} ϕ positions (Fig2.1.2.3 b). This clearly demonstrates that the CCTO unit cell is not rotated in the plane with respect to the STO substrate, for example the [100] and [010] axis directions are aligned for both the film and the substrate. The mean full width at half maximum(FWHM) of the CCTO ϕ peaks is 3.78° indicating a good degree of epitaxy.

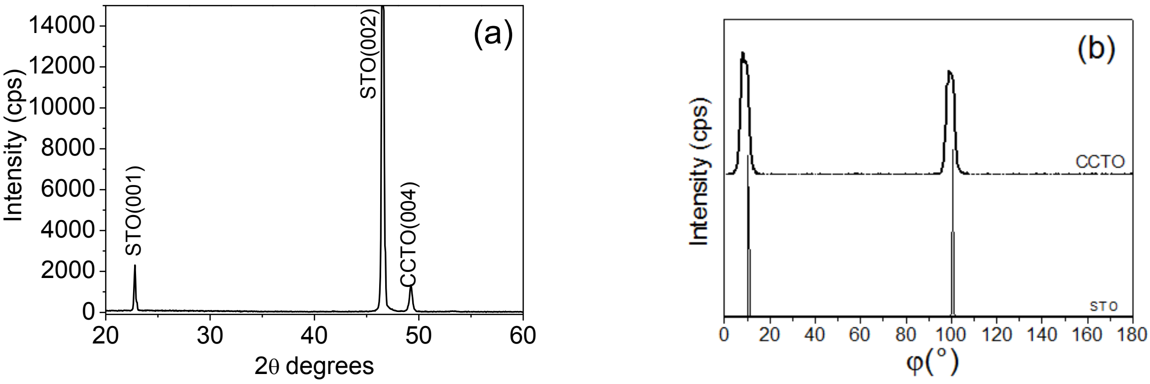

Fig.2.1.2.3 a) XRD pattern and b) ϕ-scan measurements of a CCTO film and the SrTiO$_3$ substrate.

The FE-SEM in plane (Fig.2.1.2.4a) and the cross section (Fig 2.1.2.4b) images show the formation of a continuous CCTO film consisting of quite square grains, well-ordered in the plane. The lateral size of each grain is about 200nm.

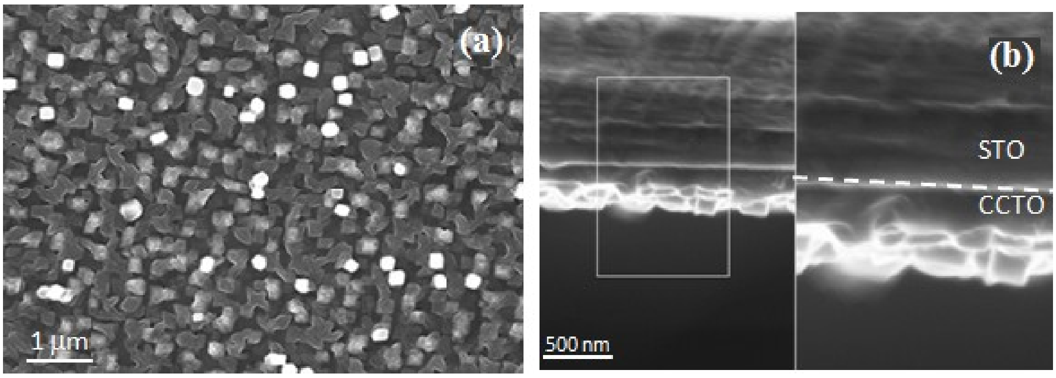

Fig.2.1.2.4 a) FE-SEM images of the surface morphology, and b) of the cross-section of the CCTO film deposited on SrTiO$_3$ substrates at 750°C.

To confirm the epitaxial growth of the CCTO film transmission electron microscopy (TEM) analysis have been carried out. The bright-field cross-section TEM image (Fig.2.1.2.5a) shows a homogeneous film thickness of 220 nm. The calculated growth rate is 3.7 nm min^{-1}and it is comparable to that found for the two-step process (growth rate=3.3 nm min^{-1}). The high-resolution (HR)TEM image (Fig. 2.1.2.5b) shows a quite sharp film/substrate interface which indicates that no chemical interaction occurred. Figures 2.1.2.5 c and 2.12.5 d show the selected-area electron diffraction (SAED) patterns of the substrate and of the CCTO film observed with an incident electron beam perpendicular to the sample cross-section. The cross-section SAED pattern, taken in an area covering both the substrate and the film, is a simple superposition of the CCTO film and STO substrate spots. The obtained SAED pattern reveals a perfect c-axis alignment and confirms that the CCTO films grow epitaxially.

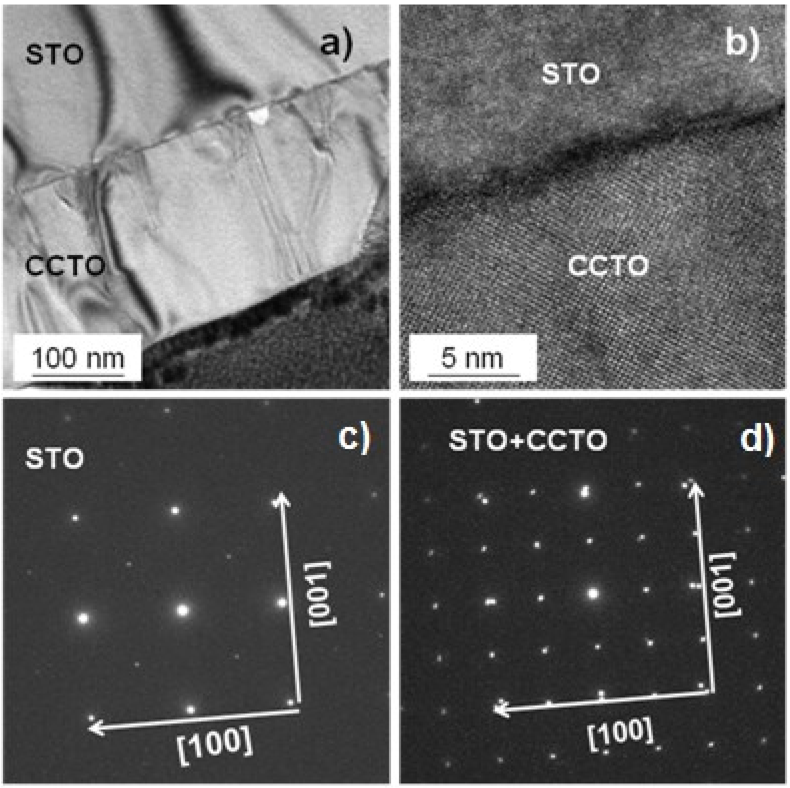

Fig.2.1.2.5 a) Low-magnitude, bright-field image of the cross-section CCTO film/SrTiO$_3$ substrate. b)HRTEM image of the CCTO/SrTiO$_3$ interface. c) SAED patterns of the (001) SrTiO$_3$ substrate and d) of the CCTO/SrTiO$_3$.

Insights into the composition of deposited films have been provided using EF-TEM chemical maps of the CCTO film obtained at 750°C. The zero loss-energy image (Fig.2.1.2.6) shows the presence of some crystalline and distorted grains embedded in the well-oriented CCTO film. The chemical nature of these distorted grains has been determined by the chemical maps of each CCTO component. By comparison of the Ca, Cu, and Ti signal intensities it can be concluded that the crystalline grains likely consist of copper oxide grains. In fact, the intensity of the copper signal increases in correspondence with crystalline grains. On the other hand, Ti and Ca signals are well-distributed all over the matrix. The presence of the CuO phase was not detected by XRD measurements, probably because of the quite low concentration.

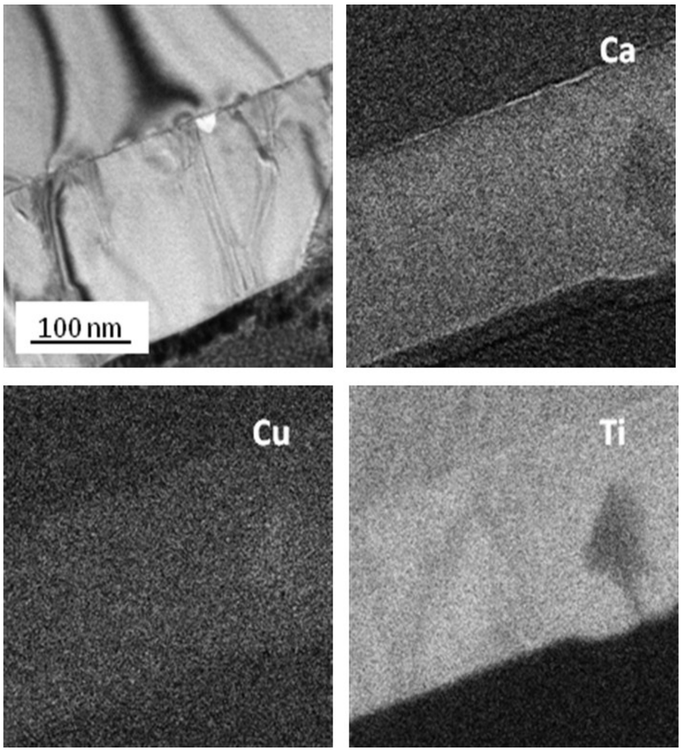

Fig.2.1.2.6 Chemical maps of a CCTO film deposited at 750°C performed by EF-TEM.

In summary , the deposition conditions for the formation of pure CCTO on $SrTiO_3$ (100) substrates have been optimized: the two-step procedure provided no pure CCTO phase growth, while the single-step process at 750 °C produced pure and (001) oriented film. Kinetic and thermodynamic factors determine the obtainment of the pure CCTO films. In fact, in the two-step growth, a kinetic contribution further supported by the favorable lattice match determines the stability of the CTO phase. Both CCTO and CTO phases, as well as the $SrTiO_3$ substrate material, are perovskite-type complex oxides. There is a competition between CCTO and CTO based on lattice match between deposited phases and substrate. Considering a typical cube-on-cube growth of (00l)-textured CCTO films on a $SrTiO_3$ substrate (a = 3.905 Å), one CCTO unit cell will match four $SrTiO_3$ (001) unit cells (fig.2.1.2.7 a, b). There is, therefore, indication of a 5.3% lattice mismatch, while the CTO phase has a lattice parameter of a=3.823 A° and a mismatch of 2.1% with respect to the $SrTiO_3$ substrate. Thus, based only on the mismatch between CCTO and CTO with the STO substrate, the growth of CTO should occur independently on the growth process, while in the one-step growth, thermodynamic factors prevail: CCTO is thermodynamically more stable than the CTO phase.[31,32]

To confirm these consideration, a new experiment has been performed by annealing, at 900°C, the CCTO film obtained at 750°C. The XRD pattern and FE-SEM images (Figs. 2.1.2.8 a, b), recorded after annealing, show that neither structural nor morphological modifications of the CCTO film occurred; this experiment confirmed that the CCTO film is very stable at 900°C.

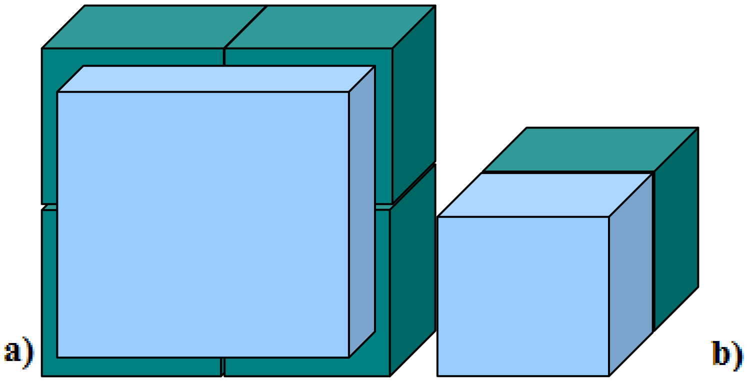

Fig. 2.1.2.7 Growth model of a) CCTO and b) CTO on $SrTiO_3$ substrate.

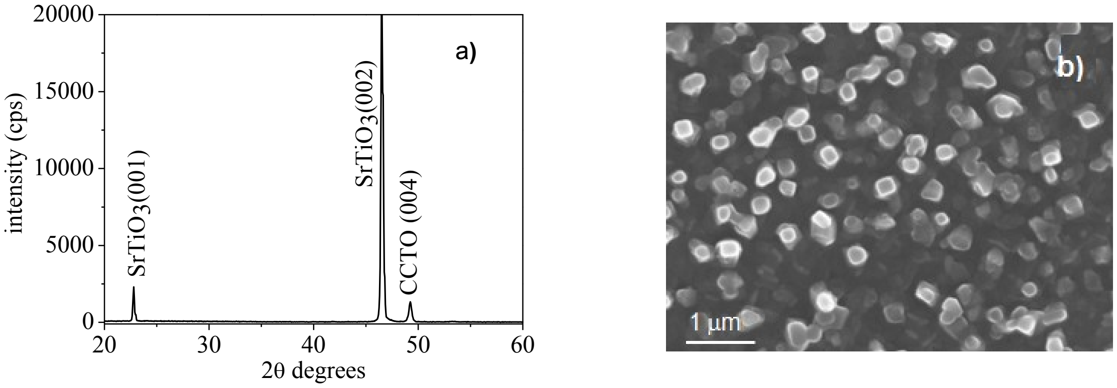

Figs. 2.1.2.8:a) XRD pattern and b) FE-SEM image of a CCTO film annealed at 900°C after deposition on $SrTiO_3$ substrate by the single-step process (750°C).

2.2 Deposition of CCTO thin films on LSNO(100) electrode

In order to build capacitor devices, it is of course required to fabricate bottom and top electrodes. In particular, the growth of oriented CCTO thin films will need the availability of a bottom electrode, stable at high deposition temperature and able to promote its epitaxial growth. These requirements could be best met by oxide electrodes having structures similar to perovskites. The $La_{0.9}Sr_{1.1}NiO_4$ (LSNO) has all the described requirements. LSNO structure and cell parameters are compatible with LAO and CCTO, the lattice mismatches being 0.8% and 3% to LAO and CCTO, respectively. Furthermore, it has been shown that LSNO grows epitaxially on LAO.[33]Depositions of CCTO thin films on LSNO electrode have been also carried out by a single step MOCVD approach at 750°C. The diffraction pattern (Fig. 2.2.1) consists of peaks at 2Θ =23.46° and 47.95° which have been related to the (001) and (002) reflections from the oriented LAO substrate, the peak at 2 Θ = 49.52° has been associated with the (004) reflection of the CCTO phase, and finally peaks are visible at 2 Θ = 30.83° and 64.39°, that cannot be assigned either to CCTO or to LSNO phase. Assignment of these peaks is not an easy task , but the second peak (64.39°) certainly represents the higher order reflection (00n*l*) of the peak at 30.83° (00*l*). Moreover, note that all the peaks related to the (00*l*) reflections of the LSNO , previously observed, are not present.

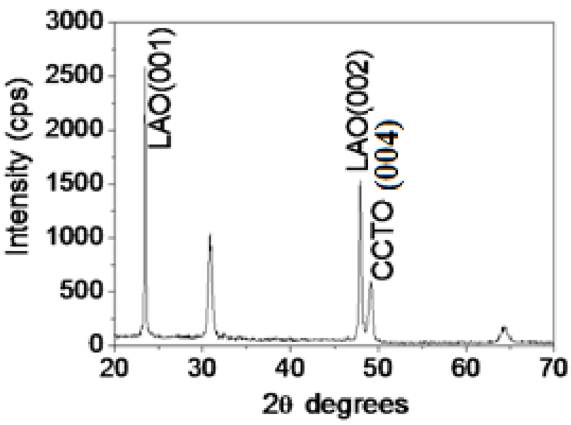

FIG.2.2.1 XRD pattern of a film deposited on LSNO substrate

FE-SEM and TEM investigations have been performed to obtain morphological details of the deposited film. The FE-SEM image shows the formation of a uniform CCTO (Fig. 2.2.2a) film with grains about 100 nm wide. The bright-field cross-section TEM image of a CCTO film deposited on LSNO/LAO stack show (Fig. 2.2.2b) the growth of a quite homogeneous film with a thickness value of about 200 nm. Moreover, an interesting detail is a ~50 nm thick layer, visible at the CCTO/LSNO interface, showing the same morphological aspect but a slightly darker contrast. The chemical composition of the CCTO film has been evaluated by EDX analysis, on a sample deposited on Pt electrode simultaneously to that deposited on LSNO/LAO(001) substrate. The use of Pt electrode is required because of the overlap between Ti K signals and La L signals from the substrate. EDX analysis indicated that a nearly perfect stoichiometry of CCTO films have been obtained using the present MOCVD process.

To evaluate if any interaction occurred in the CCTO/LSNO interface, the EF-TEM chemical maps (Fig.2.2.3) have been collected for all the components, Ca, Cu and Ti, of the deposited film and for La from the electrode and substrate. The Ni and Sr maps have not been recorded because of the overlap between the first window used for the Ni and Sr maps with the La M edge. This overlap causes an erroneous calculation of the background so that the Ni and Sr maps would not be correct. As evident in fig.2.2.3 elements, Ca, Cu and Ti of the CCTO film are well uniformly distributed, within the CCTO film; at the interface, Cu containing grains are visible, while the intensity of the titanium signal points out to the formation of a titanium containing layer reaching the CuO grains (as deducted by the Fast Fourier Transform (FFT) of their high resolution TEM image). By measurements the thicknesses in the Ca, Cu, Ti and La maps, it can be concluded that the stack is formed by: i) a 190 nm thick film containing Ca, Cu and Ti elements; ii) a 50 nm layer containing Ti plus CuO grains; iii) the LSNO electrode with a thickness, after the deposition, reduced to 75 nm.

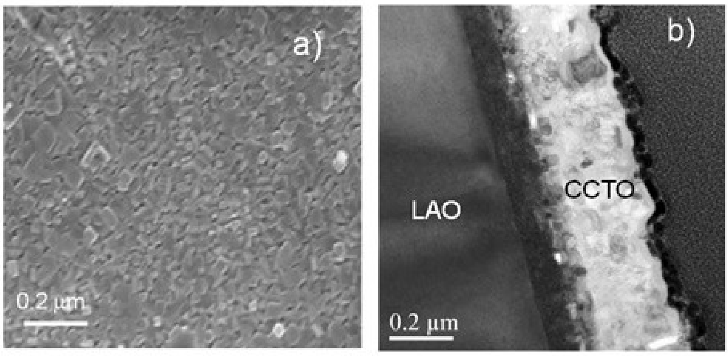

FIG.2.2.2 a) FE-SEM and b) TEM images of a film deposited on LSNO substrate.

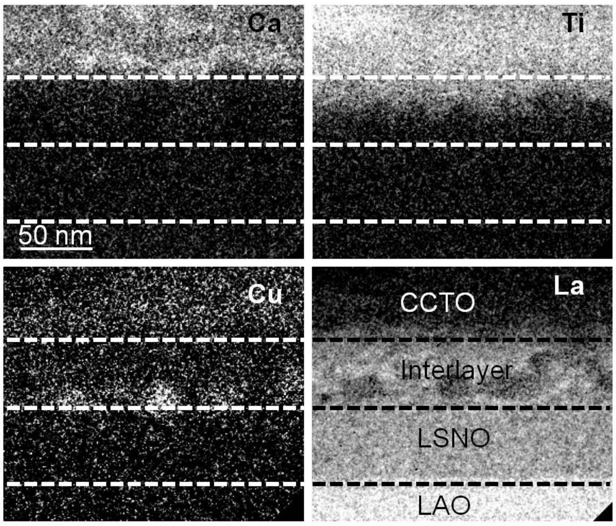

FIG.2.2.3 Chemical maps collected at the CCTO/LSNO interface by energy-filtered transmission electron microscopy

Detailed analyses of the LSNO electrode after the deposition, shown in Fig. 2.2.4, have been carried out through high resolution TEM (HR-TEM) investigation. The single crystal nature of the LAO substrate is evident, while many defects are present in the LNO electrode as pointed by the lighter and darker zones visible in the HRTEM image. The FFT of the HR-TEM image from both LAO substrate and the LSNO electrode demonstrated that the direction related to the 2.89 Å LSNO plane distance is parallel to the (001) LAO direction. The plane distance measured for the FFT of the LSNO corresponds to the unknown reflection (2θ= 30.83°) observed in the post deposition XRD pattern. Thus, also during the MOCVD process the crystalline quality of LSNO layer is degraded.

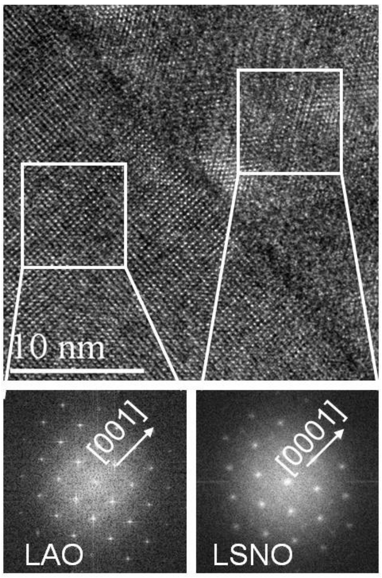

FIG. 2.2.4 High resolution **TEM image and SAED patterns of the LSNO/LAO interface after the MOCVD process**

In order to confirm this hypothesis, a new experiment has been designed. An annealing of the plain LSNO/LAO stack has been carried out under identical MOCVD operating conditions used for the CCTO film deposition. In Fig. 2.2.5 the XRD pattern of the annealed sample is compared with the pattern of the LSNO electrode. The presence of the peaks at 2θ= 30.83° and 64.39° is a definitive confirmation that the structural change is due to the MOCVD deposition conditions and cannot be related to a chemical interaction with the CCTO films.

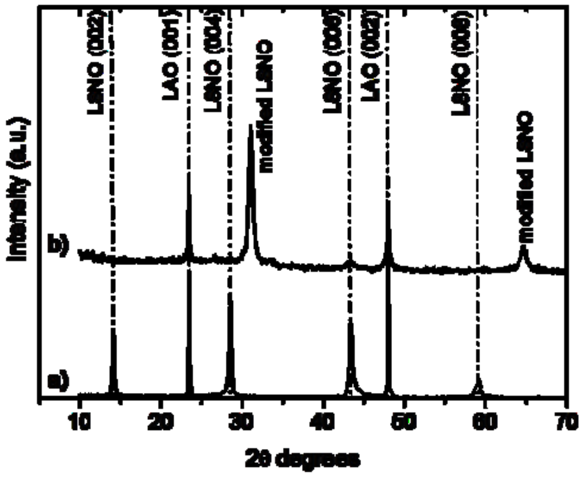

Fig. 2.2.5 XRD patterns of the LSNO/LAO stack before (a) and after (b) the annealing in the same conditions used during the MOCVD process.

The investigation of the structural modification of the LSNO electrode has been carried out by collecting several electron diffraction (Fig.2.2.6) along different zone axes. By comparison of the collected plane distance values and the expected ones, it might be concluded that the LSNO system did not change the tetragonal lattice cell in another lattice system. It is possible to hypothesize only the change in the orientation [110] of the LSNO electrode. However a simple variation of the LSNO parameter cell could be supported by the shift of all the LSNO (00l) diffraction peaks, and cannot justify the disappearance of most of them. Moreover, in each electron diffraction image, two patterns can be distinguished: the main one related to the LSNO and a second less intense pattern. The plane distances of the second pattern can be safely attributed to the NiO phase, which showed to possess the [100]NiO//[110]LSNO structural relation. Thus, the LSNO modification is not due to interaction with titanium, while it is likely due to a structural change. Some studies on the stability of the LSNO ceramic[34,35] show that the main causes of the LSNO instability are temperature higher than 700°C and high oxygen partial pressure.

In this context, it should be noted that the deposition of complex perovskite oxide by MOCVD always requires the use of high deposition temperature and high oxygen partial pressures. Finally, electrical measurement on deposited films showed a partially conducting behaviour, probably because of the large degradation of the LSNO electrode, while indirect measurements carried out on films deposited using the same MOCVD experimental conditions on the bare LAO substrate showed good dielectrical properties.[36]

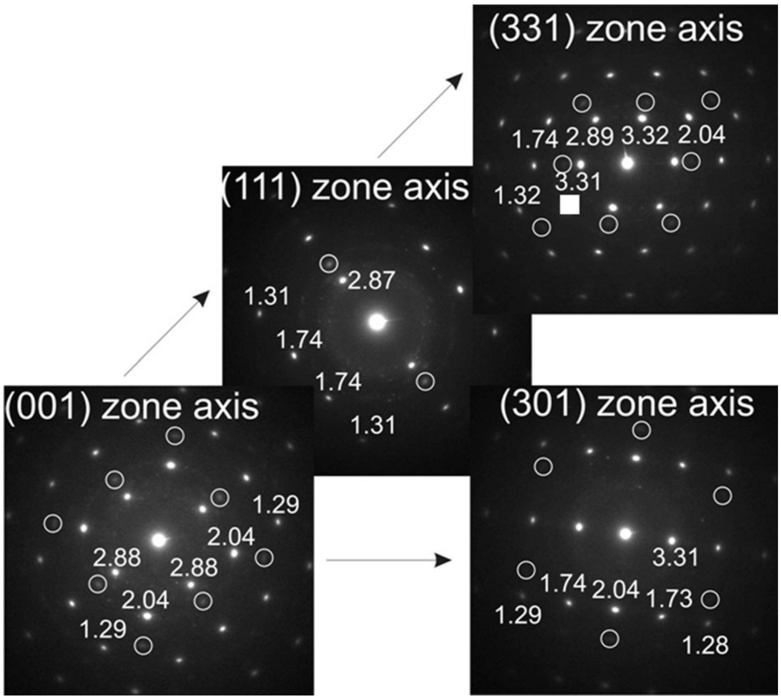

Fig. 2.2.6 SAED patterns from LSNO electrode after the MOCVD process.

References

1 Lo Nigro R.; Fiorenza P.; Catalano M. R.; Fisichella G.; Roccaforte F.; Malandrino G. . Surface and Coatings Technology 230(2013) 152-162.

2 M. A. Subramanian; Li, D. Duan, N. Reisner, B. A. Sleight, A.W.J. Solid State 151Chem.(2000), 323.

3 A. P Ramirez; M. A. Subramanian; M. Gradel;, G Blumberg; T Vogt , S. M Shapiro,.Solid State Commun 115(2000) 217.

4 C. C. Homes,T Vogt,S. M.Shapiro, S.Wakimoto, A. P Ramirez,.Science, 293 (2001), 673.

5 S. Chung, I.D. Kim, S.J.L. Kang, Nature Mater. 3 (2004) 774.

6 L. He, J.B. Neaton, D. Wanderbilt, M.H. Cohen, Phys. Rev., B 67 (2003) 012103.

7 C.C. Homes, T. Vogt, S.M. Shapiro, S. Wakimoto, M.A. Subramanian, A.P. Ramirez, Phys. Rev., B 67 (2003) 092106.

8 T. B. Adams, D. C. Sinclair, A. R. West, Adv. Mater14(2002) 1321

9 T. B. Adams, D. C. Sinclair, A. R. West, Phys. Rev. B 73(2006) 094124.

10M. C. Ferrarelli, D. C. Sinclair, A. R. West, H. A. Dabkowska, A. Dabkowski, G. M. Luke,J. Mater. Chem19 (2009) 5916.

11P. Fiorenza, R. Lo Nigro, C. Bongiorno, V. Raineri, M. C. Ferarrelli, D. C. Sinclair, A. R. West,Appl. Phys. Lett.92 (2008) 182907

12 P. Fiorenza, V. Raineri, M. C. Ferarrelli, D. C. Sinclair, R. Lo Nigro,Nanoscale 3 (2011) 1171

13. J.B He, M.H. Neaton, D. Cohen, , C.C. Vanderbilt,Homes, Phys. Rev. B 65 (2002) 214112

14Felix, A. A.; Rupp, J. L. M.; Varela, J. A.; Orlandi, M. O. J. of Appl. Physi. 112(5), (2012) 054512/1-054512/7.

15A. Deschanvres, B.Raveau, F. Tollemer, Bull.Soc.Chim.Fr., (1967) 4077

16 B. Bochu, M.N. Deschizeaux, J.C. Joubert, A. Collomb, J. Chevanas, M. Marezio, J.Solid State Chem. 29 (1979) 291

17 Y. Lin, Y.B. Chen, T. Garret, S.W. Liu, C.L. Chen, L. Chen, R.P. Bontechev, A. Jacob-son, J.C. Jiang, E.I. Meletis, J. Horwits, H.D. Wu, Appl. Phys. Lett. 81 (2002) 631.

18 W. Si, E.M. Cruz, P.D. Johnson, P.W. Barnes, P. Woodward, A.P. Ramirez, Appl. Phys. Lett. 81 (2002) 2056

19 L. Chen, C.L. Chen, Y. Lin, Y.B. Chen, X.H. Chen, R.P. Bontchev, C.Y. Park, A. Jacobson, Appl. Phys. Lett. 82 (2003) 2317.

---

20 R. Lo Nigro, R. Toro, G. Malandrino, M. Bettinelli, A. Speghini, I.L. Fragalà, Adv.Mater. 16 (2004) 891

21R. Lo Nigro, G. Malandrino, R.G. Toro, M. Losurdo, G. Bruno, I.L. Fragalà, J. Am. Chem. Soc. 127 (2005) 13772

22 R. Lo Nigro, R.G. Toro, G. Malandrino, I.L. Fragalà, M. Losurdo, M.M. Giangregorio, G. Bruno, V. Raineri, P. Fiorenza, J. Phys. Chem. B 110 (2006) 17460

23 P. Fiorenza,R. Lo Nigro,A. Sciuto, P. Delugas, V. Raineri, R. G. Toro, M. R. Catalano,G. Malandrino J. OF APPL. PHYS, 05 (2009) 061634

24 Patrick Fiorenza, Raffaella Lo Nigro, Vito Raineri, Graziella Malandrino, Roberta G. Toro,Maria R. Catalano, J.ofAppl. Phys.108(2010) 074103

25 M.R Catalano; G.Malandrino; R. G Toro,R.LoNigroChem. Vap. Depos (2012), 18(1-23), 76-82

26 Maria R.Catalano, G.Malandrino; C. Bongiorno; R. G Toro,P. Fiorenza, R.Bodeux,; J.Wolfman,; M.Gervai, C. A. Lambert, F.Gervais,; et al Mat. Chem. and Physics 133(2-3) (2012) 1108-1115.

27 G. Malandrino, F. Castelli, I.L. Fragalà, Inorg. Chim. Acta 224 (1994) 203

28 I.S. Chen, J.F. Roeder, T.E. Glassman, T.H. Baum, Chem. Mater. 11 (1999) 209.

29 R. Lo Nigro, R. Toro, G. Malandrino, M. Bettinelli, A.Speghini, I. L. Fragala` , Adv. Mater. 2004, 16, 891.

30 R. Lo Nigro, G. Malandrino, R. G. Toro, M. Losurdo, G. Bruno, I. L. Fragala` , J. Am. Chem. Soc. 2005, 127, 13772.

31 A. A. Levchenko, L. Marchin, Y. Moriya, H. Kawaji, T. Akate,S. Guillemet-Fritsch, B. Durand, A. Navrotsly,J. Mater. Res. 23 (2008) 1522

32 K. T. Jacob, C. Shekhar, X. Li, G. M. Kale, Acta Mater., 56 (2008) 4798

33 S. Shinomori, M. Kawasaki, Y. Tokura, Appl. Phys. Lett. 80 (2002) 574

34 C.F. Kao, C.L. Jeng, Ceramics Intern.26 (2000) 237

35 Y. Ling, W. Ren, X.Q. Wu, L.-Y. Zhang, X. Yao, Thin Solid Films 311 (1997) 128.

36P. Fiorenza, R. Lo Nigro, V. Raineri, R. G. Toro, M. R. Catalano, J. Appl. Phys. 102 (2007) 116103.

Chapter 3: $Pr_{1-x}Ca_xMnO_3$ perovskite thin films

Manganite perovskite materials have been intensively investigated for their several electrical and magnetic properties and, for this reason, they have been proposed as active components in resistive[1] and magnetic data storage [2]as well as in other future technologies.

The manganite materials have a perovskite structure with the general formula $AMnO_3$, but the $RE_{1-x}AE_xMnO_3$complex perovskites, where RE stands for a trivalent rare earth element such as La, Pr, Nd, Sm, Eu, Gd, Ho, Tb, Y etc, and AE for a divalent alkaline earth metal such as Sr, Ca and Ba, are most interesting for their technologically important electrical and magnetic properties.

The perovskite A-site is occupied by RE trivalent ions and AE divalent ions with 12-fold oxygen coordination. The smaller Mn ions in the mixed-valence state Mn^{3+}–Mn^{4+} are located in the B-site at the centre of an oxygen octahedron, with 6-fold coordination.

Based on the tolerance factor, introduced by Goldschimdt, the manganites having $t<1$ possess a distorted structure, rhombohedral ($0.93<t<1$)or orthorhombic structures($t< 0.93$), of lower symmetry than the cubic one.The lattice distortion is due to cation size mismatch and to the MnO_6 octahedron distortion arising from the Jahn–Teller (JT) effect: a distortion of the oxygen octahedron surrounding the B site cation splits the energy levels of a 3d ion such as $Mn,^{3+}$ thus lowering the energy.Another lattice deformation comes from the connecting pattern of the MnO_6octahedra in the perovskite structure, forming a rhombohedral or orthorhombic lattice.[3]

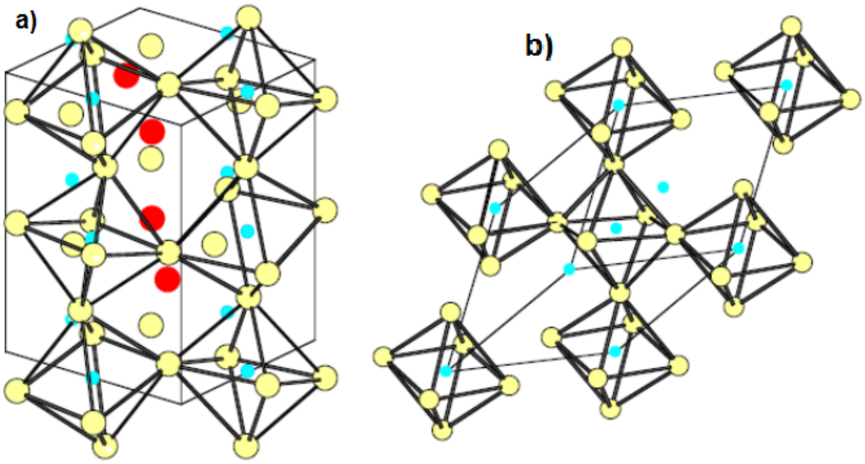

Fig 3.1. Orthorhombic a) and rhombohedral b) structures of manganite perovskites.

The distortion of the MnO_6 octahedra and consequently the structure of manganite is closely relatedto its magnetic and transport properties. The coupling of structure and physical properties of manganites has been widely investigated.[4-6]In addition, in doped manganites all magnetic and electrical properties are associated with mixed valency of the magnetic ion and depend sensitively on the ratio between $Mn^{3+}$and Mn^{4+}ions.

The Mn atom (Z = 25) has an electronic configuration $3d^5 4s^2$, the five degenerate 3d levels, in according to the Hund's rule, are singly occupied with parallel spin electrons. When Mn atom is coordinated in a center of the MnO_6 octahedra, the effect of the octahedral crystal field, due to the p orbitals of the six neighboring oxygens, is to partially lift the orbital degeneracy (Fig. 3.2a) generating a triplet of lower-energy states calledt_{2g} (d_{xy}, d_{xz}, d_{yz}) and a doublet higher-energy states called e_g ($d_{x^2-y^2}$, d_{z^2}), with a separation $\Delta \sim 1.5$ eV.[7]The electronic configurations of Mn^{3+}ion is $3d^4$(Fig.3.2b) and it contains four d electron: three electrons in the t_{2g} level aligned in the same direction and 1 electron in e_g level. This e_g electron plays a key role in conducting and other properties of manganites. The electronic configurations of Mn^{4+} is a $3d^3$(Fig.3.2b) ; the missing of e_g electron create a hole.

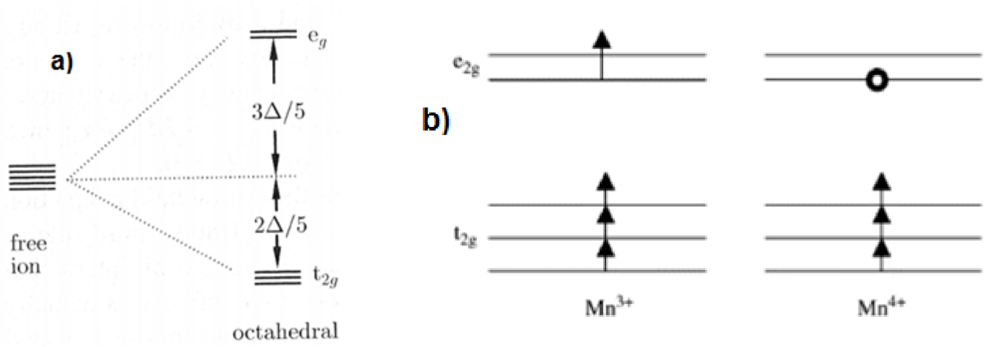

Fig. 3.2 a)Octahedral splitting of d electrons, b)electronic configurations of Mn^{3+} andMn^{4+} ions.

In the case of Mn^{3+}ion electron configuration , the Jahn-Teller (JT) effect leads to a further distortion of the orbitals (Fig.3.3a). The Jahn-Teller (J-T) theorem asserts that in molecules/ ions that have a degenerate ground-state, the molecule/ion will distort to remove the degeneracy and achieve a lower energy state. According to the Jahn-Teller theorem, the $Mn(III)O_6$ groups in the manganite are energetically unstable towards distortions aiming to reduce the total energy of the system, as a consequence of a lifting of degeneracy of the e_g levels. The degree of distortion is determined by the competition between the gain in energy due to the e_g splitting and the increase of the elastic energy associated with the lattice distortion itself. The Mn^{4+} (d^3) ion is JT inactive, because of the absence of an unpaired electron in the e_g orbital.The JT distortion of the octahedra can lead, throughout the crystal, to a distortion of the whole lattice (cooperative JT distortions effect).

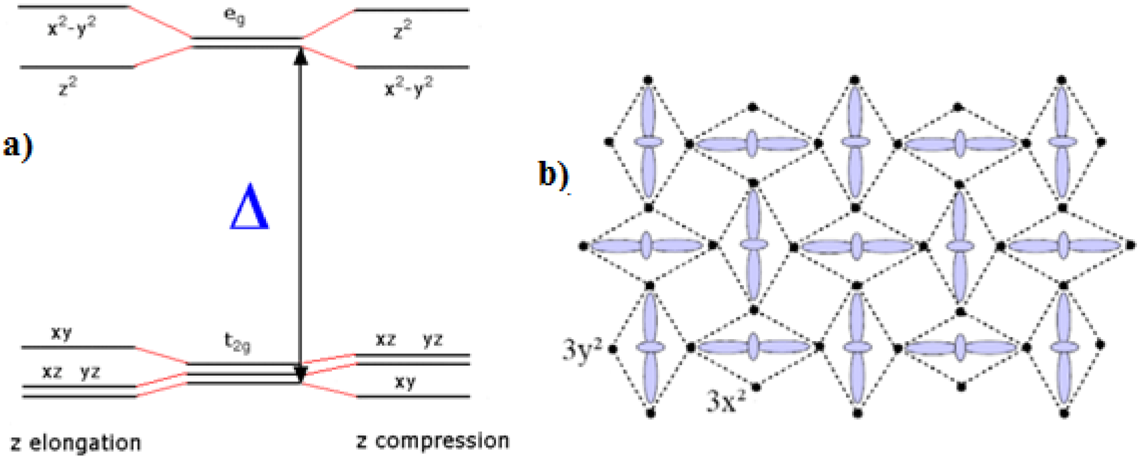

Fig.3.3. a)Distortion of the d orbitals by Jahn-Teller effect, b) cooperative JT distortions effect.

Cooperative JT effect is more evident in the manganite compounds in which the concentration of Mn^{3+} ions is sufficiently high (Fig. 3.3b). In this case a structural phase transition at a certain critical temperature T_{JT} is evident.[8]Jahn-Teller effects in manganites is to localize the e_g electrons on Mn^{3+} sites, and to stabilize insulating phases, either locally or at long range. On the other hand, if Mn^{3+}concentration is low by doping with Mn^{4+} species, the cooperative JT effects is reduced, and no static distortion will be observed, but a dynamic effect which involves rapid hopping of the distortion from site to site.

In addition, the e_g electrons of Mn^{3+}ionsisresponsible for the phenomenon of charge ordering (CO). This consists of a periodic distribution of electric charge in the crystal lattice driven by Coulomb interaction. The mobile e_g electrons may be come localized at certain Mn ion positions in the lattice, forming an ordered sublattice or on the bond centers as well, or, in the most general case, on some intermediate point between those two. Such an intermediate CO state can be more generally seen as a charge-density wave, lacking inversion symmetry and then potentially capable to develop ferroelectric ordering. The CO can be either long-ranged or short-ranged. It is clear that CO is competitive with the electron conductivity, because it tends to inhibit the movement of the charges through the crystal. Compounds with long-range CO are generally insulating, but localized CO (polarons) is responsible for an enhancement of resistivity, introducing scattering centers for the mobile electrons. At the end, the presence of Mn^{3+}/Mn^{4+}ion in the doped manganites lead to the double exchange mechanism, first introduced by Zener in 1951.[9]The e_g electron on a Mn^{3+}ion can hop to a neighboring site(empty e_g neighboring of Mn^{4+}: the double exchange interaction favours hopping if neighboring ions are ferromagnetically aligned, and do not favor hopping if neighboring ions are antiferromagnetically aligned.

Because the ability to hop gives a kinetic energy saving, allowing the hopping process reduces the over all energy. Thus, the ions align ferromagnetically to save energy. Moreover, the ferromagnetic alignment allows the e_g electrons to hop through the crystal and the material becomes metallic.

Very attractive property for future developments , that are closely related to the physical phenomena mentioned above, [10] is the colossal magnetoresistance. [11] The colossal magnetoresistance phenomenon, around the ferromagnetic transition temperature (Tc), consists in the dramatically decrease resistance of a material (negative magnetoresistance) when an external magnetic field is applied. In doped manganites the origin of the CMR is connected with the presence of a metal-insulator transition. The CMR effect is observed in manganites of a narrow range of composition between $x = 0.3$ and 0.4, where is observed the coexistence, in the absence of the magnetic field, of a ferromagnetic insulating phase and an antiferromagnetic insulating phase. In the presence of a magnetic field, these phases transform into a ferromagnetic metallic phase at a Curie temperature Tc. The maximum effect of the CMR appears near the Tc. Recently reported studies propose a new mechanism to explain the CMC effect, based on the idea that the colossal magnetoresistance is due to percolation between nanoscale ferromagnetic metallic (FMM) clusters in an antiferromagnetic insulating (AFI) matrix.[12-14]Among the doped manganite perovskite, $Pr_{0.7}Ca_{0.3}MnO_3$ has been largely investigated not only for its colossal magnetoresistance properties, but also for the recently observed electric pulsed induced resistance (EPIR), [15] interesting properties for potential applications in next-generation nonvolatile resistance random access memories, magneto-resistive read-head, and semiconductor field effect transistors.[16,17]

$Pr_{1-x}Ca_xMnO_3$ is obtained by chemical doping through substitution of Ca^{2+}into Pr^{3+} sites(Fig.3.4a). It has a distorted perovskite-like structure with an orthorhombic P*bnm* symmetry (Fig.3.4b) having lattice parameters at room temperature[18]a=0.5426 nm, b=0.5478 nm, c=7.679 nm.

The crystal structure is characterized by a considerable MnO_6 octaedra distorsion, with a bond angle Mn-O-Mn which deviates from the ideal value of 180°C.

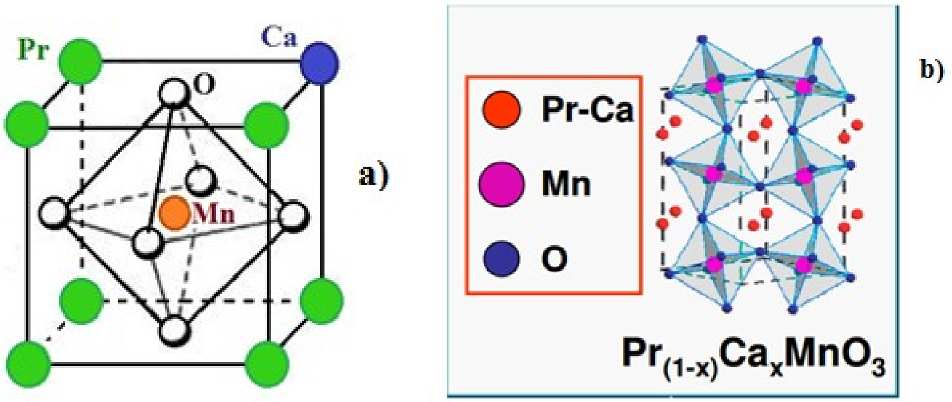

Fig. 3.4.$Pr_{1-x}Ca_xMnO_3$ ideal perovskite a) and distorted orthorhombic b) structures.

A lot of papers report on the phase diagram of the $Pr_{1-x}Ca_xMnO_3$ in function of the Ca^{2+}concentration and temperature(Fig. 3.5).[18- 20] For$0 \leq x \leq 0.1$ it is observed a antiferromagnetic insulating (AFI) phase, stable below 100 K. For $0.15 \leq x \leq 0.3$ a region of ferromagnetic insulating(FI) phase with $T_c \leq 140$ K is observed.For $0.3 \leq x \leq 0.5$, the PCMO has an antiferromagnetic insulating behavior at temperatures below 150 K. Finally, for a wider range of doping, $0.3 \leq x \leq 0.75$at 240 K, PCMO presents a state of charge ordering temperature T_{CO}, due to a Jahn-Teller distortion. At lower temperature (≤ 175 K), d electrons of Mn ions show antiferromagnetic (AF) spin ordering, resulting in an AF insulator. The magnetic state for temperature between the Neel temperature (T_N) and that of charge ordering T_{co} is a paramagnetic state (PI).In the range $0.3 < x < 0.4$, a canted AF insulating (CAFI) state is observed at low temperature, in which small ferromagnetic clusters are embedded in antiferromagnetic matrix.

$Pr_{1-x}Ca_xMnO_3$ is a unique example among manganites, exhibiting insulating behaviour over the entire chemical composition x and over the entire temperature range. This is a consequence of the small ionic radius of Ca, which results in a pronounced orthorhombic distortion that favours charge localization.

The $Pr_{0.7}Ca_{0.3}MnO_3$composition is between two different regions: one where the CO/AF phase is stabilized and the other where a transition from a PI state to a FMI one is observed at around 130 K.

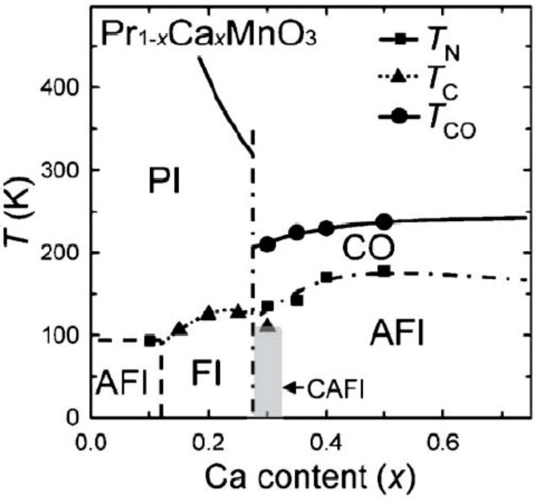

Fig.3.5.: Phase diagram of $Pr_{1-x}Ca_xMnO_3$.

3.1 $Pr_{0.7}Ca_{0.3}MnO_3$ thin films on STO(001) and STO:Nb (001) substrates

3.1.1 Thermal properties of the precursors and MOCVD growth

In this research, the attention has been focused on the synthesis of calcium-doped praseodymium manganite, $Pr_{0.7}Ca_{0.3}MnO_3$, in the form of epitaxial thin films; for many applications, it is desirable to synthesize these materials in the form of nanostructure thick and thin film. A lot of magnetic and electrical properties such as the temperature and field behaviour of the resistivity, the ferromagnetic transition temperature Tc, and the metallic/insulating transition temperature Tp,[21] are closely related to epitaxial strain due to the lattice mismatch between the film and the substrate. At the same time, developing a "user friendly" and low cost route to deposit thin films through an industrially transferable and scalable methodology, is necessary for introducing PCMO materials into electronic and magnetic devices. Metal-organic chemical vapor deposition (MOCVD) has the potential advantage of being a very reliable and reproducible method for the fast production of films with high uniformity degree in both thickness and composition over large areas.[22] In addition, a synthetic approach able to selectively deposit films with a defined stoichiometry is crucial since, as discussed above, the physical properties of PCMO are strictly related to the Ca doping amount.

In the first step of the present approach a screening has been done to find suitable precursors for the growth of PCMO films. Previous MOCVD studies carried out on Pr or Ca containing films have shown that the $Pr(hfa)_3$•diglyme and $Ca(hfa)_2$•tetraglyme [Hhfa=1,1,1,5,5,5-hexafluoro-2,4-pentanedione; diglyme = bis(2-methoxyethyl)ether, tetraglyme= 2,5,8,11,14-

pentaoxapentadecane] are suitable Pr and Ca precursors to grow high quality films.

In regard to the Mn precursor, a novel Mn precursor has been synthesized and compared to commercial precursors.[23,24]The attention has been devoted to the synthesisof a new "second generation" manganese(II) precursor, the Mn(hfa)$_2$●tmeda [tmeda = N,N,N',N'-tetramethylethylendiamine)].

The solid state crystal structure of Mn(hfa)$_2$●tmeda, determined by mean of X-ray single-crystal diffraction confirmed the FT-IR evidences, i.e. the metal cation is coordinated by the four oxygen atoms of two hfa anion and its coordination sphere is fulfilled by the nitrogen atoms of one tmeda molecule. In this way, no water molecules take part to the manganese coordination (Fig. 3.1.1.1).[25]

The thermal behavior of the Mn(hfa)$_2$•tmeda precursor has been investigated by thermogravimetric (TG) analyses and compared with the commercially available Mn(II) ["Mn(acac)$_2$", acac = acetylacetone] and Mn(III) [Mn(tmhd)$_3$,Htmhd = 2,2,6,6-tetramethyl-3,5-heptandione]precursors. The TG profile recorded at atmospheric pressure in purified nitrogen flow is reported in Fig. 3.1.1.2. The Mn(hfa)$_2$•tmeda adduct is thermally stable and the derivative curve of TG (DTG) consists of a single peak thus indicating that it evaporates quantitatively in the 100-230 °C temperature range, with a 1.5 % residue at 300 °C. A completely different behaviour has been observed for the commercially available Mn(II) precursor, the "Mn(acac)$_2$". This compound shows a TG curve with various steps in the range 120-280 °C and a very high residue (27%) at 350°C. This residue is likely due to Mn_2O_3 phase since a theroretical value of 27.3 % is found with respect to the parent Mn(acac)$_2$•2H$_2$O.

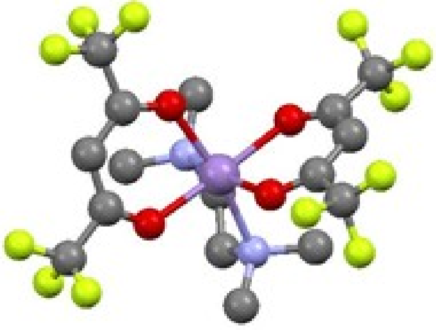

Fig. 3.1.1.1. Ball and stick representation of the compound Mn(hfa)$_2$•tmeda. Hydrogen atoms have been omitted for the sake of clarity

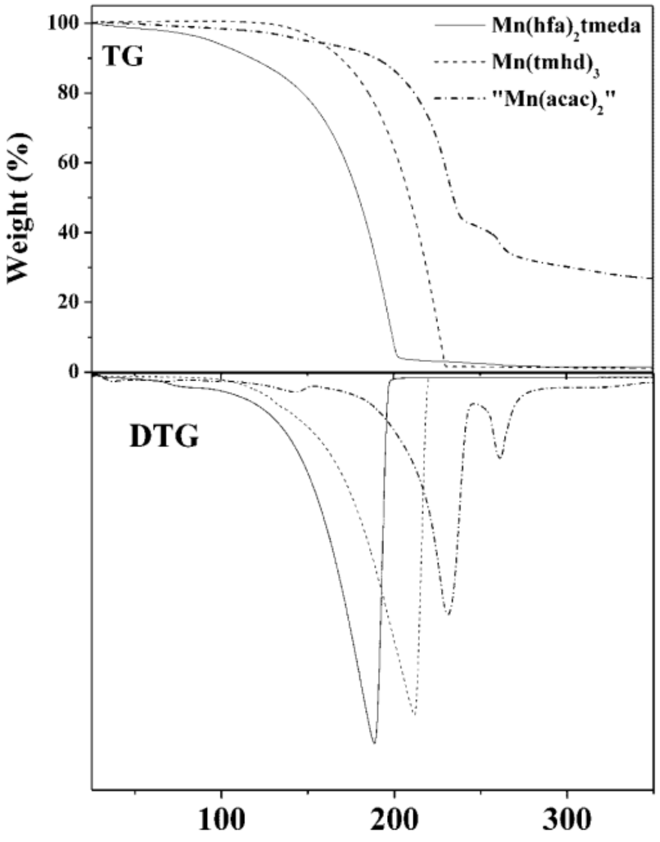

Fig. 3.1.1.2 TG profiles of the Mn (hfa)$_2$•tmeda, Mn (tmhd)$_3$ and "Mn (acac)$_2$" complexes under N_2 flow at atmospheric pressure in the 25-350°C temperature range.

These results are indicative of precursor decomposition likely due to the presence of coordinated H_2O molecules, as confirmed by the FT-IR spectrum and in accordance with single crystal data that report a Mn(acac)$_2$•2H_2O structure,[26] and to the strong donor effect of acac, which stabilizes the Mn(III) oxidation state.Mn(tmhd)$_3$ shows a good thermal stability, but a lower volatility with respect to the Mn(hfa)$_2$•tmeda precursor. In fact, the Mn(tmhd)$_3$ adduct evaporates quantitatively in the 150-260 °C temperature range, with a 2 % residue at 300 °C. It can be concluded that both the Mn(hfa)$_2$•tmeda and Mn(tmhd)$_3$ precursors show clean vaporizations with low residues as requested for MOCVD applications.

A comparison of volatilities of the Pr and Ca precursors with the Mn(hfa)$_2$•tmedaor the Mn(tmhd)$_3$pointed to a betterbehaviour of the Pr:Ca:Mn mixture containing the Mn(tmhd)$_3$ complexes. Therefore, the PCMO depositions have been carried out, on SrTiO$_3$(100),SrTiO$_3$:Nb (100), SrTiO$_3$:Nb (110) and single crystal substrates, using a molten mixture consisting of the Pr(hfa)$_3$•diglyme, Ca(hfa)$_2$•tetraglyme and Mn(tmhd)$_3$precursors.[27][28]

In this context, note that c-axis oriented films of $Pr_{0.7}Ca_{0.3}MnO_3$have been deposited using a very simple, low-cost strategy through an in situ MOCVD process similar to that previously applied for the deposition of $La_{1-x}Sr_xMnO_3$ films.[29,30]

Several experiments have been carried out to assess the operational parameters, such as deposition temperature, flow of reaction gas (water saturated oxygen flow), ratio of the source mixture to produce good crystalline quality PCMO phase film with the desired stoichiometry. In particular the attention has been focused on the effect of substrate orientation on microstructure, morphology and properties of PCMO films.

The study of the thermal properties of the multi-component mixture is a crucial step for a successful MOCVD process. The dynamic and isothermal thermogravimetric (TG) measurement of the Pr:Ca:Mn mixture in the 1.8:0.6:1 ratio has been carried out at atmospheric pressure under purified nitrogen flow. The TG curve (Fig.3.1.1.3a) indicates that the multi-component mixture evaporates quantitatively in the 160-270°Ctemperature range, with a 2% residue left at 350°C, thus indicating that the Pr, Ca, and Mn precursors evaporate simultaneously with a clean process without any-side decomposition. Isothermal thermogravimetric measurements (Fig 3.1.1.3b) in the 120-140°C interval for a total duration of 60 min of the Pr-Ca-Mn mixture point to a mass loss that linearly depends on vaporization time, thus no secondary phenomena occur in this range. Non-linear behaviour is observed at the highest temperature, thus suggesting that contributions of individual precursors prevail, giving rise to differential vaporization rates.

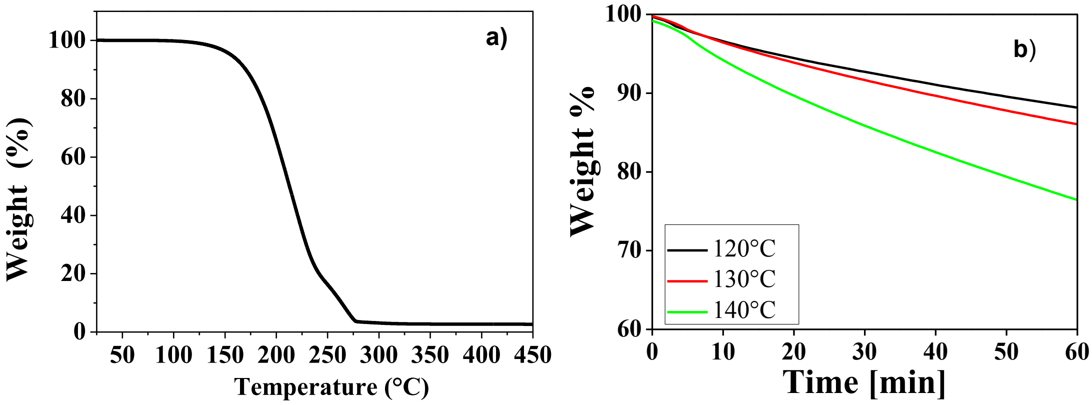

Fig.3.1.1.3 a) TG curve and b)isothermal curves of the multicomponent $Pr(hfa)_3$•diglyme/$Ca(hfa)_2$•tetraglyme/$Mn(tmhd)_3$ mixture.

The DSC curve(Fig 3.1.1.4) of the mixture shows a sharp endothermic peak at 63°C and a very broad endothermic peak from 200 to 250°C, associated, respectively, with melting and vaporization.

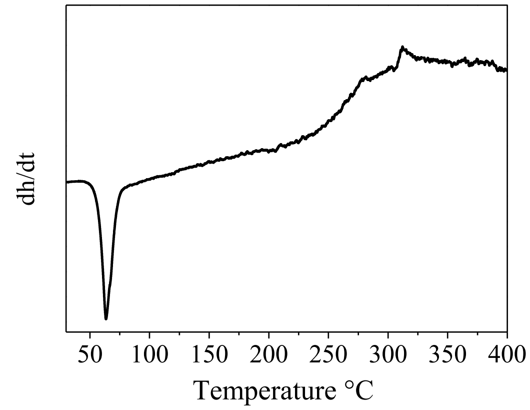

Fig.3.1.1.4DSC curve of the multicomponent Pr(hfa)$_3$•diglyme/Ca(hfa)$_2$•tetraglyme/Mn(tmhd)$_3$ mixture.

It is possible to conclude that the good thermal properties of the mixture observed at atmospheric pressure point to an even better behavior in MOCVD processes under vacuum and demonstrates great advantages for practical applications in depositing PCMO films.

3.1.2Structural and morphological characterization

The STO substrate has a perovskite structure with a unit cell that can be described as pseudo-cubic. The value of the cell parameter a = 3.905Å, is very similar to the lattice parameter of the PCMO (a = 3.855 Å), this translates into a small lattice mismatch between film and substrate that favors the formation of epitaxial films. For this reason, the STO represents the model guide on which the perovskite structure of the PCMO may replicate. The structure of thin films deposited on $SrTiO_3$(STO) (001) has been investigated by Fujimoto et al.[31]

The possibility of six growth modes of $Pr_{0.7}Ca_{0.3}MnO_3$pseudo-cubic (p) perovskite on $SrTiO_3$(001) substrate was discussed.The structural nature of fabricated PCMO on $SrTiO_3$ has been investigated by X-ray diffraction. The XRD patterns(FIG.3.1.2.1, and 3.1.2.2) carried out on film deposited on $SrTiO_3$(100) and on $SrTiO_3$(110) show the formation of the c-oriented PCMO pure phase on both substrates.

In particular, in the pattern, (Fig 3.1.2.1) the peaks at 2θ=23.21° and 47.75° can be safely attributed to 00*l*reflection of the PCMO phase on STO (100), instead the peaks (Fig. 3.1.2.2) at 2θ= 32.87° and 69.50° are due to 101and 202 reflections of the PCMO phase on STO(110).

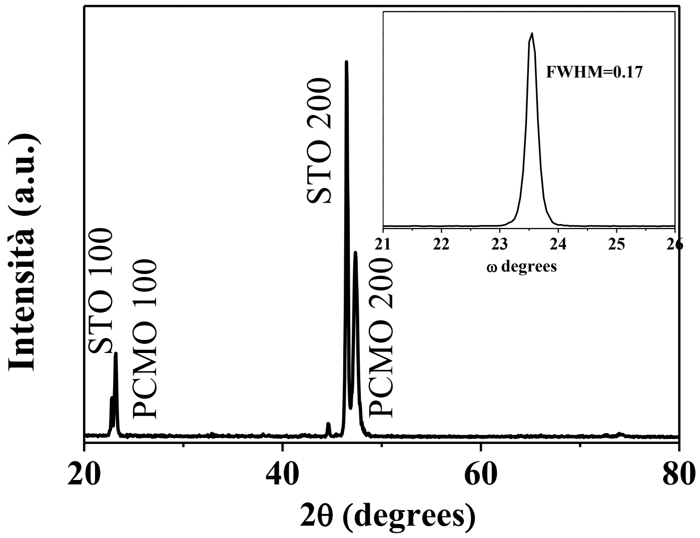

Fig.3.1.2.1 XRD pattern and rocking curve(inset) of a PCMO film deposited on STO (100).

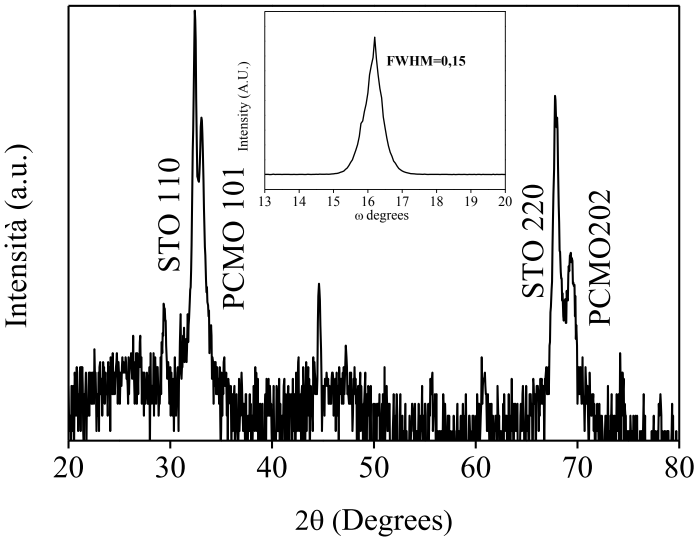

Fig.3.1.2.2 XRD pattern and rocking curve(inset) of a PCMO film deposited on STO (110).

The grains dispersion has been determined throughω-scans (rocking curve), inset in fig.3.1.2.1 and fig.3.1.2.2, of the (001) peak at 47.75°and of the (101) peak at 32.87°.

The full width at half maximum (FWHM) value of 0.17 and 0.15for the PCMO obtained on STO (100) and STO (110),respectively, show an excellent out-of-plane alignment of the PCMO films, indicating an high degree of texturing. Additional information regarding the PCMO film epitaxy have been obtained using TEM. TEM in plan view image (Fig.3.1.2.3a) of PCMO (001) film grown on STO (001) shows the interference fringes due to dislocations formed at the interface PCMO/STO. In Fig 3.1.2.3b the electron diffraction patterns of the

PCMO film and STO substrate are shown. The STO spots (larger and lighter spots) are perfectly coincident with those from the PCMO films, indicating that the deposited films possess epitaxial relationship with the substrate plane. The TEM analysis have been performed on all the deposited PCMO samples and analogous results have been found.

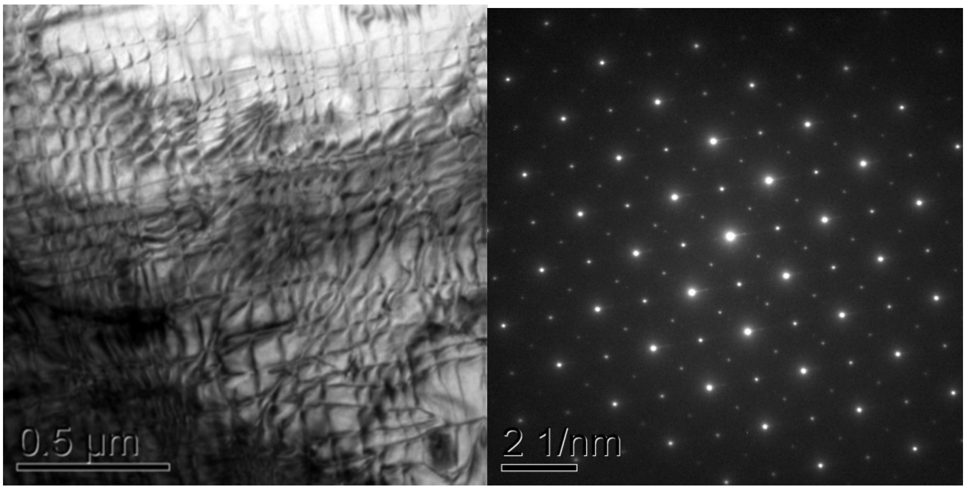

FIG 3.1.2.3 TEM plan view (a) e SAED pattern (b) of the PCMO thin film on SrTiO$_3$ (100).

To establish the chemical composition and the purity of the films, EDX analyses (Fig. 3.1.2.4)have been carried out on films deposited, simultaneously with PCMO thin film on STO (100), on MgO substrate. The Pr L lines are observed at 5.33 keV range, the CaK$_\alpha$ at 3.69 keV, while the MnK$_\alpha$, K$_\beta$ and L peaks are observed at 5.887, 6.496 and 0.637 keV, respectively. The substrate Mg K$_\alpha$ peak is found at 1.4 keV. PCMO films have almost ideal stoichiometry, namely the Pr:Ca:Mn ratio is 1±0.05:0.3±0.05:1±0.05. The correct stoichiometry in the film is obtained for a Pr:Ca:Mn ratio in the source mixture of 1.8:0.6:1.In addition, EDX data rule out the presence of contaminant elements such as C or F.

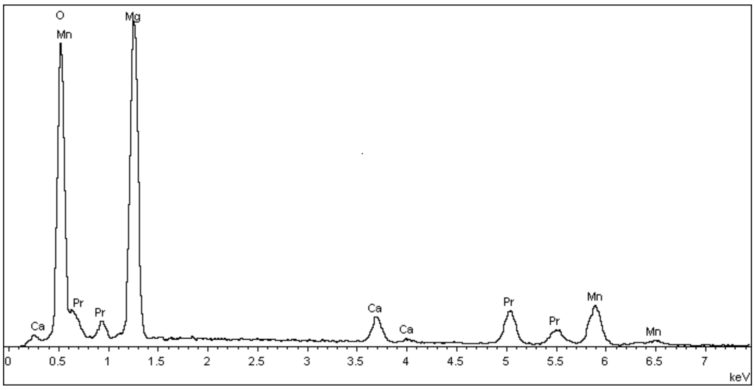

Fig. 3.1.2.4EDX spectrum of a PCMO film deposited on MgO(100).

To confirm the purity and the compositional homogeneity of the deposited phase XPS analysis (Fig 3.1.2.5) has been carried out on the as-deposited sample and after 60 sec. sputtering.XPS Ca2p, O1s, Mn2p and Pr3d spectral regions, acquired after 1 minute of sputtering performed in order to remove "adventicious" carbon and carbonates. The shape and position of Ca, Mn and Pr bands of PCMO were not significantly affected by the fast sputtering. Pr $3d_{5/2}$ band is centered at 933.5 eV pointing to a Pr^{3+} species. It is worthy to note that the shoulders observed for $Pr3d_{5/2}$and $Pr3d_{3/2}$ at lower binding energy (B.E.) are well known satellite bands of Pr^{3+}. The shoulder at higher binding energy observed only for Pr $3d_{3/2}$ is a typical extra structure. Mn $2p_{3/2}$ band is at about 641.5 eV, according to the presence of Mn3+/ 4+ oxidation state. Ca $2p_{3/2}$ band is centered at 347.1 eV according to Ca_{2+} state. Band positions of all observed elements points to the PCMO formation.

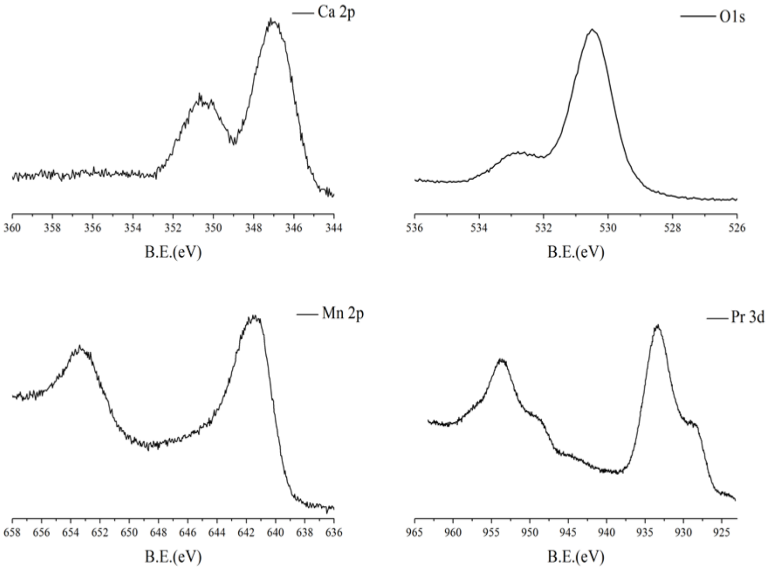

Fig. 3.1.2.5 XPS analysis of PCMO film on STO(100).

In figure 3.1.2.6 is reported XPS depth profile. This measurement indicates an homogeneous composition along depth which points to a $Pr_{0.7}Ca_{0.3}MnO_3$ stoichiometry in agreement with EDX analysis.

The effect of substrate orientation is evident in the morphology of PCMO film (Fig.3.1.2.7). In fact, the FE-SEM images of the films deposited on $SrTiO_3$ (100), $SrTiO_3$:Nb(100) and $SrTiO_3$:Nb(100) show a uniform and homogeneous morphology for all the film.

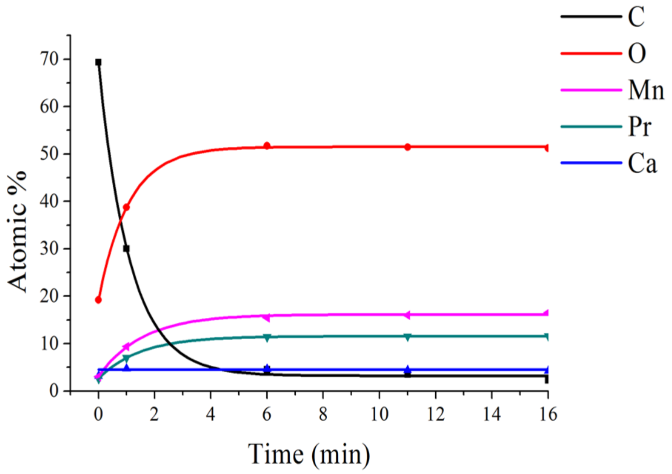

Fig. 3.1.2.6 XPS analysis of PCMO film on STO(100)

The films deposited on STO (100) and STO:Nb (100) show a quite flat and uniform surface with some pinholes. Rectangular shaper grains are found as outgrowth on the STO:Nb(110).

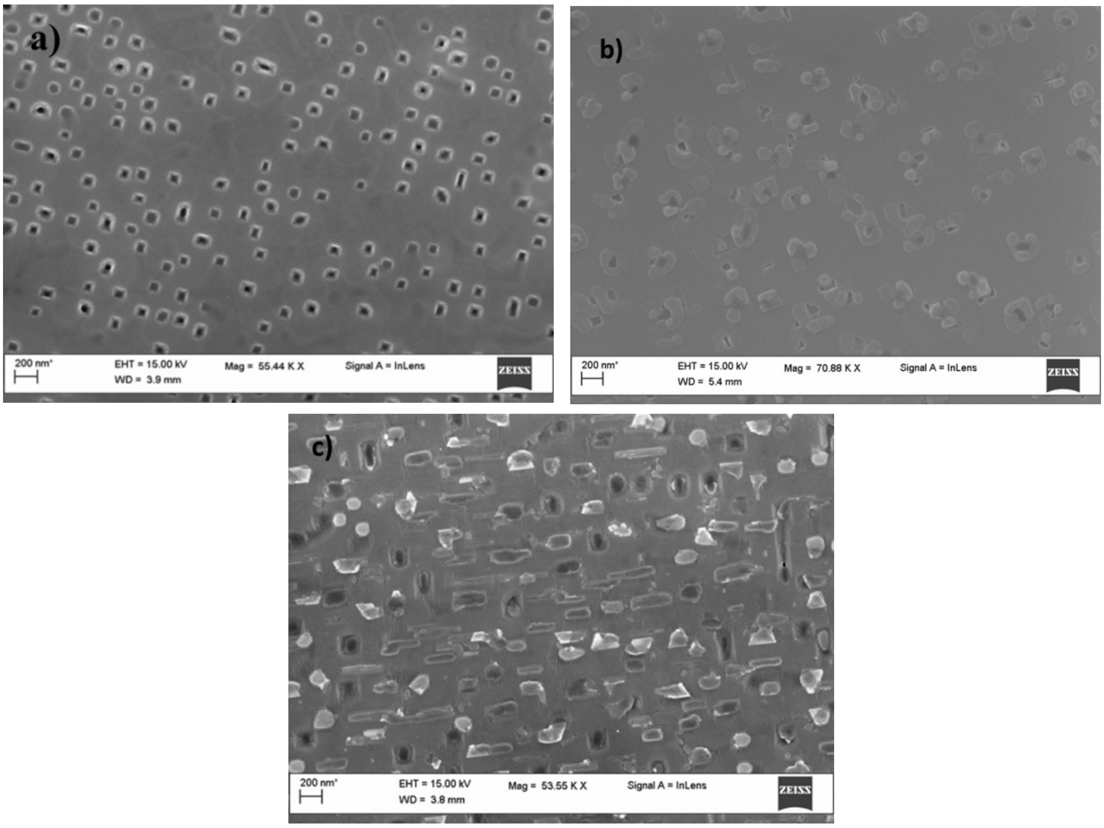

Fig.3.1.2.7 FE-SEM images of PCMO film deposited on a) STO (100);b)STO:Nb(100)and c) STO:Nb(110).

3.1.3 Magnetic characterization of PCMO thin film

Measurements of magnetization obtained in zero-field-cooling and in field-cooling revealed the presence of a FM transition Tc. Values obtained from different samples as function of different magnetic field are shown in the table(3.1.3.1). Values obtained are in agreement with what found in literature.[32,33] Magnetization of sample on STO:Nb (110) are reported in the graph reported in Fig3.1.3.2 together with their derivatives respect to the temperature, from which it is evident the presence of the transition temperature Tc.

Another magnetic transition is present at lower temperature (40 – 50 K ca.) attributable to the contribution of Pr spins.

Magnetic Field (T)	PCMO on STO:Nb(100)	PCMO on STO:Nb(110)	PCMO on STO(100)
0.5	-	105 K	105 K
1.0	115 K	110 K	110 K
3.0	125 K	120 K	139 K
5.0	100 K	135 K	95 K

Table. 3.1.3.1.Magnetic data of PCMO films grown on the different substrates.

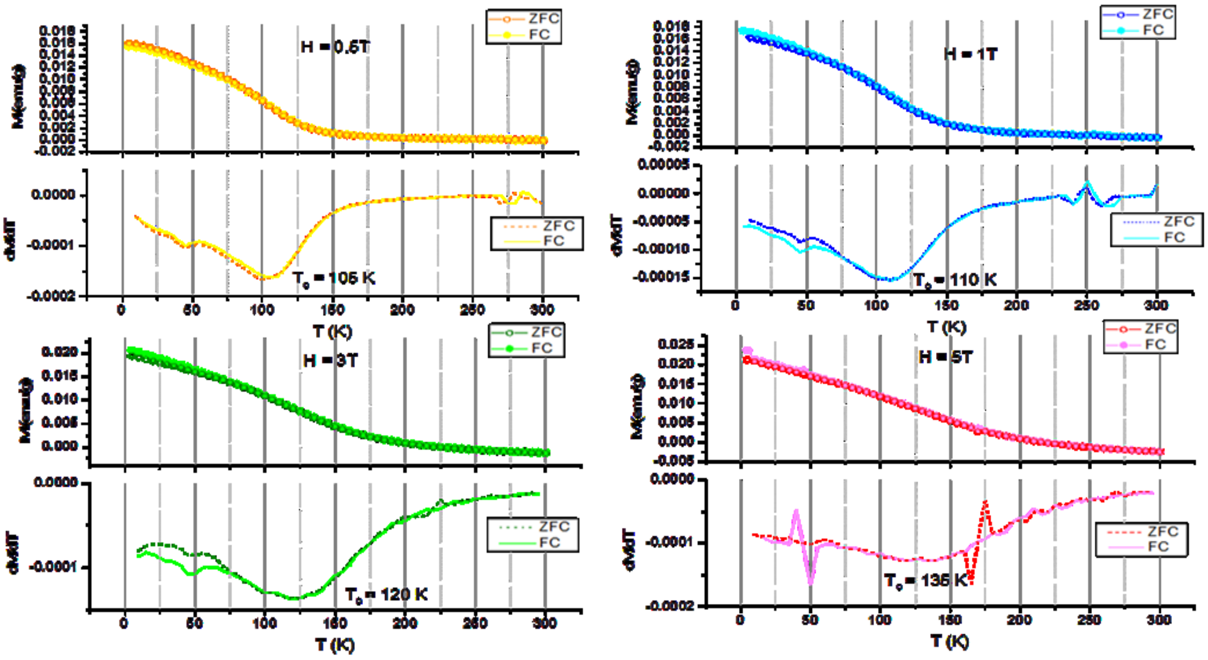

Fig. 3.1.3.2 Magnetization curves of the PCMO sample on STO:Nb (110).

References

---

1 S Q Li, N J Wu, A Ignatiev 76 Appl. Phys. Lett.2 (2000) 749

2Y Murakami, H Kasai, J J Kim, S Mamishin, D Shindo,S Mori, A Tonomura , Nature Nanotechnol. 5 (2010) 37Y.

3Y. Tokura, Rep. Prog. Phys. 69 (2006) 797

4 P. G. Radaelli, M. Marezio, H. Y. Hwang, S.-W. Cehong, B. Batlogg, Phys. Rev. B 54, 8992 (1996

5 L. Wu, R. F. Klie, Y. Zhu, Ch. Jooss, Phys. Rev. B 76, 17(2007)4210

6J. M. D Coey, M Viret,.; v. SMolnár, . Adv. Phys. 58 (2009) 571−697

7 A. M. Haghiri-Gosnet, J. P. Renard, J. Phys. D: Appl. Phys. 36 (2003)R127

8 T. Chatterji, B. Ouladdiaf, P. Mandal, B. Bandyopadhyay, B.Ghosh, Phys.Rev. B 66, (2002)054403

9 C. Zener, Phys. Rev. 82(1951), 403

10 Zhao, G., Conder , K., Keller, H., and Mu ï ller , K. A., Nature, (1996), 381, 676

11 Jin, S., T iefel, T. H., M c Cormack, M., F astnacht, R. A., R amesh, R., and Chen, L. H., , Science, 264,(1994) 413

12 M. Uehara, S. Mori, C.H. Chen, S.W. Cheong, Nature 399(1999) 560

13 A. Moreo, M. Mayer, A. Feiguin, S. Yunoki, E. Dagotto, Phys. Rev. Lett. 84(2000). 5568

14 D. Saurel, A. Brûlet, A. Heinemann, C. Martin, S. Mercone, C. Simon,Phys. Rev. B 73, (2006).094438

15 X. Chen, N. J. Wu, J. Strozier, aA. Ignatiev, Appl. Phys. Lett.87,(2005) 233506

16 R. Waser, M. Aono, Nanoionics-based resistive switching memo-ries. Nat. Mater.6(11),(2007) 833–840

17 A. Sawa, Resistive switching in transition metal oxides. Mater. Today11(6) (2008)28–36

18 Z. Jirak, S.Krupicka, Z. Simsa, M. Dlouha, S.Vratislav. Magn.Magn. Mater. (1985), 53.

19 T. Tonogai, T. Satoh, K. Miyano, Y. Tomioka, Y. Tokura. Phys. Rev. B. 62 (2000), 13903.

20J.P.Hill, C.S. Nelson, M.V. Zimmermann, Y.J. Kim, DoonGibbs, D.Casa, B. Keimer, Y. Murakami, C. Venkataraman, T.Gog, Y. Tomioka, Y. Tokura, V. Kiryukhin, T.Y. Koo, S. W. Cheong. Appll.Phys. A. 73, (2002) 723.

21 L. Huang, B. Qu, L. Liu, and L. Zhang, Solid State Comm., 143(2007) 382.

22 M. L. Hitchman, and K. F. Jensen; Chemical Vapor Deposition: Principles and Applications Eds: Academic Press, London, 1993.

---

23 Z. Lipani.; M. R. Catalano; P. Rossi.; P. Paoli; G. Malandrino. Chem.Vap. Deposit 19(1-2-3) (2013) 22-28.

24 M. R Catalano, G. Malandrino. PhysicsProcedia 46, (2013), 118-126. |

25 G. Malandrino; R. G Toro.; M. R Catalano.; M. E Fragala.; P. Rossi; P. Paoli. Europ. J. of Inorg.Chem.7 , (2012), 1021-1024.

26 H. Montgomery, E. C. Lingafelter, ActaCrystallogr. Sect. B: StructuralCrystallography and CrystalChemistry1968, 24, 1127-8; (b) S. Onuma, S. Shibata, Bull. Chem. Soc. Japan43(1970) 2395-7.

27.M. R. Catalano, E. Schilirò, G. Cucinotta, M. Mannini, A. Caneschi, E. Smecca, G. G. Condorelli, G. Malandrino. IX INSTM CONFERENCE Bari., 30th June - 3rd July 2013.

28 M. R. Catalano, E. Schilirò , G. Cucinotta , M. Mannini , A. Caneschi , R. Lo Nigro , E. Smecca , G. G. Condorelli , G. Malandrino[a]MOCVD synthesis of heteroepitaxial Pr$_{0.7}$ Ca$_{0.3}$ MnO$_3$ films: effects of processing conditions on structural/morphological and functional properties. Manuscript in preparation.

29 R. G. Toro, G. Malandrino, L. M. S. Perdicaro, D. M. R. Fiorito, A. Andreone, G. Lamura, I. L. Fragalà, Chem. Vap. Deposition15 (2010) 143

30 R. G. Toro, D. M. R. Fiorito, M. E. Fragalà, A. Barbucci, M. P. Carpanese, G. Malandrino, Mat. Chem. Phys. 124, (2010) 1015

31 M. Fujimoto, H. Koyama, Y. Nishi, T. Suzuki, S. Kobayashi, Y. Tamai, N. Awaya, J. Am. Ceram. Soc. 90 (2007)2205

32 M. R. Lees, J. Barratt, G. Balakrishnan, D. McK. Paul, C. D. Dewhurst J. Phys. Condens. Matter 8 (1996) 2967

33 W. Westhauser, S. Schramm, J.Hoffmann, C. Jooss, Eur. Phys. J. B 53(2006) 323

Chapter 4: Ionic conductor perovskite oxides

Ionic conduction is the movement of an ion from one site to another through defects in the crystal lattice of a solid. In an ideal crystal all constituent ions are arranged in a regular periodic fashion and are often stacked in a close-packed form, while defects in an ionic solid allow the migration of ions in an electric field. Two types of defects in the crystals important for ion mobility are 'Schottky' and 'Frenkel' defects. These belong to the class of 'point defects' in crystals. Schottky defects refer to the crystal imperfection in which one cation and one anion leave its position creating a vacancy pair. A single ion missing from its regular position and wandering in interstitial sites results in Frenkel defect. The Frenkel and Schottky defects result in vacant sites in the crystal and any ion in the immediate vicinity can jump to one of the vacant sites, leaving vacant their own site which could now host another ion. This process can lead to transport of ions across the solid giving rise to conductivity. This mechanism is termed vacancy migration (Fig.4.1a). The ion that moves to the interstitial site, giving rise to a Frenkel defect, can subsequently hop into adjacent interstitial site and so on, resulting in long distance motion of the ion. This mechanism is referred to as interstitial migration (Fig.4.1b).

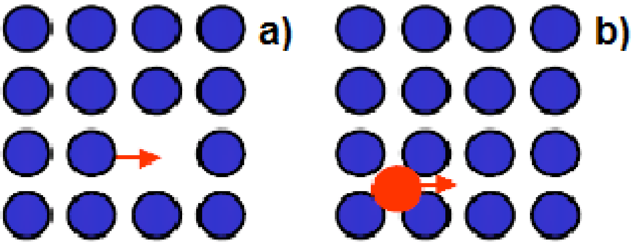

Fig 4.1 a) Vacancy migration and b) interstitial migration.

Another mechanism called interstitialcy mechanism refers to the conduction mechanism through cooperative movement of two or more ions. In this case the occupancies of the sites as well as the interstitials are such that for an ion to jump to a neighboring site or interstitial requires one or more neighboring ions to be pushed elsewhere.

The density of defects in a crystal depends considerably on various factors like, the structure, the temperature, the presence of impurity ions, the nature of chemical bonding between constituent ions etc. Solid state ionic conductors are important from an industrial viewpoint and they can be used in various technological application, such as electrolytes in fuel cells.

In fact, in recent years, the Solid Oxide Fuel Cells (SOFCs)[1] have attracted great interest because convert chemical energy directly to electrical energy cleanly and efficiently and are considered a good alternative to dirty and wasteful combustion. The advantages of SOFCs over traditional power generation systems are numerous.[2-4] One of the most important advantages of SOFCs is that they are flexible in the choice of fuel, as they can use many common hydrocarbon fuels such as natural gas, diesel, gasoline and alcohol without the need to reform the fuel into pure hydrogen. The greenhouse gas emissions from SOFCs are very low, as SOFCs have extremely low emissions by eliminating the danger of carbon monoxide in exhaust gases, because any CO produced is converted to CO_2 at the high operating temperature. Finally, the high operating temperature, at which SOFCs normally operate, allows the reforming of hydrocarbon directly inside the anode, without the need of using noble metal-based catalysts, that are problematic for their prohibitive cost and may compromise long term stability of devices. A SOFC is an assembly of different ceramic materials and typically consists of an electrolyte, a cathode, an anode, and an interconnect. Perovskite-type materials have been widely studied as components in SOFCs because they are characterized by a discrete oxide ion transport.

In this work two different types of conductors with perovskite structure have been obtained by MOCVD in form of thin film for potential applications in micro-SOFCs: the lanthanum cobaltite ($LaCoO_3$), base structure of an ionic-electronic conductor, and the proton conductor $BaCeO_3$.

4.1 Perovskite $LaCoO_3$ thin films on single crystal substrates.

4.1.1. Thermal properties of the precursor and MOCVD growth

Cobalt-based perovskite oxides have a large variety of magnetic, ferroelastic and electrical properties, and are promising candidates as ionic conductors and surface catalysts.[5-7] Lanthanum cobaltites, $LaCoO_3$ (LCO) have been tested as catalyst in various processes such as for carbon monoxide combustion[8] and for volatile organic compounds combustion.[9] In addition, lanthanum cobaltite has attracted considerable interest as cathodes of solid oxide fuel cells (SOFCs) [10,11], due to its ionic-electronic conduction, i.e. they can conduct electrons as well as ions. Furthermore LCO in form of thin film shows intriguing ferromagnetic behavior, whereas LCO in bulk form is a nonmagnetic material.[12] This behavior has been reported to be due to the highly strained nature of deposited films which is responsible for the distortion of the cobalt oxygen octahedra.[13]

In this contest, thin films of lanthanum cobaltite have been grown using a simple in-situ MOCVD process on rock-salt like MgO (001) and perovskite $LaAlO_3$ (001) substrates.[14] The key-point of this process relies upon the application of a molten precursor mixture, consisting of the $La(hfa)_3$•diglyme and $Co(tta)_2$•tmeda (H-hfa = 1,1,1,5,5,5-hexafluoro-2,4-pentanedione; diglyme=$CH_3O(CH_2CH_2O)_2CH_3$, Htta=α-thenoyltrifluoroacetone; tmeda = N,N,N′,N′-tetramethylethylendiamine). The thermal properties of the La-Co mixture have been tested by dynamic and isothermal thermogravimetric analyses at atmospheric pressure under purified nitrogen flow. The La $(hfa)_3$•diglyme/$Co(tta)_2$•tmeda mixture evaporates in a single step in a narrow temperature range (140–230 °C) with a low residue (≈9%) left at 400 °C (Fig. 4.1.1.1a), Isothermal thermogravimetric curves (Fig. 4.1.1.1b) recorded under atmospheric pressure in N_2 atmosphere for 60 minutes in range temperatures varied from 130 to 150 °C, show a linear behaviour at 130° and 140 °C, thus pointing to a constant vaporization rate during the experimental time, with negligible deviations only for the 150 °C plot. The termogravimetric analysis show that the La $(hfa)_3$•diglyme/$Co(tta)_2$•tmeda mixture possesses good thermal stability, and demonstrates great advantages for practical applications in depositing La-Co containing films in MOCVD processes under vacuum.

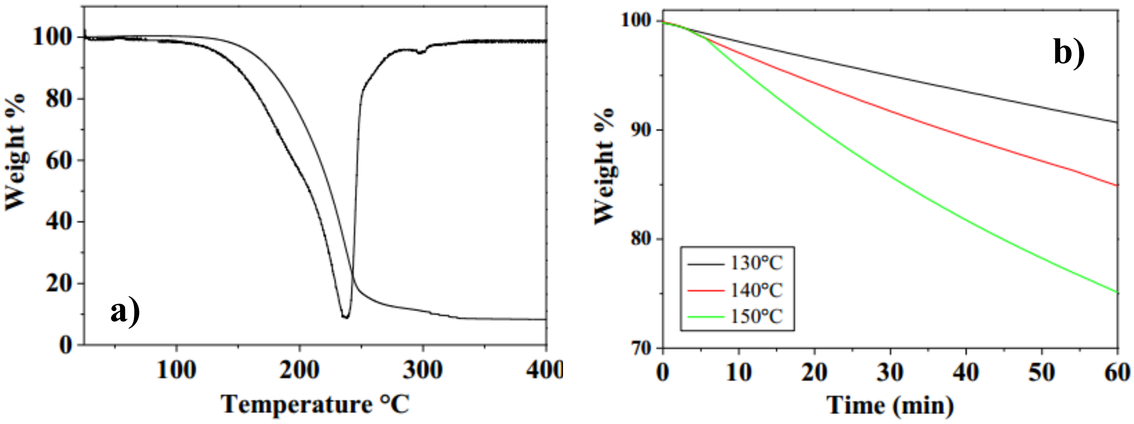

Fig. 4.1.1.1 a) Dynamic thermogravimetric curve and b) isothermal curves of the $La(hfa)_3$•diglyme/$Co(tta)_2$•tmeda mixture.

Additional information on the thermal properties of the molten mixture was obtained by differential scanning calorimetry measurement (Fig.4.1.1.2). Single precursor curves show sharp endothermic peaks at 78.2 °C, and 138.31 °C, associated with melting of

La(hfa)$_3$•diglyme and Co(tta)$_2$•tmeda, respectively, while the peaks at 200°–253 °C and 270°–312 °C are associated with vaporizations of the individual precursors. The multi-component source curve shows an endothermic peak at 69 °C, associated with melting of the La(hfa)$_3$•diglyme component, and a broad peak at 207°–304 °C, that represents the vaporization of the mixture. The lower melting temperature observed for the lanthanum precursor in the mixture may be related to the presence of the Co precursor that acts as an impurity and has two effects: melting point depression and melting range broadening. In addition, the endothermic peak expected for melting of the Co (tta)$_2$•tmeda, is missing in the DSC curve of the mixture, thus the La(hfa)$_3$•diglyme precursor is likely to act, on melting, as a solvent for the Co source.

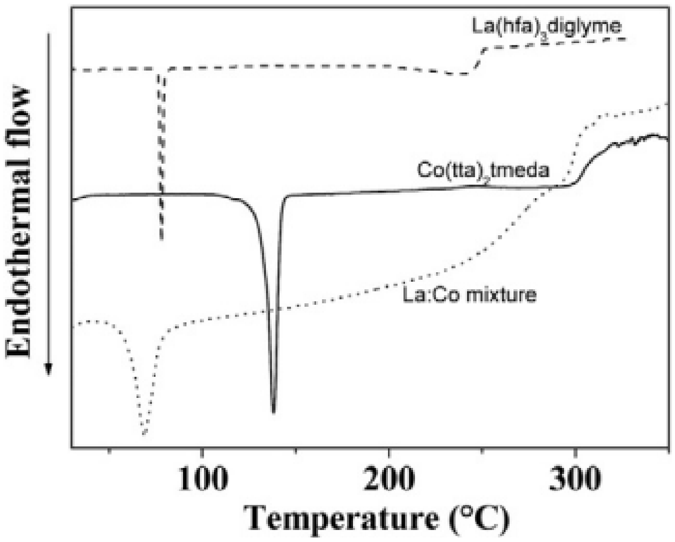

Fig.4.1.1.2 DSC curves of the single La (hfa)$_3$•diglyme and Co(tta)$_2$•tmeda precursors, and the multicomponent La(hfa)$_3$•diglyme/Co(tta)$_2$•tmeda mixture.

Various experiments have been carried out to assess the operational parameters, such as deposition temperature, flow of reaction gas (water saturated oxygen flow), La:Co ratio of the source mixture to produce good crystalline quality LCO phase film with the 1:1 desired stoichiometry. A systematic study has been carried out in order to investigate the influence of the deposition temperature on the formation of LCO films on MgO and hence to establish the lowest temperature suited for the formation of the LCO phase. On the basis of our previous studies on deposition of perovskite phases[15-18]films have been deposited in the 600–900 ° temperature range on MgO (001) substrates, using a water vapor saturated oxygen flow as reactant gas and an argon flow as carrier gas.

4.1.2 Structural, compositional and morphological characterization

LCO is a perovskite-type oxide with a slight distorted structure with respect to the ideal cubic perovskite. The tolerance factor (t), introduced by Goldschimdt, has been calculated (see Chapter 1) to determine the "stability" of the LCO perovskite structure; a t value, taking into account the crystal ionic radii from Shannon,[19] of 0.88 has been found. The value of the tolerance factor indicates that LaCoO3 is slightly distorted with respect to the ideal cubic symmetry, having a rhombohedral structure with a_{rh} = 35.3781 Å and β= 60.81°. Nevertheless, the system may be indexed as a pseudo-cubic (pc) with an a-axis parameter a_{pc}= 3.8029 Å.[20] LCO films have been deposited on $LaAlO_3$ (001) that has a perovskite structure, whose unit cell can be described as pseudo-cubic with a lattice constant a = 3.792 Å. The lattice parameter of the LAO substrate is only 0.13 Å smaller than a_{pc} for LCO with a mismatch of 0.3% and, therefore, it represents a suited substrate for the film growth, while the MgO substrate, that has a larger a-axis parameter of 4.213 Å with a mismatch of 9.7%, has been used to determine the film composition through EDX avoiding the contribution of La deriving from the LAO substrate. The Energy Dispersive X-ray (EDX) analyses show the La peaks in the range of 4.25–5 keV, while the Co K_α and K_β peaks are observed at 6.9 and 7.8 keV; the peak at 0.7–0.8 keV range is due to La M_α and Co L_α lines. In addition, the windowless EDX detector allowed to detect the O K_α peak at 0.520 keV. To determine the correct stoichiometry of the LCO films, several experiments at 900 °C have been carried out, changing the ratio of the two precursors in the mixture (table 4.1.2.1). EDX spectra indicate that he correct stoichiometry (1.00 ± 0.05:0.96 ± 0.04) in the film is obtained for a La:Co ratio in the source mixture of 1.0:0.5. Therefore, the 1.0:0.5 stoichiometry of the source mixture has been used throughout all the reported experiments.

CAMPIONI	Co:La miscela	Co:La film
LCO_1	0.5:1.3	1:1.7
LCO_2	0.5:0.8	1:0.45
LCO_3	0.5:1	1:0.9

Table 4.1.2.1 Dependence of the film La:Co ratio on the source mixture composition (900°C).

The structural characterization of the film deposited in the range temperature of 600-900°C has been obtained by X-ray diffraction measurements (Fig. 4.1.2.2). The XRD patterns indicate that the formation of the LCO phase depends upon the deposition temperature with a strict border line around 650 °C. In fact, the pattern of films deposited at 600 °C shows impurity peaks at 31.00° and 45.25°.

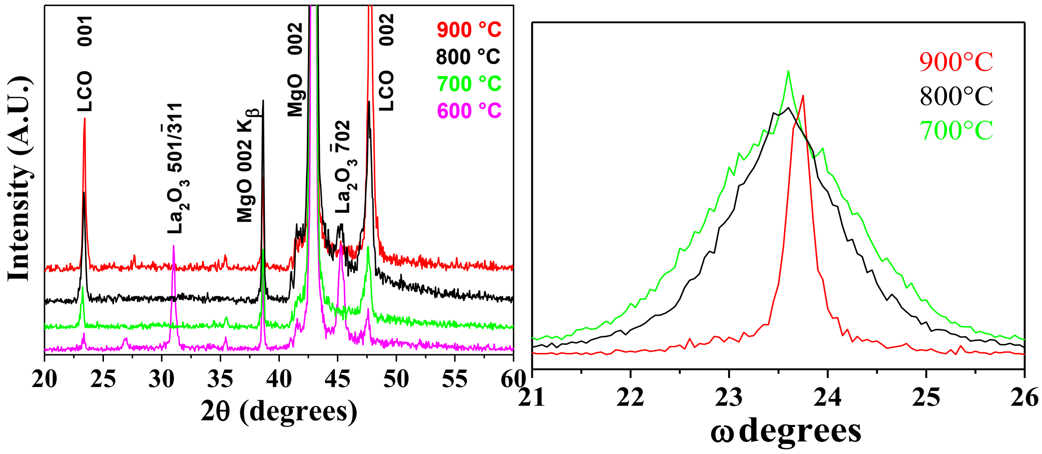

Fig.4.1.2.2 a) XRD patterns of the films obtained on MgO (100) in the 600-900°C temperature range. b) Rocking curves of the peak at 47.60° of the films obtained at 700°-800°-900°C.

Assignment of these peaks is not univocal, since they may be associated either with the−501/−311 and−702 reflections, respectively, of the La_2O_3 phase or with the 104 and 110 reflections, respectively, of the LaOF phase. Actually, in these operative conditions, water saturated O_2 flow as reaction gas, the formation of fluoride phase should not occur, since it is well known that the use of water saturated O_2 flow is able to hydrolyze fluorine containing phases and to avoid fluorine contamination .[21]

Temperatures higher than 650°C and the use of water vapor saturated oxygen flow favor the formation of good crystalline quality $LaCoO_3$ films. In fact the XRD patterns (fig.4.1.2.2a) of the films deposited on MgO (001) in the 700-900°C show the formation of pure LCO films with sharp peaks at $2\theta \approx 22.8°$ and $2\theta \approx 47.6°$ associated with the LCO 001 and 002 reflections, respectively, and a peak at 42.95° related to the 002 reflection of the MgO substrate. The presence of only the (00ℓ) peaks associated with the $LaCoO_3$ phase, points to the formation of “c-axis” oriented films. A deeper analysis of the position of the 002 peak indicates that it slightly shifts to higher angles going from 47.60° (700°C) to 47.75° (900°C). Considering the position of the MgO as a peak reference, the out-of-plane cell parameter has been estimated to be a_{ps}= 3.8178 Å and 3.8063 Å, respectively at 700 and 900°C. This finding indicates that higher temperatures favour the formation of better quality $LaCoO_3$ films as indicated from the a-axis parameter which compares very well with the reported 3.8029 Å value. The film out-of-plane orientation has been confirmed by recording the rocking curves of the peak around 47.60° (Fig.4.1.2.2 b). The orientation degree increases on increasing the deposition temperature as shown from the full width at half maximum (FWHM) of the rocking curves. Thus, the FWHM of rocking curves of films deposited at 700 °C and 800°C are 1.45° and 1.25°, respectively. The FWHM value of 0.30° of the film deposited at 900°C confirms the low mosaicity of the $LaCoO_3$ thin film deposited at this temperature.

To establish the nature of the lanthanum impurity phase observed in the sample deposited at 600 °C and to further ascertain the sample purity, XPS analysis (fig.4.1.2.3) has been carried out on the as-deposited sample and after 60 s sputtering. Fig. 4.1.2.3 shows the Al K_α survey XPS of the as-deposited (600 °C) $LaCoO_3$ film. The as-deposited film shows a composition with a slight lanthanum excess and a 2.6 % fluorine contamination. After 60 s sputtering no fluorine signal (at about 685–687 eV) can be detected, thus demonstrating that the fluorine contaminant was involved only in the topmost layers of the film. Also the C 1 s signal (285.0 eV) is almost negligible. Analogously to already reported data on similar systems, the La 3d level is characterized by a double peak for each spin–orbit component, attributed either to energy loss phenomena ("shake-up" satellites) induced by intense O 2p–La 4f charge events or to the existence of a mixing of electronic configurations.[22] In particular, peaks at 833.5 and 850.5 eV are consistent with the 3d spin-orbit components of some La_2O_3.[23] Peaks at 837.8 and 854.7 eV account for the La 3d spin-orbit components typical of $LaCoO_3$ materials .[24]

The Co 2p features consist of the broad $2p_{3/2}$, $2p_{1/2}$ spin-orbit components at 776.5 and 792.0 eV, respectively. These values are lower than those typically reported for cobalt oxides.[25] In addition, the absence of any shake-up peaks in the spectra indicated that the Co ions were only forming a $LaCoO_3$ phase. Ultimately, by XPS analysis, it is possible to conclude that the XRD impurity peaks may be associated with the La_2O_3 phase, since no F is present in the film within the detection limit of XPS except on the topmost layers.

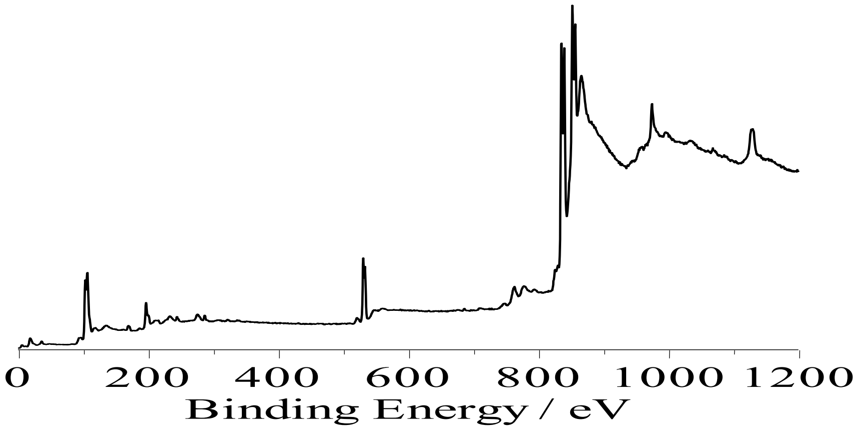

Fig.4.1.2.3 XPS analysis of the as-deposited LCO sample at 600°C and after 60 s.

The homogeneity of the film surfaces has been confirmed by FE-SEM investigations (fig.4.1.2.4). Films deposited at the lowest temperature present a different morphology from those observed at higher temperatures. In fact, at 600°C, films consist of rounded grains having diameters of about 200 nm coalesced in a uniform homogeneous structure. At higher temperatures, dense homogeneous structures are observed with plate-like grains in the order of 200 nm. At 900°C plate-like squared grains between 100 and 200 nm in dimensions are found.

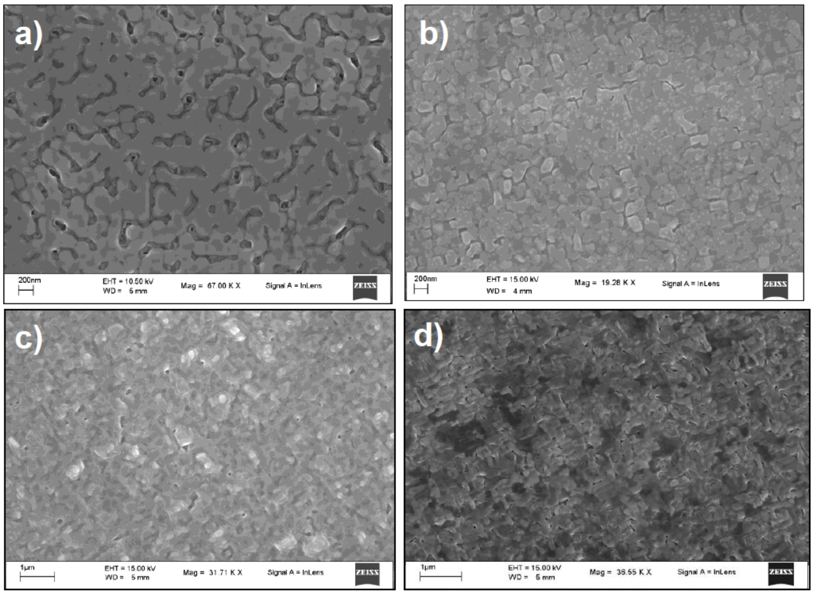

Fig.4.1.2.4 FE-SEM images of the film obtained on MgO (100) in the 600-900°C temperature range.

The LCO films have been also deposited on $LaAlO_3$perovskite substrate that, as previously commented, has a very similar a-axis parameters that makes it difficult to distinguish between the 00ℓ reflections of $LaCoO_3$ and $LaAlO_3$ phases. In fig 4.1.2.5 is reported a diffraction patterns associated with the sample deposited at 900°C, and a close up of the peak at $2\Theta\approx48°$ is reported in the Fig. 4.1.2.5b. In the enlarged XRD Θ-2Θ feature around the 002 reflection, the shoulder at 47.6° may be associated with the $LaCoO_3$ 002 reflection, while the very intense peak around 48° is due to the $LaAlO_3$ (002) peak. This peak is clearly made up of at least two sub peaks separated by $\Theta=0.11°$. This can be attributed to minor imperfections due to twinning of the $LaAlO_3$ crystal along the [010] tilt axis, a frequently observed feature of $LaAlO_3$ single crystal substrates used for thin film deposition. In Fig 4.1.2.6 the FE-SEM plan view and the cross-sectional images of a sample deposited at 900°C on $LaAlO_3$ are reported. The surface is uniform and flat with well-distinct square grains of about 150 nm; the thickness is about 360 nm, with an average growth rate of 6 nm/min. At the temperature of 700 °C the growth rate is around 3 nm/min. These data indicate that the growth is likely to occur under the mass transport limited regime, but further experiments are needed to complete the study with an Arrhenius plot.

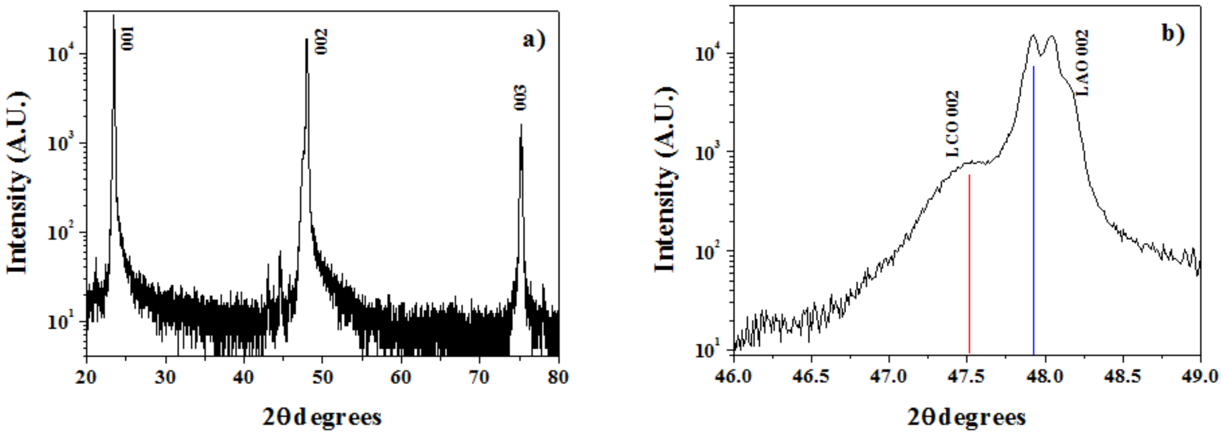

Fig.4.1.2.5 a) XRD pattern of a LCO film deposited on $LaAlO_3$ (100) substrate at 900°C. b) Enlarged XRD ϴ-2ϴ feature around the 002 reflection.

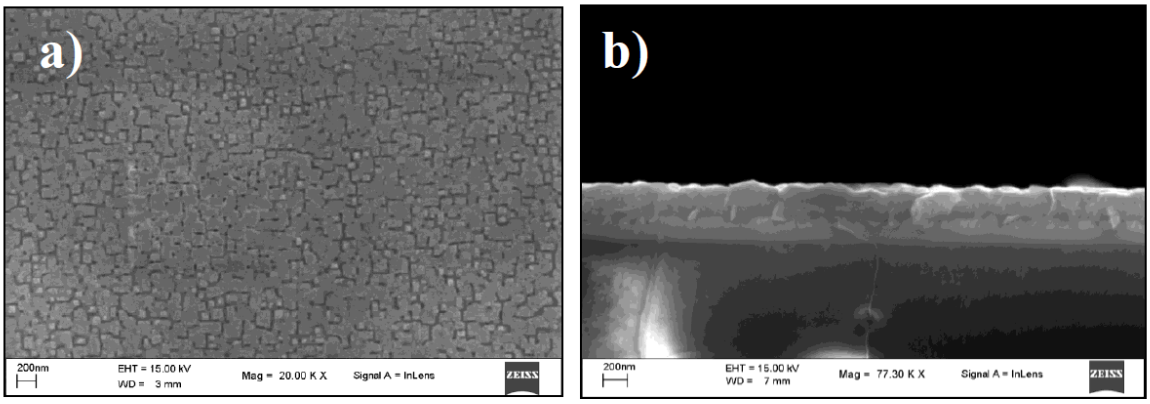

Fig. 4.1.2.6 a) FE-SEM image and b) cross section image of $LaCoO_3$ thin film on $LaAlO_3$.

These results are interesting since they open the route to the fabrication of the $La(Sr)CoO_3$ films, that represent a widely studied electrode for the SOFCs[26].

4.2 Perovskite $BaCeO_3$ thin films

The barium cerate ($BaCeO_3$) material has a perovskite structure.[27,28] It has a distorted perovskite-like structure characterized by a considerable tilting of MnO_6 octahedra (Fig-4.2.1).The octahedra tilting is observed when A in a perovskiteABO_3structureis too small for the dodecahedral site, allowing the decrease of the bond distance A-O while maintaining that of B-O.

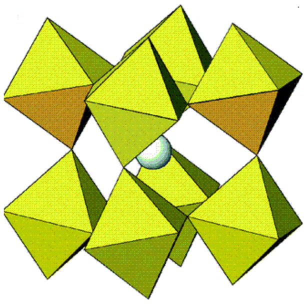

Fig-4.2.1 Tilting of MnO_6octahedra.

In addition, $BaCeO_3$ materials possess three different phases, depending on temperature, that have significantly different structural characteristics.[29,30] These different structures give to the barium ceriate different properties. In particular, the ionic conduction is due to the rhombohedral phase.[31]

Doped barium cerate $BaCe_{1-x}R_xO_{3-\alpha}$ (R=rare earth) materials exhibit outstanding mixed electronic and ionic conductivity useful for applications in fuel cell, sensor, and ceramic membrane technology.[32,33] More recently, doped $BaCeO_3$ system has drawn special attention as the substitute electrolyte materials for low temperature-SOFC, due its high proton conduction over the wide temperature range of 300 to 1000 °C.[34,3536]Fuel cells using a proton conducting ceramic as electrolyte can operate at considerably lower temperature than the oxygen conducting ceramic based FC. Compared with typical oxide ionic conductors solid oxide, proton conductors show much lower activation energy for proton transporting and this facilitates SOFCs based on proton-conducting electrolyte to attain high performances at low operating temperatures. In particular, solid electrolytes with high protonic conductivity exhibit good stability, high ionic transport rates for protons and can operate in the 500-700°C temperature range which is optimal for in-situ catalysis reactions. A prerequisite for introducing protonic conductivity to these perovskite oxides is the presence of oxygen vacancies. Oxygen vacancies can be introduced by doping with trivalent elements on the B site.[37] Thus, the development of new materials and suitable electrolyte film-deposition techniques is a great challenge to be addressed for achieving lower SOFC operating temperatures.

4.2.1 Thermal properties of the precursors and MOCVD growth

Preliminary experiments have been carried out to establish the MOCVD deposition parameters suited to produce doped barium ceriate thin film. $BaCeO_3$ films have been deposited in a horizontal hot-wall, low-pressure MOCVD reactor from a mixture consisting of the $Ba(hfa)_2$•tetraglyme and $Ce(hfa)_3$•diglyme adducts. Depositions have been carried out on MgO (100) substrates at 800-950 °C range temperature for 60 minutes, using Ar as carrier gas (150 mL/min) and oxygen flow (800 mL/min) as reaction gas, under 8 Torr total pressure. The precursors have been loaded inside the reactor in two separate Al_2O_3 boat located in the vaporization zone and resistively heated at different vaporization temperature. Differently from other MOCVD processes reported in this work which use a molten single source of precursors, in this case, to obtain the required stoichiometry of the deposited phase, it is necessary to use them separately. In fact, by comparing the thermal properties of the two precursors, obtained through thermogravimetric analysis (fig.4.2.1.1), it is evident that they have different volatilities.

The termogravimetric curves show that both the Ce and Ba precursors evaporate with a clean process without any-side decomposition.

The $Ba(hfa)_2$•tetraglyme evaporates in a single step in a 190°C a 290° temperature range with a low residue (≈2%) left at 450°C. The $Ce(hfa)_3$•diglyme evaporates in a single step in a narrow temperature range (150°C a 250°C) with a low residue (≈2%) left at 450°C .

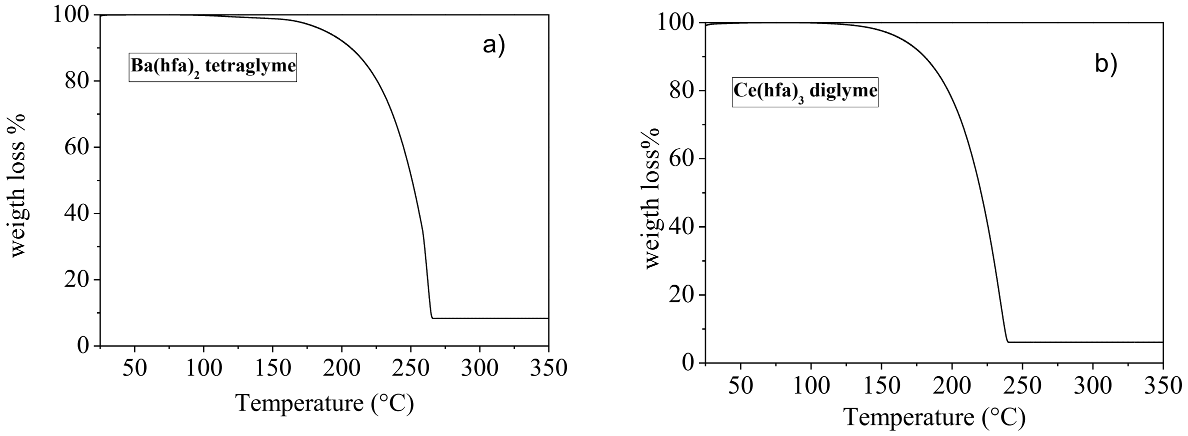

Fig. 4.2.1.1 Termogravimetric curves of a) $Ba(hfa)_2$•tetraglyme and b) $Ce(hfa)_3$•diglyme precursors.

4.2.2 Structural and morphological characterization of BaCeO$_3$ thin film.

The structural characterization of the film deposited in the temperature range of 800-950°C has been obtained by XRD patterns (Fig. 4.2.2.1a).The XRD measurement indicate that the formation of the BaCeO$_3$ phase depends upon the deposition temperature. Thus the patterns of films deposited at 800 and 850°C show the formation of the BaCeO$_3$ oriented (001) phase at $2\Theta=28.8°$ and 59.25°, while the peak at $2\Theta=25.00°$ is due to the BaF$_2$ phase and the peaks at $2\Theta=33.2$ and 69.5° are due to the oriented (100) CeO$_2$ phase that disappear at 900°C. At 950°C is present only the BaCeO$_3$ phase. The grain dispersion has been investigated by measuring the ω-scans (rocking curve) of the (002) peak at 28.8 (fig.4.2.2.1 b). The full width at half maximum (FWHM = 0.8°) value points to a good out-of-plane alignment of the BCO films. The compositional information has been carried out by energy dispersive x-ray analysis on BCO deposited at 950°C . The EDX spectra (Fig. 4.2.2.2) show the Ba L lines span in the 4.3–5.5 keV, and at4.8–5.9keV due the Cerium L lines. Great care has been taken to quantify these elements due to the partial overlap of the Ba and Ce L lines. EDX spectra indicate that using this operative condition a nearly correct stoichiometry (1.00 ± 0.05:0.96 ± 0.04) is achieved.

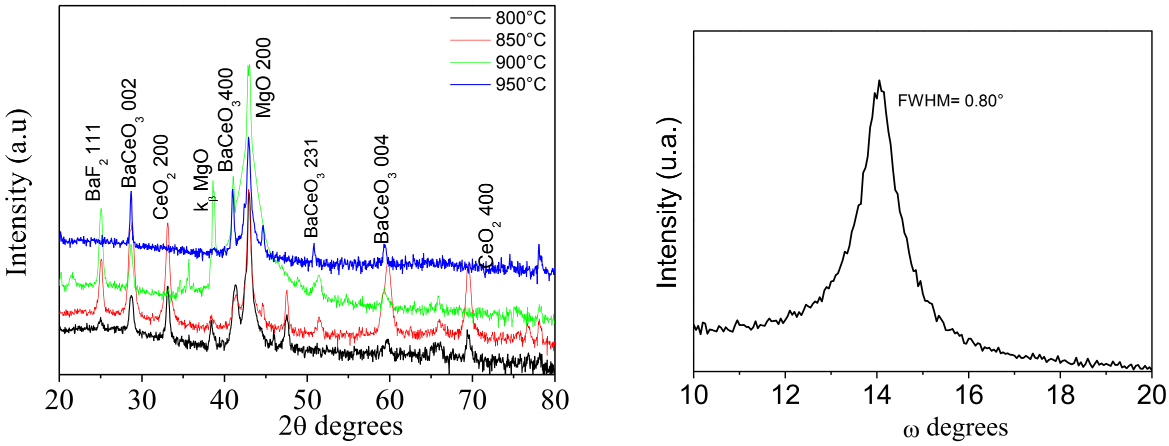

Fig.4.2.2.1 XRD patterns a) of BaCeO$_3$ thin films deposited in the 800-950°C temperature range. b) Rocking curve of the film deposited on MgO at 950°C.

The SEM investigations (fig 4.2.2.3) show surfaces that are not very uniform and homogeneous in the overall deposition temperature. Present data indicate that the experimental conditions are suited for the formation of the desired BaCeO$_3$ phase, nevertheless, further work is needed to improve the surface morphology and to produce doped thin films on suitable substrates, to increase the protonic conduction of the materials.

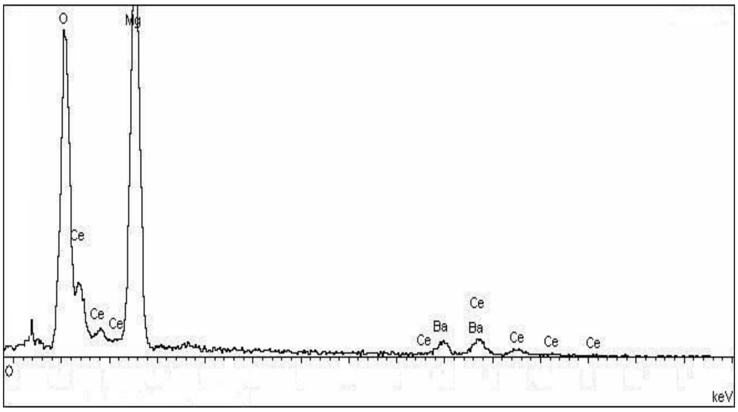

Fig.4.2.2.2 EDX spectrum of the $BaCeO_3$ film deposited on MgO at 950°C.

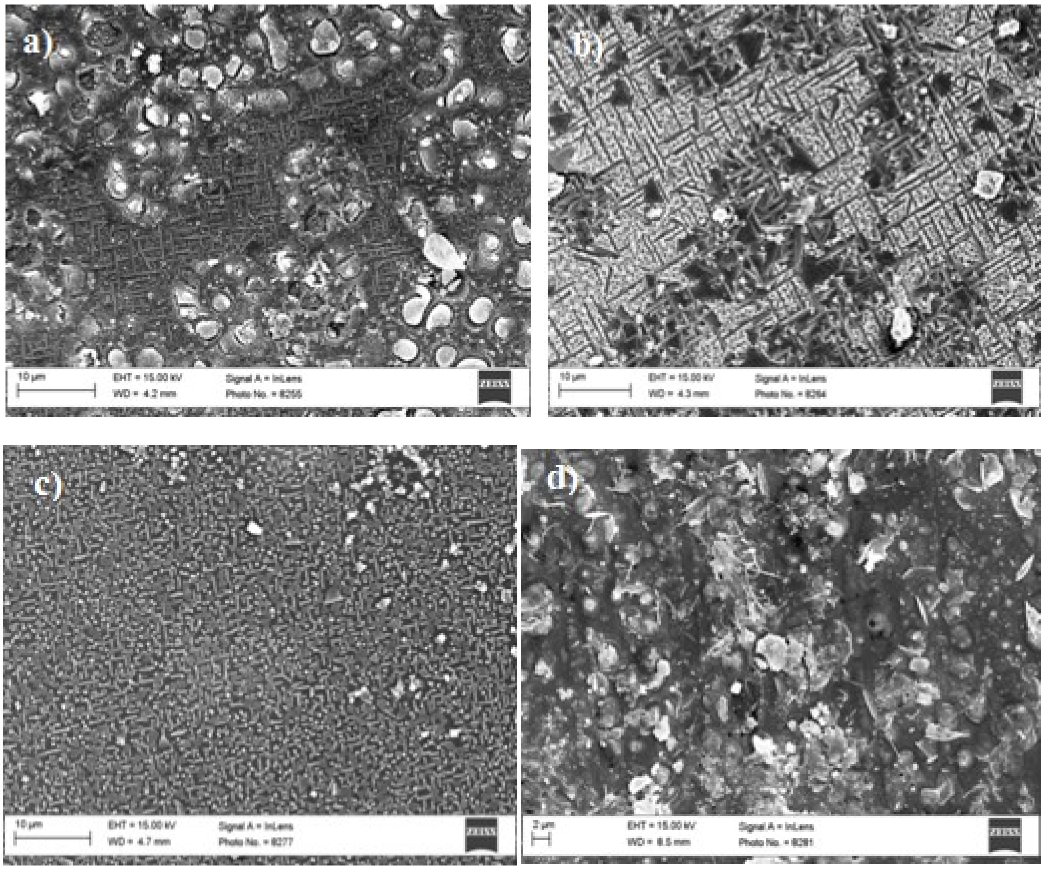

Fig 4.2.2.3 FE-SEM images of $BaCeO_3$ film obtained at a)800°C b)850°C c)900°C d)950°C.

References

---

1 A. Lashtabeg, S. J. Skinner, J. Mater. Chem. 16 (2006) 3161.

2 A.B. Stambouli, E. Traversa, Renewable and Sustainable Energy Reviews 6 (2002) 433;

3 B. C. H. Steele, A. Heinzel, Nature 414 (2001) 345;

4 X. Jiang, H. Huang, F. B. Prinz, S. F. Bent, Chem. Mater. 20 (2008) 3897.

5 K. Asai, O.Yokokura, N. Nishimori, H.Chou, J. M Tranquada, G.Shirane, S.Higuchi, Y.Okajima, K.Kay Phys. Rev. B 50 (1994) 3025

6 M. Losurdo, A. Sacchetti , P. Capezzuto, G. Bruno; L. Armelao ;D. Barreca;G. Bottaro, A. Gasparotto; C. Maragno, E. Tondello Appl. Phys. Lett. 87 (2005) 061909/1.

7 M. Daturi, G. Busca, R. Willey, Chem. Mater. 7 (1995) 2115.

8F.Patel, S.Patel, D.Gupta, D.Acharya, J. Envir. Res. Develop. 6 (2012) 964

9 M. Zawadzki, J. Trawczynski, Catalysis Today 176 (2011) 449

10 B.C.H. Steele, A. Heinzel, Nature 414 (2001) 345.

11 A. Yu Zuev, V. V. Sereda, D. S. Tsvetkov, J. Electrochem. Soc. 159 (2012) F594.

12W.S. Choi, J.-H. Kwon, H. Jeen, J.E. Hamann-Borrero, A. Radi, S. Macke, R. Sutarto, F. He, G.A. Sawatzky, V. Hinkov, M. Kim, H.N. Lee, NanoLett. 12 (2012) 4966

13 G.E. Sterbinsky, P.J. RyanKim, J.-W. KIM, E. Karapetrova, J.X. Ma, J. Shi, J.C. Woicik, Phys. Rev. B 85 (2012) 020403/1.

14 M. R. Catalano, R.G. Toro, A. Gulino, G. Malandrino Surf. and Coat. Technol. (2013), 230, 174-179

15 L.C. Tzavellas, C. Tsiamis, C.A. Kavounis, C.J. Cardin, Inorg. Chim. Acta 262 (1997) 53.

16 D. Briggs, J.T. Grant, in: D. Briggs, J.T. Grant (Eds.), Surface Analysis by Auger and X-Ray Photoelectron Spectroscopy, IMP, Chichester, 200

17 G. Malandrino, G.G. Condorelli, R. Lo Nigro, Chem. Vap. Depos. 10 (2004) 171

18 G. Malandrino, I.L. Fragalà, P. Scardi, Chem. Mater. 10 (1998) 3765

19 R.D. Shannon, ActaCrystallogr. Sect. A 32 (1976) 751

20 S. Xu, Y. Moritomo, K. Mori, T. Kamiyama, T. Saitoh, A. Nakamura, J. Phys. Soc. Jpn. 70 (2001) 3296

21 J. McAleese, J. C. Plakatouras , B. C. H. Steele, Thin Solid Films 280 (1996) 152.

22 J. A. Villoria, M. C. Alvarez-Galvan, S. M. Al-Zahrani, P. Palmisano, S. Specchia, V. Specchia, J. L. G. Fierro, R. M. Navarro, Appl. Catal. B: Environ. 105 (2011) 276–288.

23 S. Xu, Y. Moritomo, K. Mori, T. Kamiyama, T. Saitoh, A. Nakamura, J. Phys. Soc. Jpn. 70 (2001) 3296.

---

24 H. Taguchi, S. Yamada, M. Nagao, Y Ichikawa, K. Tabata, Mater. Res. Bull. 37 (2002) 69-76.

25 A. Gulino, P. Dapporto, P. Rossi, G. Anastasi, I. Fragalà, J. Mater. Chem. 14 (2004) 2549-2553.

26A. kajo, J. vanHerle, D. Favrat, Fuel Cells 11 (2011) 537.

27M. Winter, R. J. Brodd, Chem. Rev. 104, (2004)4245-4269

28M. Shi, M. C. Falub, P. R. Willmott, J. Krempasky, R. Herger, L. Patthey, K. Hricovini, C. Falub, M. Schneider, Condensed Matter (2005).

29M. Preda, R. Dinescu, Rev. Roum. Chim., 21(1976) 1023

30 T. Scherban, R. Villeneuve, L. Abello, G. Lucazeau, RamanSpectrosc., 24 (1993) 805

31K. Takeuchi, C. K. Loong, J. W. Richardson Jr., J. Guan, S. E. Dorris, U. Balachandran, Solid State Ionics, 138 (2000)63-77.

32 H. Iwahara, Solid State Ionics 77 (1995) 289.

33 K.D. Kreuer, Chem. Mater. 8 (1996) 610

34HiroyoHosono, Tohru Higuchi, Takeshi HattoriJ. OF AP, PHYs.104(2008), 113704

35PengRanrana, Wu Yan b, Yang Lizhaia, Mao ZongqiangSolidState Ionics 177 (2006) 389 – 393

36LingYihan; Chen, Jie; Wang, Zhenbin; Xia, Changrong; Peng, Ranran; Lu, YalinInter.J. of Hydrogen Energy 38(18), (2013), 7430-7437.

37E. Fabbri, D. Pergolesi, E.TraversaChem. Soc. Rev 39(2010), 4355–4369

Chapter 5: Multiferroic perovskite $BiFeO_3$ film.

Multiferroics magnetoelectric materials are of great scientific interest due their several tecnological applications, such as sensor electronics, spintronics, the non-volatile memory of the latest generation and photovoltaics.[1,2]

In multiferroics two of the three ferroic properties, ferroelectricity, ferromagnetism (antiferromagnetism) and ferroelasticity, occur in the same phase.

In order for a multiferroic material to present magnetoelectric property it is not sufficient that it possesses both ferromagnetic and ferroelectrical properties, but there must be the possibility of having coupling between these properties. Among multiferroic materials bismuth ferrite ($BiFeO_3$) has attracted a lot of attention in the last decades since it is probably the only material that is both magnetic and ferroelectric at room temperature.[2,3] Nevertheless, defects, non-stoichiometry and/or the valence fluctuations of Fe ions (Fe^{2+}or Fe^{3+}), creating oxygen vacancies for charge compensation, give rise to films having low resistivity. As a consequence, the ferroelectric loop is difficult to be observed at room temperature; however this problem can be resolved by doping the $BiFeO_3$ phase or by epitaxial strain[4] of $BiFeO_3$ in form of thin film.The principal way to obtain magnetoelectrical materials are:[5]

- single phase thin film in which the magnetoelectrical coupling is due to the doping of systems by substitution at the A and/or B sites (fig 5. 1a)
- Horizontal multilayer heterostructures in which the interfacial hetero-epitaxial between the two layer produce magnetoelectrical coupling (fig 5.1b));
- Nanocomposites formed by magnetic nanopillars in a ferroelectrical matrix (vertical hetero- epitaxial) (fig 5.1c)

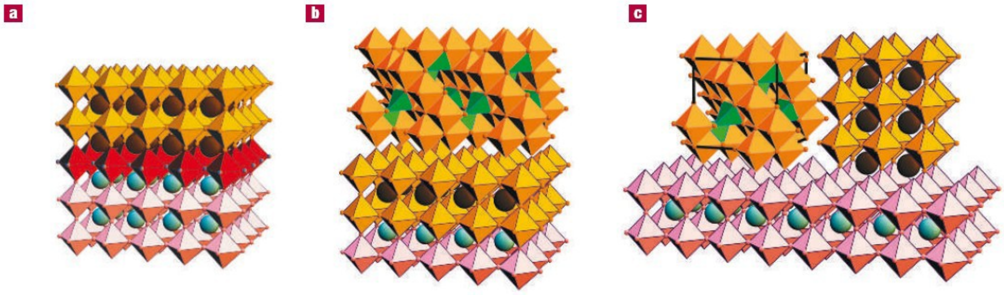

Fig.5.1 Sistems with magnetoelectrical coupling by a) doping single phase thin film; b) horizontal hetero-epitaxial; c) vertical hetero-epitaxial.

In this context, a lot of research has been devoted to the optimization of the undoped $BiFeO_3$ as well as on preparation of doped systems by substitution at the A, i.e. rare earth elements,[6] and/or B sites. Horizontal multilayers have been obtained by alternating a ferroelectric phase(such as $BaTiO_3$) and an ferro/ferromagnetic (eg. $CoFe_2O_4$)[7] Among the nanocomposites the most investigated is formed by nanopillars of $CoFe_2O_4$ in a $BiFeO_3$ matrix. [8,9]

In this context, the application of a simple and highly versatile synthetic approach such as MOCVD has been used to synthesize undoped and doped $BiFeO_3$ films.

5.1 Undoped multiferroic $BiFeO_3$ films

5.1.1 Thermal properties of the precursors and MOCVD growth

A lot of research has been devoted to the synthesis of $BiFeO_3$ and to the study of its ferroelectric properties at the nanoscale level. Several deposition methods have been used for the growth of $BiFeO_3$ films on various substrates. Recently, piezoresponse force microscopy (PFM) has emerged as a powerful and versatile tool for probing piezoelectrics and ferroelectrics properties at the micrometer and nanometer scales[10].

Two strength points of this technique are the possibility to study piezoelectric/ferroelectric phenomena at the nanoscale, such as the study of single domains dynamics, and the use of a non-invasive approach which does not require sample manipulations (i.e deposition of top-electrodes). Very few papers reported on the PFM evaluation of the piezoelectric and ferroelectric properties at the nanoscale level of MOCVD grown $BiFeO_3$films.[11,12]

The $BiFeO_3$ thin films have been deposited in a low pressure, horizontal, hot wall MOCVD reactor[13] in the 700°C-800°C range on $SrTiO_3$(100) and single crystal conducting $SrTiO_3$:Nb (100) substrate,[14] used to allow piezoresponce measurements since it acts as bottom electrode. The mixture of precursors, consisting of Bi(phenyl)$_3$/Fe(tmhd)$_3$ mixture, tested at two different molar ratios, namely 1.0:1.0 and 1.0:0.6, have been investigated by dynamic and isothermal thermogravimetric measurements (Fig 5.1.1.1.a).The thermogravimetric analysis of the precursor mixture with a molar ratio of 1.0:0.6, show a single step, indicating that the mixtures evaporate without decomposition in the temperature range of 140-250°C with low a residue (>5 %).Isothermal curves (Fig.5.1.1.1.b), measured in the 140–180 °C range show a linear behavior in almost all the investigated range, with negligible deviations only for the 180 °C plot. The same results have been obtained for the precursor mixture with a molar ratio of 1.0:1:0.

It is important to underline that the good thermal properties of the mixture at atmospheric pressure point to an even better behavior in MOCVD processes under vacuum.

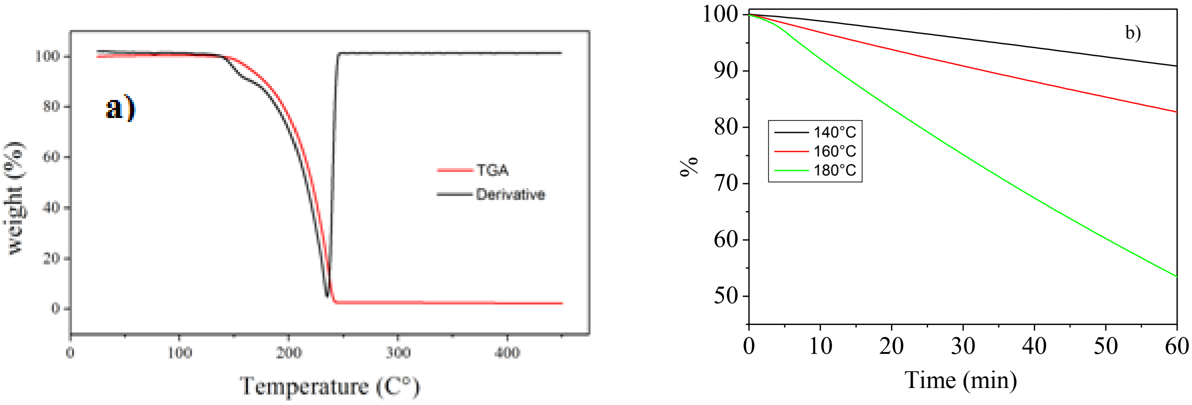

Fig. 5.1.1.1 a) Dynamic thermogravimetric curve and isothermal analysis of $Bi(phenyl)_3/Fe(tmhd)_3$ mixture precursors.

The quantitative EDX analyses, carried out on several areas over the whole 10x 10 mm^2 sample surface, indicates that the suited Bi:Fe ratio (1.0±0.1:1.0 ±0.1) can be obtained in the 700-800°C range from $Bi(phenyl)_3/Fe(tmhd)_3$ mixtures ranging from 1.0:1.0 for the higher temperatures (800°C) to 1.0:0.6 for lower temperatures (750-700°C).In addition, EDX data show the presence of a very low C content in all films.

X-ray diffraction (XRD)of films deposited in the 700-800°C range (Fig.5.1.1.2) show only 00ℓ reflections in addition to the $SrTiO_3$100 and 200 reflections at 22.75° and 46.55°. The presence of only 00ℓ reflections points to the formation of an highly oriented film for all the investigated deposition conditions. Other information on the out-of-plane alignment has been obtained from the rocking curve of the 200 $BiFeO_3$ reflection. The rocking curve shown in the inset of Fig.5.1.1.2 (FWHM=0.29°) confirms that the film is highly oriented with a very low dispersion of grains.

Additional information about the crystalline structure of the $BiFeO_3$ has been investigated by a series of θ-2θ scans, in a suited 2θ range, varying the χ angle (where χ represents the angle between the normal to the film surface and the plane of the X-ray beam) to detect the most intense (hk0) reflections. A set of measurements has been carried out in the θ-2θ range of 20-60° upon varying the χ angle from 0 to 70°.

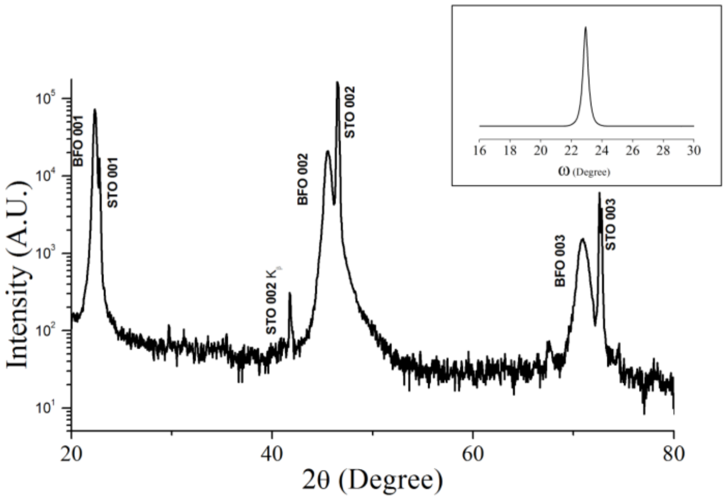

Fig. 5.1.1.2. XRD pattern of $BiFeO_3$ films deposited on $SrTiO_3$:Nb (001) at 800°C. The inset reports the rocking curve of the (200) peak

The θ-2θ scan (fig. 5.1.1.3) in the range 50-54° at χ angle equal to 26° is reported. The peak at 52.33° is attributed to the 210 reflection of the $SrTiO_3$ substrate, while the peak at lower angle is due to the $BiFeO_3$ sample. The position of the peak and the value of χ at which is observed clearly point to the assignment of the peak as the 210 reflection considering for $BiFeO_3$ a pseudocubic structure. Actually, two peaks are present, that match those expected for a rhombohedral $BiFeO_3$ structure even though slightly shifted at lower angles (theoretical positions are indicated with blue lines).

Considering the position of the $SrTiO_3$:Nb substrate as a peak reference, the in-plane cell parameter has been estimated to be a= 3.9826 Å. This value is slightly different from that reported of 3.965 Å, but the difference is too small to consider the formation of a tetragonal phase.

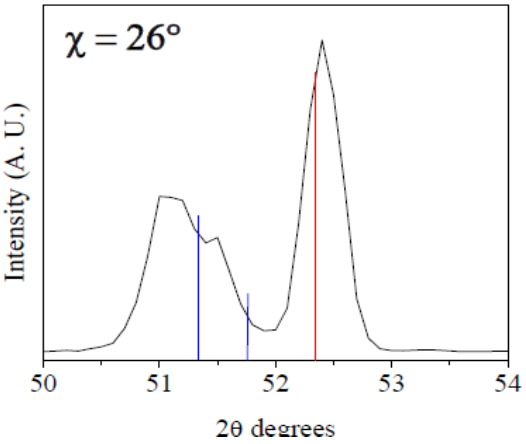

Fig.5.1.1.3. θ-2θ XRD pattern at χ = 26° of a $BiFeO_3$ film grown on $SrTiO_3$:Nb (001).

This finding is in accordance with data reported in the literature, which propose a tetragonal distortion only for very thin films, i.e. thickness lower than 100 nm.[15] In the present case, the thickness of the $BiFeO_3$ film obtained by the present MOCVD approach, varies from 800 nm (700 °C) to 500 nm (800 °C).

The epitaxial nature of the $BiFeO_3$ film and its relationship with the substrate have been also studied. The 210 pole figure (Fig. 5.1.1.4 a) shows two major different sets of four poles at $\chi \approx 26°$ and $\chi \approx 63°$, each set every 90° of ϕ. This sets of poles are due, respectively, to the $\chi_{(210)(100)} = 26°$ and $\chi_{(210)(010)} = 63°$ calculated through the following equation:

$$\cos\chi_{(h_1k_1l_1)-(h_2k_2l_2)} = \frac{h_1h_2 + k_1k_2 + l_1l_2}{\sqrt{\left(h_1^2 + k_1^2 + l_1^2\right)\times\left(h_2^2 + k_2^2 + l_2^2\right)}}$$

The 110 pole figure of the $SrTiO_3$:Nb (100) substrate (fig.5.1.1.4b), show four poles at $\chi=45°$ and every 90° of ϕ. These poles are perfectly aligned with respect to the two sets found for the sample, thus indicating that films are epitaxially grown on the $SrTiO_3$ (100) substrate.

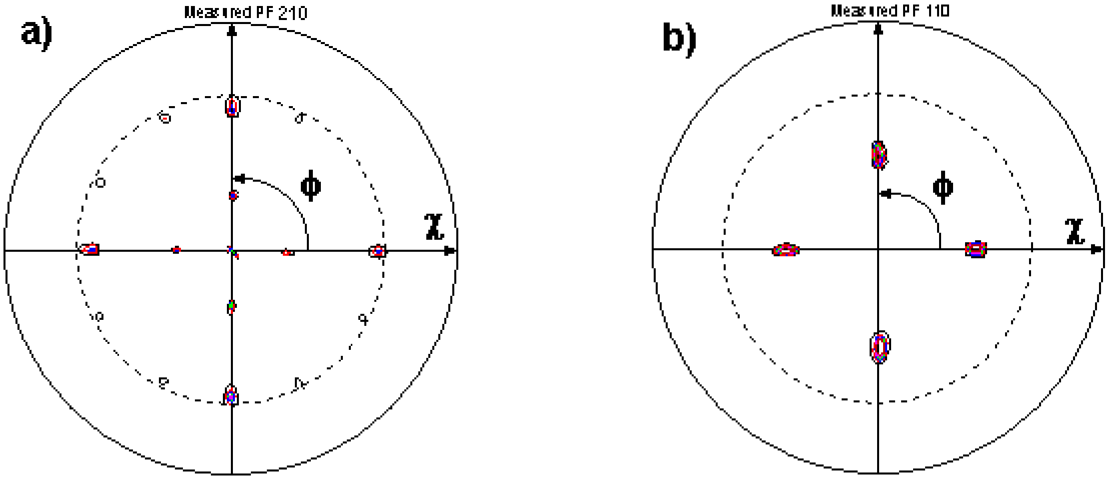

Fig. 5.1.1.4 a) Pole figure (210) of the $BiFeO_3$ film and b) pole figure (110) of the $SrTiO_3$:Nb (100)substrate.

Morphology of $BiFeO_3$ films deposited at 800°C, 750°C and 700°C are reported in Figure 5.1.1.5. The films deposited at 800 °C (fig. 5.1.1.5a) show a very flat surface formed by the coalescence of big flat grains with some pinholes. Note that despite the presence of some big grains in the topographical image obtained by secondary image, the backscattered secondary electron (BSD) image (Fig. 5.1.1.5b) of the same zone shows an homogeneous contrast between flat surface and crystals. This similarity in the electron backscattered image indicates that all the feature of the images have a similar atomic composition.

Lowering substrate temperature to 750°C, films are formed by big flat plate-like grains, not fully coalesced, thus the film morphology consists of a flat surface with voids between grains acting as larger pinholes (Fig. 5.1.1.5c). At 700°C, film morphology is dominated by the plate-like grains, not yet coalesced and, therefore, separated by larger voids (Fig. 5.1.1.5d).

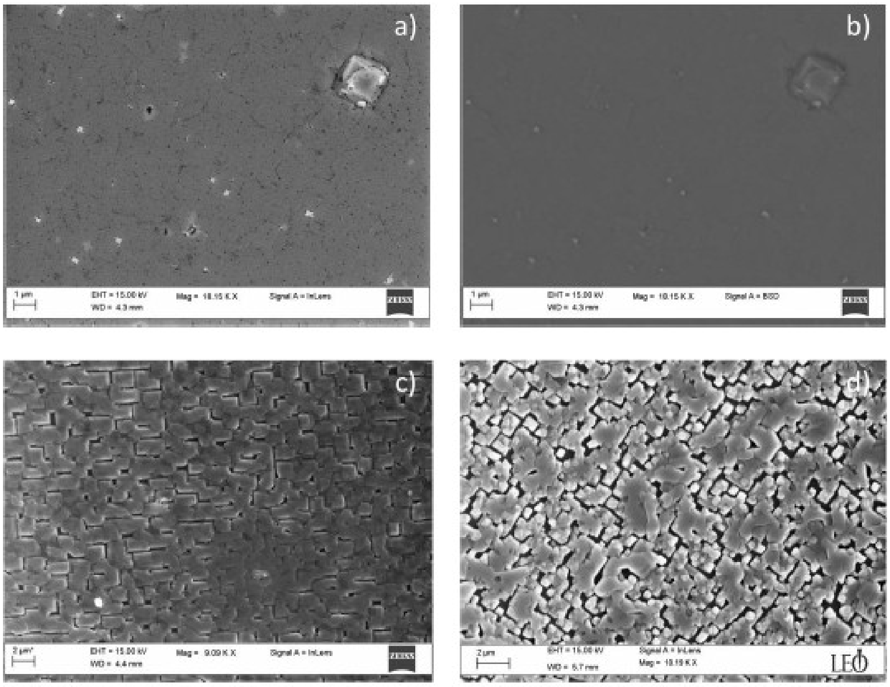

Fig. 5.1.1.5 FE-SEM images of secondary a) and backscattered b) electrons of $BiFeO_3$ film deposited at 800°C. FE-SEM secondary electron images of $BiFeO_3$ film deposited at c) 750°C and d) 700°C.

5.1.2 Piezoelectric and ferroelectric properties of the $BiFeO_3$ films

The piezoelectric properties of obtained $BiFeO_3$ (001) films have been evaluated by piezoresponce force microscopy (PFM).

The images of the topography and of the phase difference between applied oscillating potential V_{ac} and the vertical piezoresponce Z_{ac} of the (001) $BiFeO_3$ films deposited at 800°C are reported in Fig. 5.1.2.1a and Fig. 5.1.2.1b, respectively. From the comparison between topographic and phase images, it is evident the presence of domains (labeled as A and B) showing different piezoelectric responses (in term of phase difference). This behavior suggests that the polarization of as-grown domains, which lies along the [111] direction of the pseudocubic structure, is oriented in some cases in the upward directions and in other cases downwards.

Single point piezoresponce force spectroscopy (PFS) (Figure 5.1.2.1c) obtained with a round trip of ±8V tip bias has been performed on domains labeled as B. The plot shows that the dependence of the phase difference and, therefore, of the polarization direction upon tip bias follows an hysteresis loop with a coercive voltage of about 2V. This behavior indicates that it is possible to determine the polarization direction of the ferroelectric domains (writing) by applying a suited potential to the AFM tip.

Therefore, a new experiment (writing) has been performed by applying a -8V bias to the tip which is moved along the previous investigated 10x10 μm area. After the writing, the new phase image (Fig. 5.1.2.1d) does not show the different domains previously observed but a uniform polarization in the same direction of domains previous labeled as A.

Fig. 5.1.2.2 shows the images of the topography, (a), and phase difference (b) of the (001) $BiFeO_3$ film deposited at 750°C. Analogously to the case of the film deposited at 800C° different domains can be identified from the contrast of the phase image. To better evaluate the piezoelectric/ferroelectric behavior, single-point PFS have been performed on the bright domains. The phase dependence on bias upon a round trip of ±5V tip bias (Fig. 5.1.2.2c) shows a much more narrow hysteresis loop, thus indicating a lower quality of the ferroelectric properties. In this case, the writing of the ferroelectric domains with a potential applied to the tip, followed by the acquisition of the phase image did not lead to evident uniform orientation of all the ferroelectric domains.

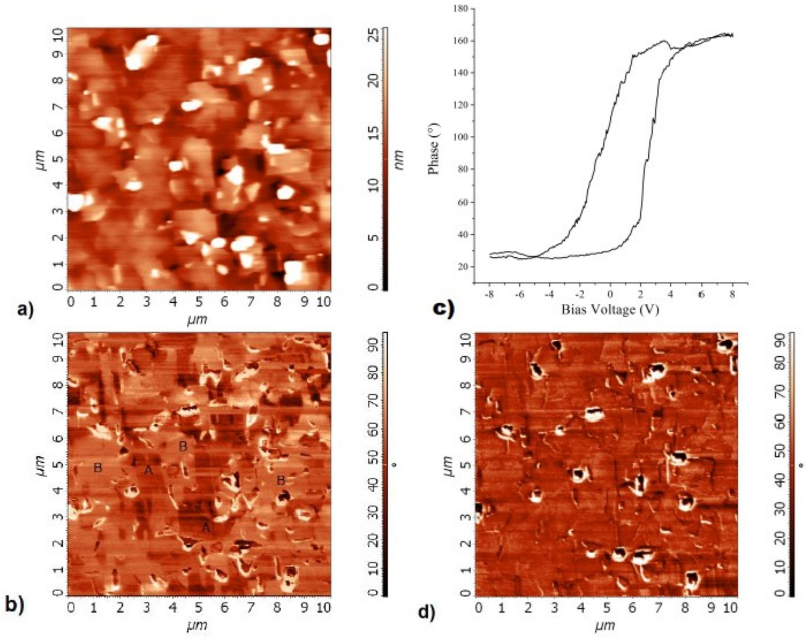

Fig.5.1.2.1 PFM and PFS characterization of a (001) $BiFeO_3$ film deposited at 800°C. Topographic a) and b) vertical PFM phase shift images of the as-grown film: A and B indicate domains with different PFM responses; c) single point PFS hysteresis loop obtained on domain B by applying a round trip ±8V tip bias; d) vertical PFM phase shift image after full area pre-writing with a -8V tip bias.

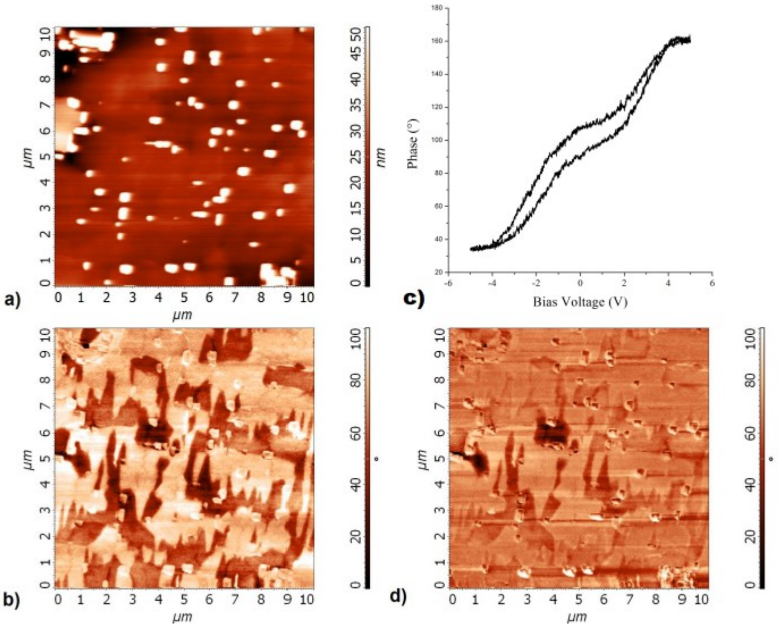

Fig.5.2.2 PFM and PFS characterization of a (001) $BiFeO_3$ film deposited at 750°C. Topographic a) and b) vertical PFM phase shift images of the as-grown film; c) single point PFS hysteresis loop obtained on bright domain by applying a round trip ±5V tip bias voltage; d) vertical PFM phase shift image obtained performing PFM scanning with an additional -4V tip bias.

Nevertheless, it was possible to observe uniformly oriented ferroelectric/piezoelectric domains in the phase image (Fig.5.1.2.2d) by applying, besides the V_{ac} signal, a -3V tip bias during PFM scanning. Adopting this approach it was possible to determine the orientation of the piezoelectric domains, despite the poor hysteresis.

On the basis of the present investigation, it is possible to conclude that Piezoelectric/ferroelectric properties are slightly worse in films deposited at lower temperatures. Present data indicate that deposition temperature plays a crucial role since, even though the crystalline structure is independent on temperature, morphology and piezoresponce properties are strictly related to the deposition temperature.

5.2 $BiFeO_3$ Films Doped in the A or B Sites

5.2.1 Thermal properties of precursors and MOCVD growth

$BiFeO_3$ thin films have been doped at the A or B sites with Ba and Ti elements, respectively. Few studies have been reported on the preparation of $BiFeO_3$ films doped with Ba[16] or Ti,[17], obtained mainly using pulsed laser deposition technique. In the present study, $Bi_{1-x}Ba_xFeO_3$ and $BiFe_{1-y}Ti_yO_3$ films have been deposited on YSZ (100) and $SrTiO_3$ (100) substrates. Depositions have been carried out for 60 min at 5 torr at 800° C, on (100) $SrTiO_3$ and (100)

YSZ single crystals, using a single source mixture consisting of the Bi(phenyl)$_3$/Fe(tmhd)$_3$/Ba(hfa)$_2$•tetraglyme precursor mixture to deposit $Bi_{1-x}Ba_xFeO_3$ thin films and the Bi(phenyl)$_3$/Fe(tmhd)$_3$/Ti(tmhd)$_2$(O-iPr)$_2$ precursor mixture to deposit $BiFe_{1-y}Ti_yO_3$ films. The precursor mixtures have been heated at 120°–130°C, a suitable temperature for an efficient vaporization without thermal degradation. Argon was used as a carrier gas (flow = 150 sccm/min), while the reactant gas (oxygen flow = 150 sccm/min) was introduced in the main flow in close proximity of the reaction zone. The thermal behaviour of the mixtures of Bi(phenyl)$_3$/Fe(tmhd)$_3$/Ba(hfa)$_2$•tetraglyme and Bi(phenyl)$_3$/Fe(tmhd)$_3$/Ti(tmhd)$_2$(O-iPr)$_2$ has been characterized by thermogravimetric analyses at atmospheric pressure under nitrogen flow.

The TG curves of the Bi(phenyl)$_3$/Fe(tmhd)$_3$/Ba(hfa)$_2$•tetraglyme and Bi(phenyl)$_3$/Fe(tmhd)$_3$/Ti(tmhd)$_2$(O-iPr)$_2$ mixtures , in 1.0:1.0:2.0 and 1.0:0.6:0.8 molar ratios respectively, show mainly a single step, indicating that the mixtures evaporate without decomposition in the temperature range of 120–280 °C with a low residue (~10%). To obtain epitaxial growth of the $BiFeO_3$ thin films, $SrTiO_3$(100) substrate with perovskite structure has been used. In fact, $SrTiO_3$ has a lattice parameter a_s= 3.9050 Å, while $BiFeO_3$ may be considered as a pseudocubic, having a rhombohedral structure with a_{rh}= 3.965 Å and α_{rh}= 89.4°. YSZ substrate, with a cubic structure and a larger a parameter of 5.139 Å, has been used to allow compositional analysis of the grown layers through energy dispersive X-ray analyses (EDX), since Ti is also present in the substrate and in the case of the $Bi(Ba)FeO_3$ system the L lines of Ba and the K lines of Ti would overlap hampering the Ba quantification. In fig. 5.2.1.2 are reported the XRD Θ-2Θ scans of Ba-doped $BiFeO_3$ films and Ti-doped $BiFeO_3$ films compared to undoped $BiFeO_3$ film.

The XRD patterns show only 00ℓreflections of $BiFeO_3$ in addition to the $SrTiO_3$ 100 and 200 reflections at 22.75° and 46.55° (Fig 5.2.1.1a). The presence of only 00 ℓreflections points to the formation of an highly oriented film. The out-of-plane cell parameter is a = 3.966 Å, which compares very well with the reported 3.965 Å value. The XRD patterns of the Ba doped and Ti doped films indicate that the dopants give rise to a shift of the 001 peak at lower angle in both cases (Fig.5.2.1.1b). This indicates larger a axes for the doped systems, respectively of 4.037 Å for the $Bi_{1-x}Ba_xFeO_3$ and of 4.130 Å for the $BiFe_{1-y}Ti_yO_3$ films. In addition, the pattern of the Ba doped film shows some additional peaks due to impurity phases, i.e., peaks at 26.65°, 49.85°, 63.95° and 64.90°. Most of these peaks may be likely due to a Ba–Fe–O containing phase, even though its univocal identification is not possible due to the great variety of Ba–Fe–O phases. The pattern of the Ti-doped film shows an impurity peak at 63.95°.

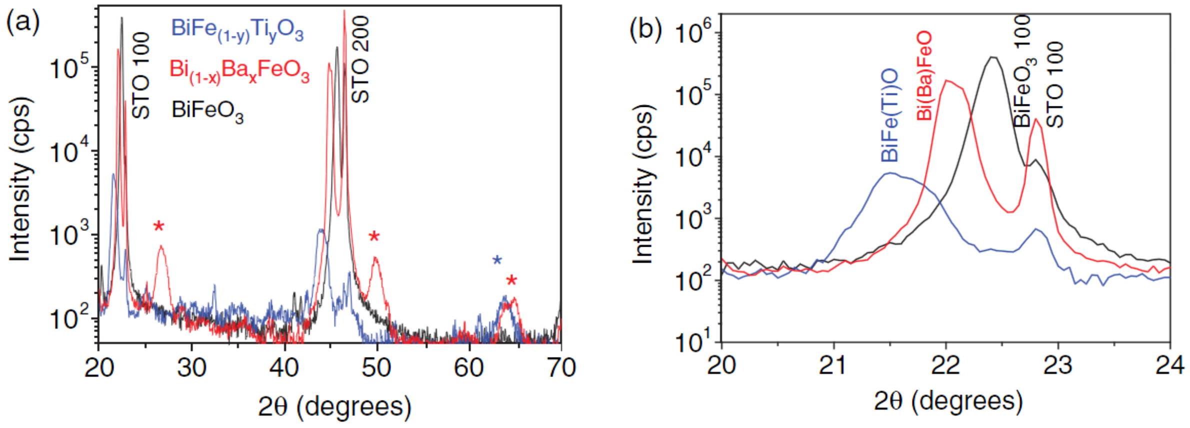

FIG. 5.2.1.1 XRD patterns of an undoped $BiFeO_3$, $Bi_{1-x}Ba_xFeO_3$ and $BiFe_{1-y}Ti_yO_3$ films on $SrTiO_3$ (100) substrates

Quantitative analyses obtained by EDX for films deposited on YSZ substrates, simultaneously with those deposited on STO substrate, represent well those of films deposited on $SrTiO_3$ substrates, since both substrates are monocrystalline and inert with respect to the deposited layer.

In the EDX spectra of the $Bi_{1-x}Ba_xFeO_3$(Fig.5.2.1.2a), the Bi M peak is observed at 2.440 keV, the Ba L lines span in the 4.3–5.5 keV and the Fe Kα Kβ and L peaks are observed at 6.355, 6.982 and 0.710 keV, respectively. The substrate Zr M lines are found at 2.176 keV. The quantitative EDX analyses carried out on several selected areas indicate that the Bi:Ba:Fe ratio of films grown at 800 °C from the above mentioned stoichiometric mixture is 0.52±0.05:0.49±0.05:1.0±0.1 over the whole 10×10 mm^2 surface. The EDX analysis (Fig.5.2.1.2b) of the $BiFe_{1-y}Ti_yO_3$ film shows in addition to the Bi and Fe peaks, the Ti K_α and K_β peaks at 4.520 and 4.920 keV, respectively, and points to a stoichiometric ratio of 1.0±0.1:0.61±0.05:0.47±005. In addition, EDX data show the presence of a very low C content, while in the case of the Ba doped sample no F contamination is observed.

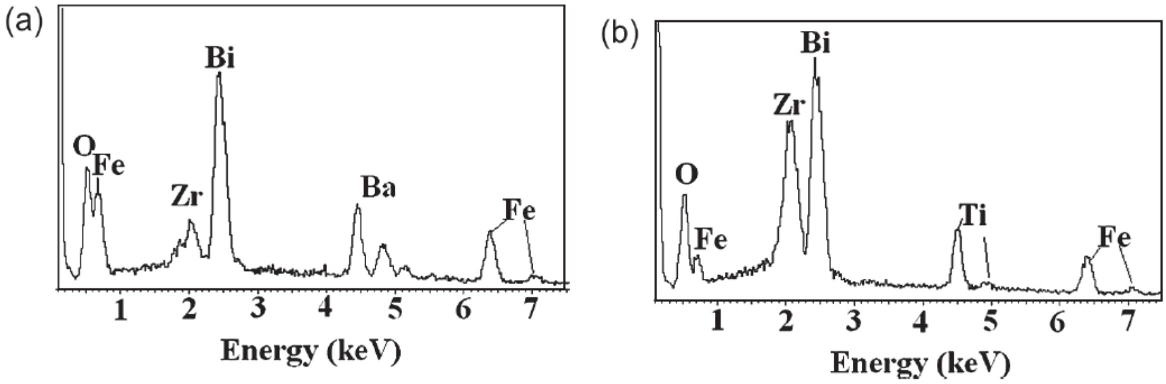

FIG 5.2.1.2 EDX spectra of the

a)$Bi_{1-x}Ba_xFeO_3$ (b) and b) $BiFe_{1-y}Ti_yO_3$ films on YSZ substrates.

The SEM images of films deposited at 800° C on $SrTiO_3$ (100) substrates show for all the films a uniform and homogeneous morphology (Fig.5.2.1.3). In particular, a very flat surface with some pinholes is observed for the undoped $BiFeO_3$ film (Fig. 5.2.1.3a). The morphology of the $Bi_{1-x}Ba_xFeO_3$ film is very homogeneous and flat as well (Fig.5.2.1.3b). In the case of the $BiFe_{1-y}Ti_yO_3$ very large plate-like grains of about 2 μm in size are present (Fig.5.2.1.3c).

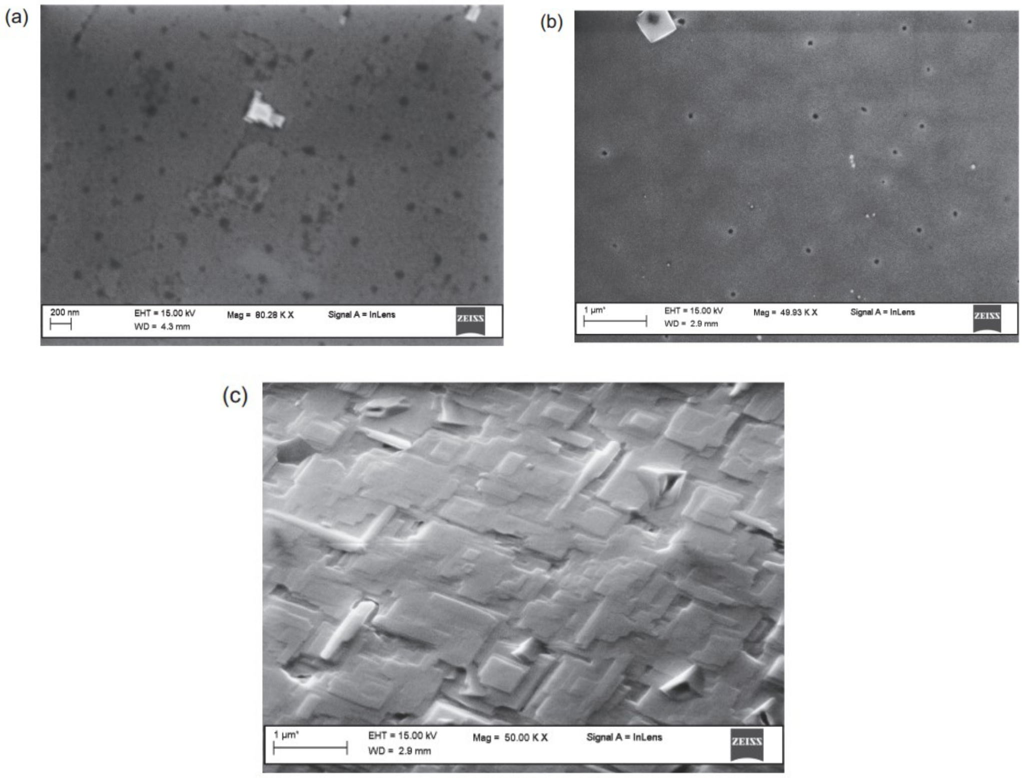

Fig. 5.2.1.3 FE-SEM images of the a) $BiFeO_3$ of b) $Bi_{1-x}Ba_xFeO_3$ and c) $BiFe_{1-y}Ti_yO_3$ films on YSZ substrates.

Other morphological information have been carried out by AFM measurements Fig(5.2.1.4).The root mean square (RMS) roughness of the $BiFeO_3$ surface (measured on a 10 µm×10µm area) shows a value of 5.26 nm. The $Bi_{1-x}Ba_xFeO_3$ shows a RMS roughness (measured on a 10 µm×10µm area) of 4.95 nm, while the $BiFe_{1-y}Ti_yO_3$ shows a RMS roughness (measured ona10 µm×10µm area) of 26.39 nm.

This synthetic in-situ MOCVD process,through which good quality $BiFeO_3$ films have been grown, is very appealing because it may be extended to simultaneously dope $BiFeO_3$ films with Ba and Ti, producing $Bi_{1-x}Ba_x$ $Fe_{1-y}TiyO_3$ solid solution or $(1-x)BiFeO_3$-$xBaTiO_3$nanocomposites.

.

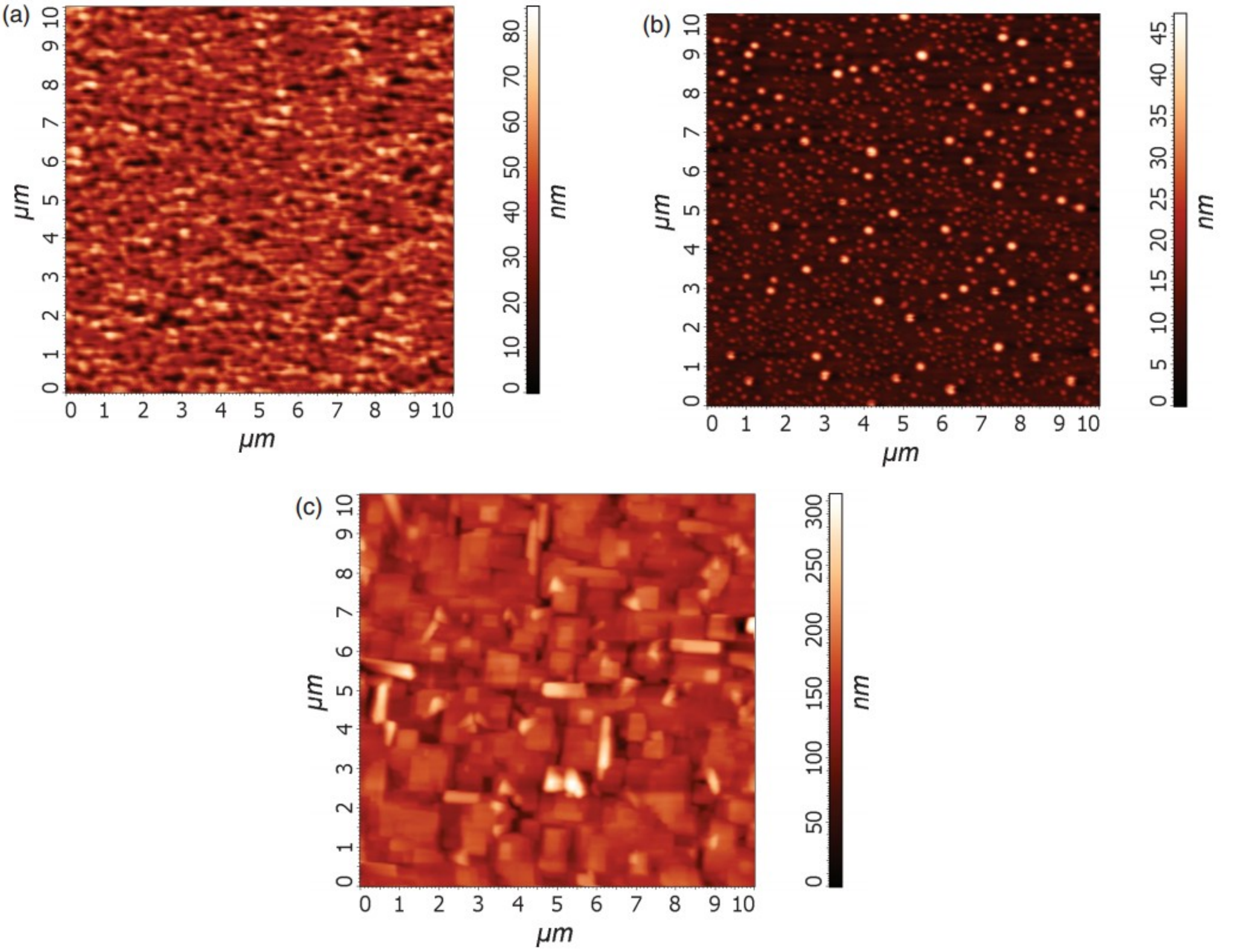

Fig 5.2.1.4 AFM images of the a) undoped $BiFeO_3$, of the b) $Bi_{1-x}Ba_xFeO_3$ and c) $BiFe_{1-y}Ti_yO_3$ films.

References

---

1 N. A. Spaldin, S.-W. Cheong, R. Ramesh, Physics Today, 63 (2010) 38

2 T. Choi, S. Lee, Y. J. Choi, V. Kiryukhin, S. W. Cheong, Science, 324(2009) 63-66

3 G. Catalan and J. F. Scott, Adv. Mater. 21 (2009) 2463.

4Liu, Huajun; Yang, Ping; Fan, Zhen; Kumar, Amit; Yao, Kui; Ong, Khuong Phuong; Zeng, Kaiyang; Wang, John Physical Review B: Condensed Matter and Materials Physics 87(22), (2013) 220101/1-220101/6.

R. Ramesh, N. A. Spaldin, Nature Materials, 6, (2007)21-29

6 D. Kan, L. Pàlovà, V. Anbusathaiah, C. J. Cheng, S. Fujino, V. Nagarajan, K. M. Rabe, I. Takeuchi, Advanced Functional Materials*,* 111 *(*2010)201108

7H. Zheng, J. Wang, S. E. Lofland, Z. Ma, L. Mohaddes-Ardabili, T. Zhao, L. Salamanca-Riba, S. R. Shinde, S. B. Ogale, F. Bai, D. Viehland, Y. Jia, D. G. Schlom, M. Wuttig, A. Roytburd, R. Ramesh, Science 303,(2004), 661-663

8N. Dix, R. Muralidharan, J. M. Rebled, S. Estradé, F. Peirò, M. Varela, J. Fontcuberta, F. Sànchez, ACS Nano4 (2010) 4955-4961

9F. Zavaliche, T. Zhao, H. Zheng, F. Straub, M. P. Cruz, P. L. Yang, D. Hao, R. Ramesh, Nano Letters, 7(2007)1586-1590

10N. Balke, I. Bdikin, S. V. Kalinin, A. L. Kholkin J. Am. Ceram. Soc., 92 (2009) 1629

11 M. S. Kartavtseva, O. Yu. Gorbenko, A. R. Kaul, S. Fusil, A. Barthelemy and K. Bouzehouane, Ferroelectrics 374 (2008) 20.

12 M. S. Kartavtseva, O. Yu. Gorbenko, A. R. Kaul, A. R. Akbashev, T. V. Murzina, S. Fusil, A. Barthelemy and F. Pailloux, Surf. Coat. Technol. 201 (2007) 9149.

13D. Scillato; N. Licciardello; M.R.Catalano; G. GCondorelli; R. Lo Nigro; G. Malandrino. Journal of nanosc. and nanotech. 11(9), (2011), 8221-5.

14 G. G Condorelli,.; M. R Catalano, E. Smecca, R: Lo Nigro, a; G. Malandrino,.Surf and Coat. Technology 230 (2013), 168-173

15A. R. Damodaran, S. Lee, J. Karthik, S. MacLaren, L.. W. Martin Phys. Rev. B 85 (2012) 024113

16P. Singh, K. D. Sung, Y. A. Park, N.Hur, and J. H. Jung, J. Korean Phys. Soc. 55 (2009) 609

17 M. Kumar and K. L.Yadav, J. Appl. Phys. 1 (2006)100, 074111/

Conclusions

In this PhD thesis, an overview of the MOCVD fabrication has been provided for different perovskite materials: calcium copper titanate$CaCu_3Ti_4O_{12}$, bismuth ferrite $BiFeO_3$, lanthanum cobaltite ($LaCoO_3$), barium ceriate ($BaCeO_3$)and Ca-doped praseodymium manganites ($Pr_{1-x}Ca_xMnO_3$), which possess interesting physical properties of scientific and technological interest.

CCTO thin films have been deposited on $SrTiO_3$(100) single crystal substrates and on $La_{0.9}Sr_{1.1}NiO_4/LaAlO_3$(LSNO/LAO) stack. The MOCVD growth of CCTO films using a molten multimetal source has been achieved, representing an interesting and convenient alternative to the adoption of different sources for each component which would require the control of different parameters (gas flows and sublimation temperatures) for MOCVD process at 750°C.In addition, first attempts have been carried out using a two-step, in-situ MOCVD process, but CTO and CCTO phases have been obtained. These results indicate that selective formation of the CCTO phase is mainly related to the deposition temperature which needs to be lower than 900°C.

In regard to PCMO films grown through an MOCVD process using a molten multimetal source, the deposited films are of the $Pr_{0.7}Ca_{0.3}MnO_3$pure phase, with a different morphology depending on the used substrate. In all substrates the films are epitaxially grown as demonstrated by XRD and TEM measurements. In addition XPS investigations pointed to an homogeneous composition through the film thickness. The magnetic measurements allow to evidence the main characteristics of the thin films i.e. the presence of a FM transition temperature that has been correlated to the transport properties of the film.

$LaCoO_3$ thin films have been grown through a one step MOCVD process on single crystal substrates using the molten single source approach. The deposition temperature has been found to play a crucial role, thus below 650 °C, films are contaminated with lanthanum containing spurious phases, while temperatures higher than 650°C favor the formation of good crystalline quality $LaCoO_3$ films. The present study indicates that the best conditions for fabrication of crystalline, highly oriented and smooth $LaCoO_3$ films are temperatures around 800-900°C and water saturated oxygen flow. Finally, these results are interesting since they open the route to the fabrication of the La(Sr)CoO_3 films, that represent an interesting electrode for the SOFCs.

Good quality $BiFeO_3$films have been grown through an in-situ MOCVD process on $SrTiO_3$(001) and $SrTiO_3$:Nb (001) substrate. The use of multicomponent single source processes approach has shown good results not only for the deposition of$BiFeO_3$ but also for the Ba and Ti doped films. In fact, the present approach easily allowed the control of the stoichiometry of deposited films. The $BiFeO_3$ films show a well (00ℓ) oriented structure in all the investigated 700-800°C range. Pole figures confirmed the epitaxial nature of the $BiFeO_3$film and its in-plane alignment with respect to the substrate.PFM and PFS investigations suggest that within the present approach, films obtained at 800°C possess better ferroelectric properties. PFM investigation also showed the presence of different piezoelectric domains, that can be reoriented at the nanoscale by the application of a suited voltage to the AFM tip. The hysteresis loop of these domains showed a coercive voltage around 2V. Piezoelectric/ferroelectric properties are slightly worse in film deposited at lower temperature. Present data indicate that deposition temperature, also in this case, plays a crucial role since, even though the crystalline structure is independent on temperature, morphology and piezoresponse properties are strictly related to the deposition temperature.

In conclusion present data indicate that, this MOCVD approach has the advantage of being a very simple method for the easy production of functional perovskite materials and makes it possible to control simultaneously the evaporation rates of different precursors from molten, thus avoiding any problems related to the crystallite size and resulting in a constant evaporation rate even for very long deposition times. In all cases the MOCVD routes have shown great flexibility and proven to be a really intriguing challenge for implementation on large scale processes that could be superior or, at least, complementary to other methodologies.

Appendix: Experimental details

Precursor mass transport characterization. Thermogravimetric (TG) measurements of the mixture precursors were performed using a Mettler Toledo TGA/SDTA 851^{e}.The weight of the samples was between 10–15 mg (TG). Thermal investigations were carried out under vacuum (20 Torr) and at atmospheric pressure, under purified nitrogen, fed into the working chamber with a flow of 30 sccm. The differential scanning calorimetry measurements of the precursors have been carried out under purified nitrogen flow (30 sccm) at atmospheric pressure using a TC10 processor and DSC 30 calorimeter. Weights of the samples were between 4 and 10 mg (DSC). For all thermal measurements, the heating rates were 5 °C/min and temperature was measured with an accuracy of ± 0.1 °C.

MOCVD processes. The perovskite thin films were deposited in a low pressure, horizontal, hot wall reactor (diameter = 25 mm, length = 800 mm) equipped with a single sublimation zone. The precursors were placed in an Al_2O_3 boat, resistively heated at the appropriate vaporization temperature, inside the reactor in the sublimation zone. The vaporized source materials were transported through argon gas flow to the deposition zone. Oxygen flow was used as reaction gas. The carrier and reactive gas flow, controlled by mass flow meters, were introduced in close proximity to the reaction zone.

Film characterization.XRD measurements were recorded on a Bruker-AXS D5005θ-θ X-ray diffractometer, while θ–2θ patterns at various χ angles and polefigures were recorded on a Bruker D5005 θ–2θdiffractometer equipped with an Eulerian cradle. A Cu Kα radiation operating at 40 kV and 30 mA was used in all cases.

Film surface morphology was examined by field emission scanning electron microscopy (FE-SEM) using a ZEISSVP55 microscope. The atomic composition of the films was analyzed by energy dispersive X-ray analysis (EDX), using an INCA-Oxford windowless detector. X-ray photoelectron spectra (XPS) were measured with a PHI 5600 Multi Technique System (base pressure of the main chamber 3×10^{-10}Torr).The chemical mapping of the perovskite films has been performed by energy filtered transmission electron microscopy (EF-TEM) using the three windows method (JEOL 2010F, equipped with the Gatan imagining filter, instrument). Imaging and selected area electron diffraction were realized by JEOL FEG 2100 transmission electron microscope

The Scanning probe microscopies and spectroscopies were performed with a Solver P47NT-MTD instrument. For simultaneous topographic and piezoelectric properties evaluation, atomic force and piezoresponce force microscopies (AFM and PFM) were performed adopting Au-coated silicon tips.

List of international publications produced during the PhD research activity

1) **Catalano M. R**.; Toro R. G.; Gulino A.; Malandrino G.
Perovskite $LaCoO_3$ thin films on single crystal substrates: MOCVD growth and characterization.
Surf. Coat. Technol. **(2013)**, 230, 174-179.

2) Condorelli G. G.; **Catalano M. R**.; Smecca, E.; Lo Nigro R.; Malandrino G.
Piezoelectric domains in BiFeO3 films grown via MOCVD: Structure/property relationship
Surf. Coat. Technol. (**2013),** 230, 168-173.

3) **Catalano M. R**.; Malandrino G. Multifunctional Manganese Single Source Precursor for the Selective Deposition of MnF_2 or Mn_3O_4
Physics Procedia **(2013),** 46, 118-126.

4) Lipani Z.; **Catalano M. R.**; Rossi P.; Paoli P.; Malandrino G . A Novel Manganese(II) MOCVD Precursor: Synthesis, Characterization, and Mass Transport Properties of $Mn(hfa)_2$•tmeda
Chem. Vap. Deposition **(2013),** 19(1-2-3), 22-28.

5) Lo Nigro R.; Fiorenza P.; **Catalano M. R**.; Fisichella G.; Roccaforte F.; Malandrino G.
Binary and complex oxide thin films for microelectronic applications: An insight into their growth and advanced nanoscopic investigation
Surf. Coat. Technol. **(2013),** 230, 152-162.

6) **Catalano M. R.**; Malandrino G.; Toro R. G.; Lo Nigro R.
Control of Heteroepitaxial Growth of CaCu3Ti4O12 Films on SrTiO3 Substrates by MOCVD.
Chemical Vapor Deposition **(2012)** 18(1-2-3), 76-82.

7) **Catalano M. R.**; Malandrino G.; Bongiorno C.; Toro R. G.; Fiorenza P.; Bodeux R.; Wolfman J.; Gervais M.; Lambert C. A.; Gervais F.; et al.
$CaCu_3Ti_4O_{12}$ thin films on conductive oxide electrode. A comparative study between chemical and physical vapor deposition routes
Mater. Chem. Phys., (**2012**), 133, 1108-1115.

8) Malandrino G.; Toro Roberta G.; **Catalano M. R.**; Fragala M. E.; Rossi P.; Paoli P.
Pompon-Like MnF_2 Nanostructures from a Single-Source Precursor through Atmospheric Pressure Chemical Vapor Deposition
Eur. J. Inorg. Chem **(2012),** 1021-1024.

9) Scillato D.; Licciardello N.; **Catalano M. R.**; Condorelli G. G.; Lo Nigro, R.; Malandrino G.
$BiFeO_3$ films doped in the A or B sites. Effects on the structural and morphological properties. *J. Nanosci. Nanotechnol.*, **(2011),** 11, 8221-8225.

10) **M. R. Catalano**, E. Schilirò , G. Cucinotta, M. Mannini , A. Caneschi , R. Lo Nigro , E. Smecca , G. G. Condorelli , G. Malandrino
MOCVD synthesis of heteroepitaxial $Pr_{0.7}Ca_{0.3}$ MnO_3 films: effects of processing conditions on structural/morphological and functional properties.
Manuscript in preparation.

Acknowledgments

Arrivata alla fine di queste pagine, desidero ringraziare tutti coloro che in un modo o nell'altro hanno contribuito alla realizzazione di questo lavoro di dottorato.

Un grazie, profondamente sentito, va al mio tutor scientifico, la prof.ssa Graziella Malandrino, che è e sarà sempre un modello da seguire non solo nel mondo lavorativo ma soprattutto nei rapporti umani e personali. La ringrazio per aver messo a mia completa disposizione le sue competenze con professionalità e passione; è stata sempre in grado di mettermi nelle condizioni di lavorare nel miglior modo possibile, creando un clima sereno e di collaborazione.

Desidero ringraziare la Dott.ssa Raffaella Lo Nigro, non solo per il supporto sperimentale che ha dato a questa tesi, ma anche per avermi seguita nel primo periodo in laboratorio con tanta disponibilità e pazienza.

Ringrazio il prof. Guido Condorelli, per le misure XPS, AFM e PFM descritte in questo lavoro nonchè per la sua disponibilità.

Desidero ringraziare tutti i miei colleghi del gruppo, la Dott.ssa Cristina Tudisco, il Dr. Alessandro Motta, il Dr. Fabio Lupo, il Dr. Alessandro Di Mauro e il Dr. Emanuele Smecca, non solo per il supporto scientifico ma anche per le innumerevoli e allegre pause pranzo trascorse insieme.

Vorrei ringraziare tutta la mia fantastica famiglia per avermi incoraggiata e aiutata, sopratutto nell'organizzazione logistica delle giornate. In particolar modo vorrei ringraziare i miei due "masculazzi" che riescono a farmi sentire speciale e amata, dedicando loro questo mio importante traguardo raggiunto.

Infine l'ultimo pensiero va a chi avrebbe dovuto e voluto esserci e che ha sempre creduto in me.

Grazie.